

University of Warwick institutional repository: <http://go.warwick.ac.uk/wrap>

A Thesis Submitted for the Degree of PhD at the University of Warwick

<http://go.warwick.ac.uk/wrap/67107>

This thesis is made available online and is protected by original copyright.

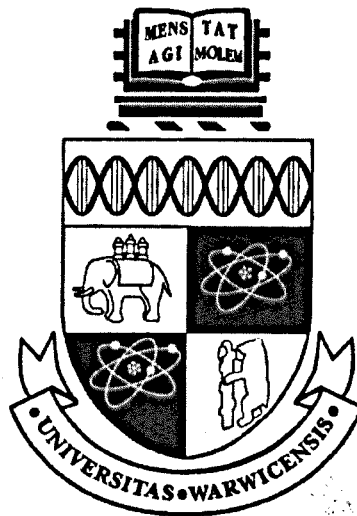
Please scroll down to view the document itself.

Please refer to the repository record for this item for information to help you to cite it. Our policy information is available from the repository home page.

Advances in EMAT measurements for NDE

Kwok Shun Ho

A Thesis presented for the degree of
Doctor of Philosophy



Ultrasonics Group
School of Engineering
University of Warwick
England
May 2007

Contents

Table of Contents	i
List of Figures and Tables	iv
Acknowledgements	xiii
Declarations	xiv
Abstract	xv
 Chapter 1	 1
Introduction	1
1.1 Introduction	1
1.2 Aims and Motivation	1
1.3 Thesis Outline	2
1.4 References	4
 Chapter 2	 7
A Review of EMAT Technology	7
2.1 Introduction	7
2.2 Historical Review	9
2.3 Typical EMAT designs	12
2.3.1 Bulk-Wave EMATs	12
2.3.2 Magnetostrictive EMAT for Pipes	13
2.3.3 Meander-Line Coil EMAT	14
2.3.4 Chirp-Coil EMAT	15
2.3.5 Periodic-Permanent-Magnet EMAT	17
2.3.6 Axial-Shear-Wave EMAT	17
2.3.7 EMATs for High-Temperature Measurements	20
2.4 Conclusions	20
2.5 References	21
 Chapter 3	 25
Application of Pulse-Compression Techniques to EMATs	25
3.1 Introduction	25
3.2 The Pulse-Compression Technique	26
3.3 Theory	27
3.4 Simulations	31
3.5 Experimental Arrangement	32
3.6 Results and Discussion	35
3.7 Conclusions	41
3.8 References	43

Chapter 4	46
Inspection of Drinks Cans using EMATs	46
4.1 Introduction	46
4.2 Tomographic Reconstruction Techniques.....	48
4.3 Experimental Setup	50
4.4 Results and Discussion.....	52
4.5 Conclusions.....	61
4.6 References	63
 Chapter 5	 65
Lamb Wave Tomography and Wavelet Processing	65
5.1 Introduction and Background.....	65
5.2 The Continuous Wavelet Transform	69
5.3 Simulations.....	71
5.4 Experimental Setup	74
5.5 Results Using the Mexican Hat Wavelet.....	76
5.6 Lamb Wave Tomographic Imaging	78
5.7 Discussion	84
5.8 The Use of the Morlet Wavelet	84
5.8.1 Background to the Morlet Wavelet	84
5.8.2 Analysis of EMAT data.....	87
5.9 Discussion and Conclusions.....	90
5.10 References	91
 Chapter 6	 95
Texture Measurement of Metal Sheets.....	95
6.1 Introduction	95
6.2 Overview of Texture Measurements	96
6.2.1 Theoretical Background	98
6.3 Transducer design	101
6.4 Stationary Wavelet Processing.....	102
6.4.1 Introduction	102
6.4.2 Theoretical Background	104
6.4.3 SWT Simulation.....	107
6.5 Preliminary Experiments.....	110
6.5.1 Apparatus and Experimental Setup	110
6.5.2 Results and Discussions	112
6.6 Mode identification	113
6.6.1 Short-Time-Fourier Transform approach.....	113
6.6.2 STFT Spectrogram	114
6.7 Demonstration of Multiple Mode Extraction	114
6.7.1 Stationary Wavelet Processing Approach.....	114
6.7.2 Wavelet Binary Tree Approach.....	116
6.8 Degree of Dispersion Considerations.....	119
6.8.1 Modes Analysis using FFT	119

6.8.2	Mode Velocities Analysis	121
6.9	Texture Measurements	122
6.9.1	Dispersion Effect Estimation in Thin Plates	122
6.9.2	Texture Experiments and Apparatus	123
6.9.3	Velocity Measurements On Thin Plate	123
6.9.4	Orientation Distribution Coefficients Extraction	124
6.9.5	Amplitude Measurements on Thin Plate	126
6.9.6	Texture Measurements on a Thick Plate using the s_0 mode.....	127
6.9.7	Texture Measurements on a Thick Plate using the a_0 Mode....	129
6.9.8	Texture Measurements on a Thick Plate using the a_1 Mode....	130
6.9.9	Amplitude Comparison of Multiple Modes on Thick Plate.....	132
6.10	Conclusions	133
6.11	References	134
Chapter 7		139
EMATs Fabricated using Micro-Stereolithography.....		139
7.1	Introduction	139
7.2	Micro-Stereolithography for EMAT Fabrication	140
7.3	Experimental Measurements of EMAT Performance.....	143
7.4	Imaging Using Synthetic Aperture Focussing Technique.....	149
7.5	Conclusions	152
7.6	References	154
Chapter 8		156
Conclusions		156
8.1	General Conclusions	156
8.2	Conclusions for each Chapter	156
8.3	Future Work	160
Bibliography.....		162
Publications arising from this thesis.....		162

List of Figures and Tables

Chapter 2

- Figure 2.1: An example of an optimised longitudinal and shear wave EMAT; (a) a shear wave EMAT, and (b) a longitudinal wave EMAT.
- Figure 2.2: Mechanisms of the bulk wave generation by the Lorentz force. (a) Typical planar coil, and (b) diagram of resultant force direction.
- Figure 2.3: A dual-mode EMAT with a spiral pancake coil and a magnet. (a) Coil configuration, and (b) Lorentz force mechanism.
- Figure 2.4: Magnetostriction EMAT for longitudinal waves along wires and pipes.
- Figure 2.5: A meander-line EMAT consisting of a permanent magnet and a meander-line coil. (a) Coil geometry and (b) Lorentz force mechanism.
- Figure 2.6: Focussing of the Shear-Vertical (SV) waves on a focal line in solid by the line-focusing EMAT.
- Figure 2.7: Appearance of the periodic-permanent-magnet EMAT (PPM-EMAT).
- Figure 2.8: Axial-shear wave EMAT consisting of a solenoid coil and a meander-line coil surrounding the cylindrical surface.
- Figure 2.9: Axial-shear-wave EMAT consisting of periodic permanent magnets with the alternating radial polarity and a solenoid coil surrounding the cylindrical surface.
- Figure 2.10: EMAT configuration for generating axial shear waves in a bolt head.
- Figure 2.11: Schematic cross-section of the torsional-mode EMAT consisting of permanent magnets with alternating radial polarity and a meander-line coil.

Chapter 3

- Figure 3.1: Characteristics of a typical chirp signal showing (a) the time domain waveform; (b) the corresponding frequency spectrum of (a); (c) the frequency vs. time delay characteristics of (a); (d) the equivalent matched filter characteristics, and (e) the compressed-pulse envelope.
- Figure 3.2: Numerical simulation of the pulse compression technique; (a) broadband reference chirp signal; (b) frequency spectrum of the reference signal; (c) simulated signal reflecting within a 50 mm thick plate with added noise, and (d) compressed signal after cross-correlation.
- Figure 3.3: Basic through-transmission arrangement for characterisation of an EMAT using conventional transient excitation.
- Figure 3.4: Characterisation of the pancake coil EMAT shown in Figure 2.3 in a 10 mm thick aluminium plate, using the apparatus of Figure 3.3. Shown are (a) a single shot waveform; (b) the result following 1000 averages, and (c) the spectrum resulting from the FFT of (b).
- Figure 3.5: Experimental arrangement for through-transmission measurements and imaging using two spiral pancake coil EMATs.
- Figure 3.6: Results illustrating the use of the pulse compression technique to the spiral coil EMAT. (a) Chirp signal generated by the NCA 1000 unit and used as a reference signal; (b) FFT of the signal in (a); (c) unprocessed signal detected after propagation through a 6mm thick aluminium sample, and (d) compressed pulse resulting from the cross-correlation of signals (a) and (c).
- Figure 3.7: Through-transmitted signal across a 2.25 mm aluminium plate using (a) the Panametrics pulser/receiver with no averaging, (b) The Panametrics pulser/receiver with 1000 averages.
- Figure 3.8: Through-transmitted signal across a 2.25 mm aluminium plate after using pulse compression without averaging.
- Figure 3.9: Example of the pulse compression output signal obtained across a 10 mm thick aluminium in through transmission mode.
- Figure 3.10: As Figure 3.8, but for a 31.8 mm thick brass plate.
- Figure 3.11: Thickness measurements of aluminium plates using EMATs and

pulse-compression system (circles). The results are compared to those measured using a vernier caliper gauge, shown as squares.

Figure 3.12: Through-transmission images of a 6 mm thick aluminium plate having a 6.5mm diameter circular hole, machined into one surface to a depth of 3 mm. (a) Panametrics pulser/receiver with 20 averages; (b) Panametrics pulser/receiver with 200 averages and (c) pulse compression signal processing technique using 20 averages.

Figure 3.13: Through-transmission internal defect images in aluminium plate. (a) Image obtained using Panametrics-NDT pulse/receiver with 20 averages; (b) image obtained using pulse compression unit with the same number of averages.

Table 3.1: Comparison of thickness measurements using a vernier caliper and EMAT pair of various brass plates.

Table 3.2: Same as Table 3.1 but with copper plates were used.

Chapter 4

Figure 4.1: The fan beam coordinate system and variables used in reconstruction.

Figure 4.2: The spiral-coil geometry used in the EMAT.

Figure 4.3: Schematic diagram of the experimental configuration used for collecting data using transient (pulsed) excitation.

Figure 4.4: The experimental configuration used to obtain data for tomographic reconstruction.

Figure 4.5: The experimental geometry used for data collection.

Figure 4.6: (a) A typical time signal that was generated and received across the beverage can filled with water, and (b) the corresponding frequency spectrum.

Figure 4.7: Experimental waveforms illustrating the arrival of multiple acoustic modes at various values of θ .

Figure 4.8: The velocity dispersion curves for Lamb waves propagating in an aluminium plate of thickness 0.15 mm, showing (a) phase velocity and (b) group velocity.

- Figure 4.9: Waveforms obtained using the pulse compression approach. The dotted line is the waveform obtained following conventional pulse compression, and contains s_0 Lamb modes, Shear Horizontal (SH) waves and longitudinal (L) acoustic modes, with multiple arrivals of each denoted by additional numbers. The result of mode extraction of the longitudinal mode is shown as the solid line, where interference with other modes has been dramatically reduced.
- Figure 4.10: The schematic diagram of the experimental setup to determine the location of a water-oil interface in the container.
- Figure 4.11: A single through-transmission signal obtained in water (solid line); oil (dotted line) and at a water-oil interface (dashed line).
- Figure 4.12: A grey-scale plot of the data obtained at various heights as the EMAT system was scanned vertically over the water/oil interface region.
- Figure 4.13: (a) The peak amplitude and the arrival time of the L mode as a function of vertical position; (b) Frequency spectra obtained in water (solid line), oil (dashed line), and at the interface (dotted line).
- Figure 4.14: The reconstructed attenuation image ($\text{dB}\cdot\text{mm}^{-1}$) of the water-filled cylindrical container with (a) a 6.6 mm diameter copper rod located at the coordinates (55, 35) mm, and (b) two 7.2 mm diameter aluminium rods located separately at the coordinates (15, 33) mm; (48, 48) mm. Amplitude scales are arbitrary.

Chapter 5

- Figure 5.1: (a) Phase velocity and (b) group velocity dispersion curves for the first five Lamb wave modes in a 1 mm thick aluminium plate.
- Figure 5.2: Mexican Hat or Gaussian wavelet function.
- Figure 5.3: (a) Simple simulated signal containing two discrete frequencies (f_1 and f_2) travelling at different speed, with added random noise. (b) The corresponding frequency spectrum. (c) Continuous Wavelet Transform (CWT) of (a).
- Figure 5.4: The effect of smoothing. (a) f_1 component extraction, and (b) CWT magnitude of the waveform shown earlier in Figure 5.3(a).
- Figure 5.5: Sampling geometry used for tomographic reconstruction.

- Figure 5.6: The experimental configuration for Lamb wave measurements.
- Figure 5.7: Experimental EMAT results for a 1 mm thick aluminium plate, showing (a) the received time waveform, (b) the corresponding frequency spectrum, and (c) CWT magnitude of the time waveform in (a).
- Figure 5.8: Measured s_1 mode group velocities on a 0.69 mm thick aluminium plate.
- Figure 5.9: Photographs of artificial defects in aluminium plates. (a) circular defect of ~ 11 mm diameter in 0.69 mm thick plate; (b) a non-circular defect of ~ 5.8 mm maximum width in a 1.25 mm thick aluminium plate; (c) a rectangular slot of dimensions $1.3 \text{ mm} \times 10.5 \text{ mm}$ machined through a 0.79 mm thick plate.
- Figure 5.10: Tomographic attenuation image, formed from amplitude data, of the defect shown earlier in Figure 5.9(a), using data for (a) s_0 (b) a_1 and (c) s_1 modes.
- Figure 5.11: Tomographic reconstruction using the a_1 mode and the sample of Figure 5.9(a), in terms of, (a) a_1 arrival time (to give slowness image), and (b) shift in peak frequency.
- Figure 5.12: Tomographic attenuation images using the a_1 mode amplitude for (a) the smaller non-circular defect shown in Figure 5.9(b), and (b) the slot shown in Figure 5.9(c).
- Figure 5.13: The complex-valued Morlet wavelet: (a) real part, (b) imaginary part.
- Figure 5.14: Frequency domain representation of the Morlet wavelet. An increase in wavelet scale, a , corresponds to a decrease in the centre frequency.
- Figure 5.15: Experimental EMAT results for a 0.69 mm thick aluminium plate; showing (a) the received time waveform (expanded version of the waveform shown earlier in Figure 5.7(a)); (b) the corresponding CWT magnitude of the time waveform in (a); (c) 3D visualisation of the data shown in (b).
- Figure 5.16: Experimental EMAT results for a 1 mm thick aluminium plate, showing (a) the received time waveform; (b) CWT magnitude using Morlet wavelet of the time waveform.

Chapter 6

- Figure 6.1: The estimated velocities (ms^{-1}) through 360° simulations.
- Figure 6.2: Schematic diagram of a meanderline EMAT showing (a) the coil geometry, and (b) the EMAT meanderline configuration.
- Figure 6.3: Lamb wave modes prediction in steel using the Rayleigh-Lamb dispersion curves, showing (a) phase velocity and (b) group velocity. The straight line in (a) corresponds to the wavelength (λ) defined by the meanderline spacing ($\lambda=1.8\text{mm}$).
- Figure 6.4: The SWT signal decomposition procedure, (a) A schematic diagram of a single level signal decomposition procedure using SWT, and (b) filter characteristics.
- Figure 6.5: Simulated input signals used for the SWT, (a) 1 MHz wave component, (b) 8 MHz wave component, (c) simulated waves (a) and (b) superimposed, and (d) frequency spectrum of (c).
- Figure 6.6: The FIR based approximation of the Meyer wavelet, (a) Mother wavelet function, (b) father scaling function, (c) frequency domain characteristic of the Wavelet filter correspondent to (a), and (d) Frequency domain characteristic of the scaling filter correspondent to (b).
- Figure 6.7: The SWT filters characteristics, (a) three levels up-sampling of wavelet function and (d) three levels up-sampling of scaling function.
- Figure 6.8: Signal decomposition and reconstruction using SWT. (a) Three levels decomposition of approximation coefficients, (b) three levels decomposition of detail coefficients, (c) three levels reconstruction of approximation coefficients, and (d) three levels reconstruction of detail coefficients.
- Figure 6.9: Schematic diagram of the experimental arrangement.
- Figure 6.10: Experimental result of the EMAT system, (a) time signal, and (b) frequency spectrum corresponds to (a).
- Figure 6.11: Mode identification using STFT, (a) Time signal used for the input of STFT, (b) the frequency spectrum corresponds to (b), (c) the resulted spectrogram using STFT corresponding to (a), and (d) 3D mesh plot of (c).

- Figure 6.12: Mode extraction using SWT, (a) the synthetic time signal of the approximation coefficients at level 3, (b) the corresponding frequency spectrum of (a).
- Figure 6.13: Schematic diagram of the binary tree SWT structure.
- Figure 6.14: Mode extraction using the binary tree SWT, (a) the synthetic time signal obtained at AADA4, (b) the corresponding frequency spectrum of (a), (c) the synthetic time signal obtained at DDDA4, (d) the corresponding frequency spectrum of (c), (e) the synthetic time signal obtained at DD2, (f) the corresponding frequency spectrum of (e).
- Figure 6.15: Experimental results obtained using various of different steel sheet thickness, (a) waterfall-plot of the time received signals, (b) the corresponding frequency spectrum of (a). Figure 6.16: Modes extraction using SWT at a range of different thickness. The solid-lines show the Rayleigh-Lamb dispersion curves of 1 mm thick steel, the dotted-points show the time extracted results obtained from Figure 6.14(a).
- Figure 6.16: Modes extraction using SWT at a range of different thickness. The solid-lines show the Rayleigh-Lamb dispersion curves of 1 mm thick steel, the dotted points show the time extracted results obtained from Figure 6.14(a).
- Figure 6.17: Phase and Group velocity dispersion curves simulated up to 1 MHz of 1 mm thick steel.
- Figure 6.18: The s_0 mode transit time (μs) texture result on the 0.05 mm thick steel sheet as a function of angle to rolling direction.
- Figure 6.19: The s_0 transit time (μs) together with a "theoretical fit" on the 0.05 mm thick steel sheet.
- Figure 6.20: s_0 directivity on 0.05mm thick steel, the scales are shown in arbitrary scales, (a) amplitude peak-to-peak, (b) FFT magnitude of the fundamental frequency, (c) FFT magnitude of the second harmonic, and (d) FFT magnitude of the third harmonic.
- Figure 6.21: s_0 mode texture result on the 0.39 mm thick steel sheet as a function of angle to rolling direction. The experimental transit time (μs) together with a theoretical fit.
- Figure 6.22: Normalised s_0 transit time on 0.05 mm (solid line) and s_0 transit time on 0.39 mm (dashed line).

- Figure 6.23: a_0 transit time (μs) mode texture result on the 0.39 mm thick steel sheet as a function of angle to rolling direction, with a “theoretical fit”.
- Figure 6.24: Normalised a_0 transit time on 0.39 mm (solid line) and s_0 transit time on 0.39 mm (dashed line).
- Figure 6.25: a_1 mode transit time (μs) texture result on the 0.39 mm thick steel sheet as a function of angle to rolling direction, with a “theoretical fit”.
- Figure 6.26: Normalised a_1 transit time on 0.39 mm (solid line) and s_0 transit time on 0.39 mm (dashed line).
- Figure 6.27: Directivity on 0.39 mm thick steel, the scales are shown in arbitrary scales, (a) s_0 peak-to-peak, (b) a_0 peak-to-peak, (c) a_1 peak-to-peak, and (d) s_2 peak-to-peak.
- Table 6.1: Calculated values of the ODCs obtained by using three velocity values at 0° , 45° , and 90° , and the theoretical fitting to Equation (6.2).

Chapter 7

- Figure 7.1: Schematic diagram of micro-stereolithography process used to fabricate EMAT coils.
- Figure 7.2: 3D-CAD models of the types of EMAT coil constructed using MSL, these being (a) spiral and (b) meander-line geometries.
- Figure 7.3: Process flow for production of a spiral EMAT. (a) MSL model is created, defining spiral EMAT architecture; (b) 200 nm planar layer of gold is sputtered over entire model; (c) model is polished to leave only depressions describing the spiral.
- Figure 7.4: Example of EMAT coil manufactured using MSL, (a) a spiral EMAT and (b) meanderline EMAT.
- Figure 7.5: Manufacture of an EMAT probe prototype.
- Figure 7.6: The experimental setup used for the characterisation of EMATs fabricated using MSL.

- Figure 7.7: Spiral-coil MSL EMATs in through-transmission. (a) Received time signal, and (b) corresponding frequency spectrum for the first arrival S1.
- Figure 7.8: Lift-off experimental result.
- Figure 7.9: The influence of magnetic field strength on the spiral-coil EMAT performance.
- Figure 7.10: (a) Schematic diagram of the experimental circuit to measure EMAT coil inductance. (b) Spiral-coil EMAT inductance as a function of the number of turns in the coil.
- Figure 7.11: Frequency and SV propagation angle of different meanderline conductor spacing, of 0.9 mm.
- Figure 7.12: Directivity patterns for a meander-line EMAT source with $l = 0.9$ mm. (a) $\theta = 30^\circ$ (b) $\theta = 40^\circ$ (c) $\theta = 50^\circ$ (d) $\theta = 60^\circ$ and (e) $\theta = 70^\circ$.
- Figure 7.13: Experimental setup used for SAFT imaging.
- Figure 7.14: A shear-vertical wave reflected from an artificial circular defect using MSL EMATs. The source was driven by a high power tone-burst with a centre frequency of 2.15 MHz. (a) The time received waveform, and (b) the corresponded frequency spectrum.
- Figure 7.15: SAFT image of a 10 mm through-hole defect (shown as the white circle) located at (125 mm, 32.5 mm, using EMAT receivers of (a) 105 mm and (b) 5 mm diameter.
- Figure 7.16: SAFT reconstructed image of a 5 mm through-hole defect, located at (125mm, 35mm).

Acknowledgements

I would like to sincerely thank my supervisors, Dr. Duncan Billson and Prof. David Hutchins, who have provided the invaluable guidance, technical knowledge and grammatical superiority throughout this project. This thesis would not have been possible without their support.

For all their generous advice, assistance and companionship, I also thank my colleagues in the Ultrasonic group at Warwick University. I particularly appreciate the efforts of Bob Bradley for advice in the manufacture of devices using micro-stereolithography. I should also like to thank a former colleague, Dr. Gan, for discussion in pulse-compression signal processing techniques and the software for the tomographic reconstruction. I also gratefully acknowledge the assistance of the academic and technical staff of the School of Engineering.

I must also acknowledge Crane Electronics Ltd for providing a 2 year part-time funding, and the Engineering and Physical Sciences Research Council (EPSRC) for providing a 3 year scholarship that enabled me to pursue this research work.

Finally, I want to thank my family for their enduring patience and encouragement.

Declaration

The work in this thesis is based on research carried out at the Ultrasonic Group, the School of Engineering, the Warwick University, England. No part of this thesis has been submitted elsewhere for any other degree or qualification and it all my own work unless referenced to the contrary in the text. All publications to date arising from this thesis are listed after the bibliography.

K. S. Ho, May 2007.

Abstract

This thesis describes a variety of experiments, many using advanced signal processing techniques, and electromagnetic acoustic transducers (EMATs). The first sections of this thesis describe the application of the pulse-compression signal processing technique with EMATs. This has been shown to improve the signal-to-noise ratio without the use of high levels of signal averaging, and thus potentially increases the speed of measurements. Ultrasonics thickness measurements and imaging were carried out to show that pulse-compression can be applied to the testing of the metals. The work was extended to demonstrate the successful measurement of fill level in drinks cans, and the detection of foreign bodies using fan-beam tomographic imaging in the drink cans.

This thesis also describes the application of a continuous wavelet transform (CWT) to EMATs. The technique was applied to experimental EMAT data in thin metal plates, to identify propagation of s_0 , a_0 , a_1 , s_1 and s_2 modes in an aluminium plate from one waveform. To illustrate the usefulness of the approach, the extracted multiple modes were applied to tomographic reconstructions of artificial defects in plates. This thesis also describes metal texture measurements using EMATs and wavelet processing. The work described in this section focuses on the multi-scale discrete wavelet method where the analysis in time and in wavelet scale is discrete as opposed to the CWT. The use of discrete wavelet processing for signal analysis can improve the performance of EMATs data in highly noisy environments.

Another section describes the use of the micro-stereolithography (MSL) process to fabricate EMATs, and this is followed by a description of the Synthetic Aperture Focussing Technique (SAFT) algorithm used to reconstruct images of data obtained from these EMATs. Finally, results are given, demonstrating that the EMATs can be used to perform NDE inspections. The thesis also contains conclusions and suggestions for further work.

Chapter 1

Introduction

1.1 Introduction

Ultrasonics is a powerful tool for the Non-Destructive Evaluation (NDE) of materials. NDE can be used to determine structural integrity, for flaw detection, and the measurement of stress and microstructure changes. It can also be used to study and characterise the elastic properties of materials. Ultrasonics can provide information on materials through a combination of velocity, attenuation, frequency change and other measurements [1–5].

In general, the accuracy and speed of many ultrasonic techniques can be hampered when using conventional piezoelectric transducers which need a coupling fluid. More rapid ultrasonic testing may be achieved using non-contacting methods [6–10], including air-coupled ultrasound [11–19]. In this thesis, advanced signal processing techniques are applied to Electromagnetic acoustic transducers (EMATs) and investigated for material testing and imaging. By combining signal processing techniques and EMATs, one can improve the overall performance of an EMAT system.

1.2 Aim and Motivation

EMATs have not been used widely in NDE applications, because they have several limitations that can limit their effectiveness, giving low signal-to-noise ratio (SNR). It is well known that low transduction efficiency is the major weakness in EMATs. In addition, the broad radiation patterns of the waves into the solids can reduce the ultrasonic energy to be concentrated on the target flaw. This is undesirable for ultrasonic imaging for flaw detection, because it is difficult to distinguish the flaw echo from the received signal. Furthermore,

EMATs can be sensitive to more than one ultrasonic mode and each of which can travel at different speeds, causing interference with the signal of interest. This characteristic makes received signals difficult to interpret directly.

The existing problems and limitations of EMATs are investigated in this thesis. Many problems can be resolved by using recent advances in signal processing techniques. In recent years, sophisticated algorithms have emerged to improve many ultrasonic measurements. Various methods have been developed in signal processing to enhance measurements for on-line applications. For example, the split-spectrum processing technique [20–22] has been developed to SNRs, based on the splitting of the received signal at a given location over a set of selected frequencies. Several other signal-processing filtering methods have been used to enhance the time-resolution and SNR of ultrasonic signal NDE signals. For example, Wiener filtering [23] and autoregressive spectral extrapolation [24] produce very good results. In addition, processing in software rather than by hardware has the advantage that limitations such as dynamic range and system linearity can substantially improved [25].

1.3 Thesis Outline

This thesis describes work conducted on the application of various signal processing techniques to EMATs. As EMATs will be used extensively throughout this thesis, they are described in detail in chapter 2.

Chapter 3 describes a pair of non-contact EMATs that can be used for thickness measurements and imaging of metallic plates. Experiments were performed using wide bandwidth EMATs and pulse-compression processing techniques, using chirp excitation. This gave a greatly improved SNR for air-coupled experiments, increasing the speed of data acquisition. A numerical simulation of the technique confirmed the performance. Experimental results indicate that it is possible to perform non-contact ultrasonic imaging and thickness gauging in a wide range of metal plates. The resolution of the image obtained using the pulse compression approach was also improved compared to a transient pulse signal from a conventional pulser/receiver. It is thus suggested

that the combination of EMATs and pulse compression can lead to a wide range of online applications where rapid testing is necessary.

Chapter 4 uses EMATs to transmit ultrasonic signals across liquid-filled aluminium beverage containers. The work has demonstrated a non-contact method for both determining the location of liquid boundaries, and detecting the presence of foreign bodies using fan-beam tomographic imaging. Pulse compression signal processing, followed by acoustic mode extraction, has been used in a new technique, whereby unwanted guided waves that travel around the container wall can be identified and removed from the image reconstruction process. Such waves would normally complicate the identification of the signals require for image formation that propagated through the liquid. The result is a method that has been used to provide images, by scanning EMATs around the outer surface of aluminium drinks cans.

Chapter 5 describes Lamb wave tomography using multiple mode propagation in plates. This has been carried out using a high voltage transient EMAT system. As EMATs are non-contact, inexpensive and portable, they are an excellent choice for fast and automated data collection for Lamb wave tomography. A technique has been developed to improve the analysis of multi-mode Lamb wave propagation, using a continuous wavelet transform (CWT). This was applied to experimental EMAT data in thin metal plates, to identify propagation of s_0 , a_0 , a_1 , s_1 and s_2 modes from one waveform. Fourier and Wavelet Transforms have been used for mode identification on various thicknesses of plate, and the results applied to tomographic reconstruction of artificial defects in plates to illustrate the usefulness of the approach.

Chapter 6 continues the ultrasonic Lamb wave mode investigation, for the NDE of the texture and formability of metal sheets. This uses both symmetric (s_0 and s_2) and asymmetric modes (a_0 , and a_1) modes. This work was performed using a pair of magnetostrictive EMATs. Digital signal processing and integrated scan control were used. Modes were identified using the Short-Time Fourier Transform (STFT), and the precise cut-off frequency and bandwidth associated with each mode is extracted using the Stationary Wavelet Transform (SWT). This technique is fast and efficient, and has been carried out for the first time in EMATs for Lamb waves extraction. The filtering was obtained by correlating the wavelet via Quarature Mirror Filtering (QMF) pairs.

This technique has been implemented in a complete binary tree system to achieve mode extraction, which was then used to obtain texture information on plates.

Chapter 7 demonstrates the use of a micro-stereolithography (MSL) rapid prototyping technique to produce EMATs. The work has characterised the EMATs produced using this technique, in both meander-line and spiral-coil configurations. A synthetic aperture focussing technique (SAFT) has been applied to the ultrasonic signals from these devices to reconstruct images in metallic objects.

Finally, Chapter 8 presents conclusions and suggestions for further work.

1.4 References

- [1] J. L. Rose, *Ultrasonic Waves in Solid Media*. Cambridge : Cambridge University Press, 1999.
- [2] J. Blitz and G. Simpson, *Ultrasonic Methods of Non-Destructive Testing*. New York : Chapman & Hall, 1996.
- [3] T. Kundu, *Ultrasonic Nondestructive Evaluation : Engineering and Biological Material Characterization*. Boca Raton, FL : CRC Press, 2003.
- [4] J. D. N. Cheeke, *Fundamentals and Applications of Ultrasonic Waves [Electronic Resource]*. Boca Raton : CRC Press, 2002.
- [5] J. Krautkrämer, H. J. Krautkrämer and W. Grabendorfer, *Ultrasonic Testing of Materials*. New York : Springer-Verlag, 1990.
- [6] C. B. Scruby and L. E. Drain, *Laser Ultrasonics : Techniques and Applications*. Adam Hilger, 1990.
- [7] M. Hirao and H. Ogi, *EMATs for Science and Industry : Noncontacting Ultrasonic Measurements*. London : Kluwer Academic Publishers, 2003.
- [8] E. P. Papadakis, *Ultrasonic Instruments and Devices : Reference for Modern Instrumentation, Techniques, and Technology*. London : Academic, 2000.
- [9] W. R. Hedrick, D. L. Hykes and D. E. Starchman, *Ultrasound Physics and Instrumentation*. London : Mosby, 1995.

- [10] Š Kočiš and Z. Figura, *Ultrasonic Measurements and Technologies*. London : Chapman & Hall, 1996.
- [11] T. R. Gururaja, W. A. Schulze Jr., L. E. Cross, R. E. Newnham, B. A. Auld and Y. J. Wang, "Piezoelectric composite materials for ultrasonic transducer applications. I. Resonant modes of vibration of PZT rod-polymer composites," *IEEE Trans. Sonics Ultrason.*, vol. SU-32, pp. 481-98, 07. 1985.
- [12] J. D. Fox, B. T. Khuri-Yakub and G. S. Kino, "High-frequency acoustic wave measurements in air," in *1983 Ultrasonics Symposium Proceedings*. 1983, pp. 581-584.
- [13] J. D. Fox, B. T. Khuri-Yakub and G. S. Kino, "Acoustic resonator transducer for operation in air," *Electron. Lett.*, vol. 21, pp. 694-6, 08/01. 1985.
- [14] O. Krauss, R. Gerlach and J. Fricke, "Experimental and theoretical investigations of SiO₂-aerogel matched piezo-transducers," *Ultrasonics*, vol. 32, pp. 217-22, 05. 1994.
- [15] M. Tone, T. Yano and A. Fukumoto, "High-frequency acoustic wave measurements in air," *Jpn J Appl Phys Part 2 Letter*, vol. 23, pp. 436-438, 1984.
- [16] H. Kawai, "The piezoelectricity of poly(vinylidene fluoride)," *Jpn. J. Appl. Phys.*, vol. 8, pp. 975-6, 07. 1969.
- [17] M. Platte, "PVDF ultrasonic transducers for nondestructive testing," in *Goteborg Conference on Piezo- and Pyroelectric PVDF Films*, 1991, pp. 229-46.
- [18] W. Manthey, N. Kroemer and V. Magori, "Ultrasonic transducers and transducer arrays for applications in air," *Meas Sci Technol*, vol. 3, pp. 249-61, 03. 1992.
- [19] H. Ohigashi, K. Koga, M. Suzuki, T. Nakanishi, K. Kimura and N. Hashimoto, "Piezoelectric and ferroelectric properties of P (VDF-TrFE) copolymers and their application to ultrasonic transducers," in *Proceedings of the First International Symposium on Piezoelectricity in Biomaterials and Biomedical Devices*, 1984, pp. 263-76.
- [20] N. M. Bilgutay and J. Saniie, "Effect of grain size on flaw visibility enhancement using split-spectrum processing," *Mater. Eval.*, pp. 808-814, 1984.
- [21] L. Ericsson and T. Stepinski, "Verification of split spectrum technique for ultrasonic inspection of welded structures in nuclear reactors," *Eur J Non Destr Test*, vol. 2, pp. 56-64, 1992.

- [22] M. Karaoguz, N. Bilgutay, T. Akgul and S. Popovics, "Ultrasonic testing of concrete using split spectrum processing," *Mater. Eval.*, vol. 57, pp. 1183-1190, 1999.
- [23] G. Hayward and J. E. Lewis, "Comparison of some non-adaptive deconvolution techniques for resolution enhancement of ultrasonic data," *Ultrasonics*, vol. 27, pp. 155-64, 05. 1989.
- [24] S. Sin and C. Chen, "A comparison of deconvolution techniques for the ultrasonic nondestructive evaluation of materials," *IEEE Trans. Image Process.*, vol. 1, pp. 3-10, 1992.
- [25] D. R. Daughton and N. Mulders, "High-resolution ultrasonic spectrometer using digital signal processing," *J. Low Temp. Phys.*, vol. 134, pp. 413-418, 2004.

Chapter 2

A Review of EMAT Technology

This chapter presents a literature review of EMAT technology. EMATs basically consist of a coil, and magnetic field; operate on a conductive substrate. Although the operation of an EMAT sounds rather simple, there are many important details that enter into designing and building a useful EMAT before they can be used for non-destructive testing. The optimum design of an EMAT requires an understanding of the coupling mechanism of energy transfer between the transducer and sample.

2.1 Introduction

EMATs can be used for both ultrasonic generation and detection [1–7], and they have been used for the non-contact generation and detection of ultrasonic signals in metals for some time [3, 5]. The exact wave mode to which the EMAT is sensitive depends on the coil and magnetic field configuration. A wide variety of EMAT coils have been utilised to produce maximum sensitivity to certain wave modes. The most important design feature of an EMAT is the choice of the correct coil configuration and magnetic field distribution. For example, by changing the orientation of the magnetic field with respect to the coil, longitudinal and shear wave modes can be optimised. Both longitudinal and shear wave EMATs may be constructed, as shown schematically in Figures 2.1 (a) and (b).

The transmitter coil is conventionally driven with a transient current pulse. The characteristics of an EMAT as an ultrasonic source depend on the direction of the applied magnetic field, B , and eddy current density, J , induced at a conducting surface. The presence of a Lorentz force, F , on the substrate causes an elastic wave to propagate into the volume of the material, or along the

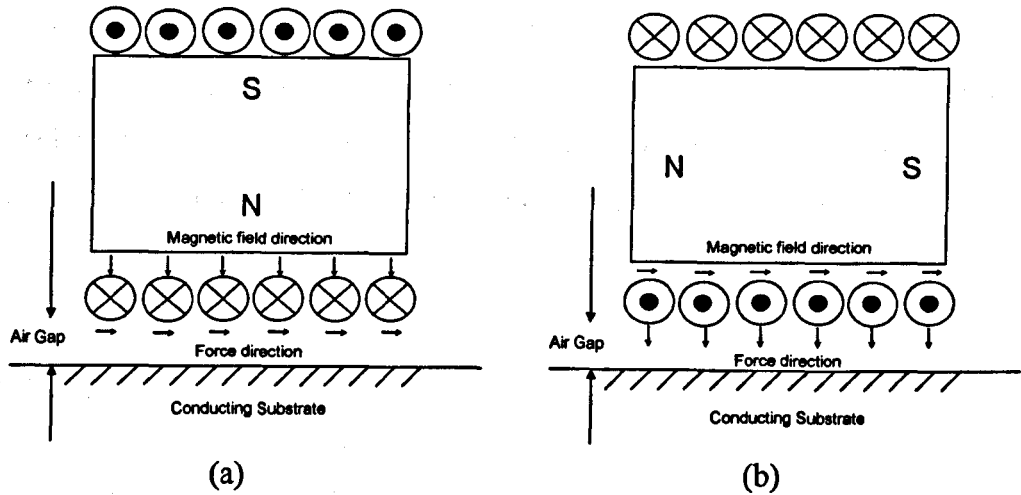


Figure 2.1: An example of an optimised longitudinal and shear wave EMAT; (a) a shear wave EMAT, and (b) a longitudinal wave EMAT.

surface. Let \vec{B} and \vec{J} represent the static magnetic field and the eddy currents (both are vector quantities). Subjecting the currents flowing in a material to a superimposed magnetic field creates the Lorentz force, the magnitude and direction of which is given by:

$$\vec{F} = \vec{J} \times \vec{B} \quad (2.1)$$

where \vec{B} is static, and \vec{J} alternates with the frequency of the driving current in the conductor coil. Therefore, \vec{F} also alternates in a direction perpendicular to and at a frequency identical to the driving current, according to the right hand rule. EMAT detection works via an inverse process, where motion of the surface induces an e.m.f. into the coil.

The theory is a well-researched area and many studies appear in the literature [1–10]. The Lorentz force arises in all conducting materials, while a magnetostriction mechanism appears only in ferromagnetic materials [11]. Note that magnetostriction does not occur in a non-magnetic material (e.g. aluminium). For example, Thompson [2] studied the field dependence of the guided wave amplitude in ferromagnetic thin plates and derived a theoretical model to explain the results. Il'in and Kharitonov [6] calculated the efficiency of detecting Rayleigh waves radiated by a meander-line coil in a ferromagnetic metal, and Wilbrand [7, 8] discussed bulk-wave detection involving the three mechanisms. Following them, Ogi [9, 10] improved Wilbrand's model to

explain the field dependence of the bulk wave excitation and detection in a ferromagnetic metal. Note that both Lorentz and magnetostrictive forces operate simultaneously in a ferromagnetic material, and can in fact cancel each other in some circumstances. Hence, it is important to consider both forces when describing an EMAT for a ferromagnetic material.

2.2 Historical Review

The acoustic coupling with EMATs is a basic physical effect, which occurs whenever a magnetic field, dynamic current, and a metal object are located in close proximity. For instance, Wegel and Walther [12] studied the low-frequency internal friction in brass by applying variable-frequency current to a coil, which drove a magnetic unit bonded to one end of a cylindrical specimen, and an identical magnetic unit on the other end detected the vibration. Their experimental arrangement allowed the generation and detection of longitudinal and torsional modes through the specimen.

Following them, Randall *et al.* [13] devised a measurement setup without using pole pieces to study the grain size dependence of internal friction in brass. Their arrangement was based on the Lorentz force coupling to detect the longitudinal resonance, and hence to measure the Q value. Houck *et al.* [14] presented evidence that RF-ultrasonic coupling can occur near the surface of a metal in the presence of a magnetic field. The signal amplitude was shown to be proportional to the magnetic strength. Gaerttner *et al.* [11] conducted an experiment on aluminium and tungsten crystals to observe the dependence of received shear wave amplitude on frequency (10 to 70 MHz) and temperature (4.2 to 300 K). Temperature varies the metal's conductivity and thus skin depth, which changes the generation efficiency with the Lorentz force mechanism. Good agreement with the theory was presented.

Using a similar configuration, Dobbs [15] showed that shear and longitudinal waves can be generated separately by orienting the static field to be normal and parallel to the specimen surface, respectively, and concluded that the action of the Lorentz force on the electronic current in the skin depth was responsible for the generation. He emphasised the usefulness for the NDE of

metals and also measured the exponential decay of shear wave amplitude with the air gap up to 1.0 mm from the aluminium surface. Filimonov *et al.* [16] and Nikiforenko *et al.* [17] developed instrumentation in the 1-20 MHz frequency range. They observed resonance peaks attributable to the longitudinal and shear modes of thickness oscillations of metal plates and splitting shear-mode peaks, which are now interpreted as a birefringence effect caused by the texture-induced elastic anisotropy in the rolled metal sheet. They claimed the usefulness of this contactless method for measuring the elastic-wave speeds and the anisotropic elastic constants.

In the 1970's, EMATs were studied with the aim of developing non-contact flaw-detection methods. Butenko *et al.* [18] pointed out some remarkable advancements with the EMAT technique. The Lorentz force was considered to be the coupling mechanism, but some experiments indicated that magnetostriction also occurred. EMATs have been used for a wide range of applications. For example, the anisotropic velocity measurement using polarised shear waves, the thickness measurements for hot-rolled pipes with shear wave pulse-echo technique, a mobile system for inspection of railway track, and an automatic flaw detector on seamless pipes. The advantages and disadvantages on EMATs were just as thirty years later, namely:

- (i) non-contact operation and good tolerance to the surface conditions;
- (ii) generation and reception of wide variety of ultrasonic waves;
- (iii) applications to high temperature measurements up to 1000 °C;
- (iv) detection of anisotropic elastic constants with polarised shear waves;
- (v) low transfer efficiency compared to the piezoelectric transducers;
- (vi) inapplicability to non-conducting materials.

EMATs were not recognised as a generally useful technique and did not replace the piezoelectric transducers in most flaw detection applications. This is because the received signals were too small to make reliable flaw detection on metal components. As such, the EMATs didn't gain much attention during the 1980's except for the limited applications including measurements on metals at elevated temperature and moving at moderate speeds. It was also said that the

EMAT techniques were mature [19], in comparison with other non-contact techniques such as laser-ultrasound and air-coupled transducers. Practical designs of EMATs and discussions on them can be found in Maxfield and Fortunko [20], and Alers and Burns [21]. The bulk-wave EMAT and many other EMAT configurations emerged from these studies, which are still of much value. The EMAT designs and instrumentation were facilitated by the physical models, which were best described by Thompson [3] and recently extended by Ogi [22]. Thompson provided a general framework and analytical formalism covering both of the Lorentz-force and magnetostrictive coupling mechanisms.

Although low transduction efficiency is a weakness of EMATs, once this is overcome or compensated for their unique and attractive features open up novel ultrasonic methodologies. Many of the early EMATs were employed in resonance to maximise the signal intensity. The spectrometric approach [23] (a technique for studying a variety of physical phenomena through resonance frequency and resonance-peak sharpness (Q^{-1} value)) gives rise to the ultrasonic resonances, hence improving the SNR to a large extent. Kawashima [24] applied this technique to detect the rolling texture and estimate the formability (r-value) in thin steel sheets. The available frequency range was up to 50 MHz and was later increased to 120 MHz for a 20 μm thick aluminium foil [25].

Johnson *et al.* [26, 27], and Clark *et al.* [28] have proposed the use of Electromagnetic Acoustic Resonance (EMAR) for materials characterisation. With the recent advances of the electronics and signal processing, EMAR has shown great potential for velocity and attenuation measurements. The difficulty of a precise velocity measurement is overcome by incorporating highly sensitive EMATs and employing a superheterodyne signal processing [29, 30]. Furthermore, it was found that EMAR can give an absolute value of attenuation owing to the non-contacting nature and low transfer efficiency [31]. This is one of the attractive aspects of EMAR, because the absolute measurement of attenuation has never been realised with contact techniques.

2.3 Typical EMAT designs

2.3.1 Bulk-Wave EMATs

Figure 2.2 shows the configuration of a bulk wave EMAT, which is sensitive to both longitudinal waves, and shear waves with a polarisation parallel to the specimen surface. The compact structure, broad bandwidth, and high transfer efficiency promote its frequent use in many scientific and practical applications. The permanent magnets produce a magnetic biasing field normal to the surface under the unidirectional coil elements and the tangential fields at the centre and edges of the coil elements. The resultant force (F) is parallel to the surface. In such cases, this EMAT will be referred to as shear wave EMAT.

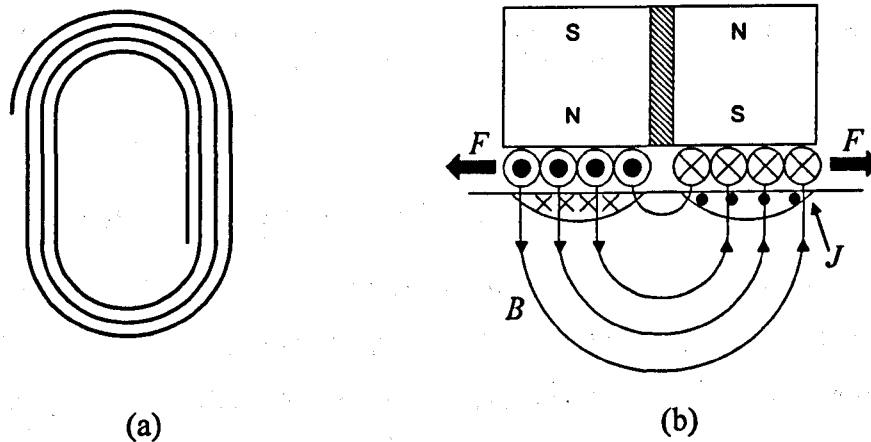


Figure 2.2: Mechanisms of the bulk wave generation by the Lorentz force. (a) Typical planar coil, and (b) diagram of resultant force direction.

Figure 2.3 shows a schematic diagram of the generation mechanism with Lorentz forces of another bulk-wave EMAT. It consists of a single cylindrical permanent magnet and a flat pancake coil. The static field from the magnet has the radial and the normal components, which interact with the eddy currents and induce the Lorentz forces along the normal and radial directions, respectively. For a ferromagnetic material, magnetostriction forces will be present. These forces generate the longitudinal wave and the radially-polarised shear wave both propagating in the thickness direction at the same time, for which this is called dual-mode EMAT. If the metal has elastic anisotropy, the shear waves decompose into two polarisations along the two principal directions producing

the split resonance peaks. This EMAT has been used for the measurement of in-plane anisotropy in rolled steel sheets [32] and the birefringent acoustoelastic stress measurement [33].

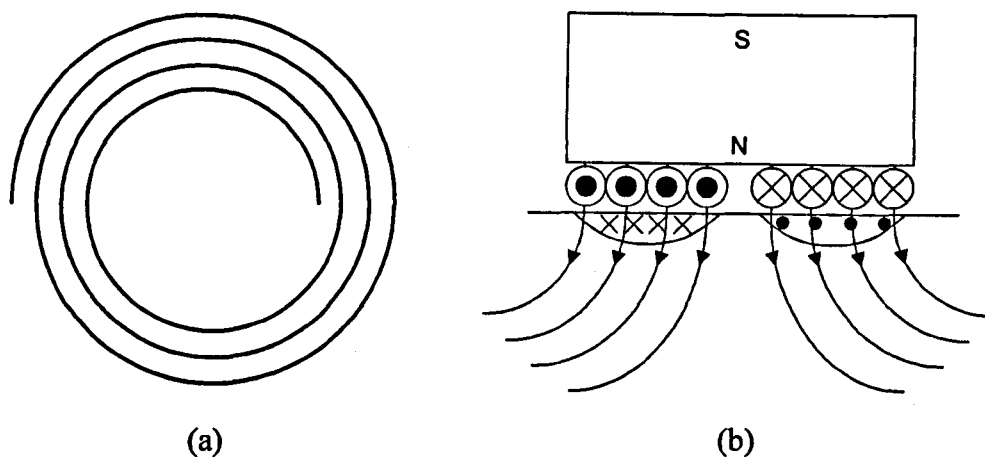


Figure 2.3: A dual-mode EMAT with a spiral pancake coil and a magnet. (a) Coil configuration, and (b) Lorentz force mechanism.

2.3.2 Magnetostrictive EMAT for Pipes

Figure 2.4 shows an EMAT designed to generate and detect longitudinal guided waves along a rod or pipe specimen [34–39]. It consists of an electromagnet or permanent magnet to provide the biasing field along the specimen's axis and a solenoid coil to generate a dynamic field superimposed on the biasing field. The magnetostriction mechanism is dominant, and the generation efficiency is thus determined by the slope of the magnetostriction curve, as demonstrated by Yamassaki, *et al.* [39]. The longitudinal wave generated by this EMAT travels along 100 m or more. The generated signal is mainly the non-dispersive fundamental longitudinal mode with nominal velocity, and given by:

$$v_f = \sqrt{E/\rho} \quad (2.2)$$

where E is the Young's modulus and ρ is the density. Long-range inspection is then possible to detect large precipitation particles and flaws in wires in a production environment. This EMAT, however, generates the waves

symmetrically in both directions, which can make the signal interpretation difficult.

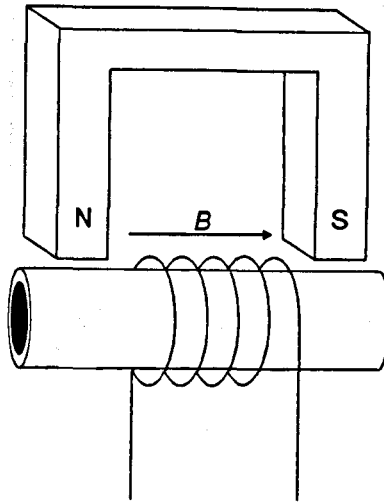


Figure 2.4: Magnetostriction EMAT for longitudinal waves along wires and pipes.

2.3.3 Meander-Line Coil EMAT

Figure 2.5 shows the configuration of a meander-line coil EMAT, which can be used for Rayleigh and Lamb waves, and angled shear and longitudinal waves (travelling obliquely into the specimen). Thus, a disadvantage of this EMAT is difficulty of the mode identification in the observed echoes.

A normal biasing field and a meander-line coil as illustrated in Figure 2.5, induces the Lorentz and magnetostriction forces parallel to the surface, whose directions change alternately with the meandering period. The generation frequency is governed by the meander-line period, which can be controlled by fabricating the coil by a printed circuit technique. The technique is therefore capable of generating ultrasonic waves of higher frequencies. The generation of Rayleigh wave is possible on thick samples and Lamb waves on thinner samples. The maximum transfer efficiency of Lamb waves occurs when the wavelength is tuned to the thickness of the specimen [1]. Tangential biasing magnetic field to surface and a meander-line coil work for the surface SH waves [10]. A disadvantage is the necessity of very large biasing magnetic field when the static magnetic field is applied along the straight lines of the meander-line coil.

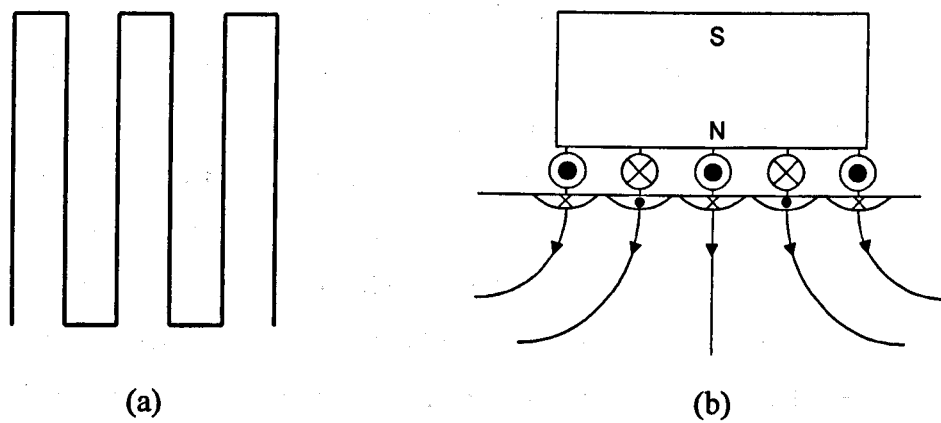


Figure 2.5: A meander-line EMAT consisting of a permanent magnet and a meander-line coil. (a) Coil geometry and (b) Lorentz force mechanism.

2.3.4 Chirp-Coil EMAT

A potential application of the meander-line coil EMAT is flaw detection in ferromagnetic metal sheets. Like other EMATs, it can operate on moving sheets for on-line inspection; however, a classic trade-off is encountered between the SNR and the measurement resolution. Being excited by a current impulse, the EMAT launches a wave train of constant amplitude, and the carrier wavelength equals the meander-line period. When the same EMAT is used as a receiver, the maximum amplitude is then proportional to the number of turns in the meander-line coil. A long coil of many turns produces a high amplitude, but results in an elongated received signal, reducing both the spatial and temporal resolution.

The problem can be solved by generating ultrasonic waves with a meander-line coil, whose period changes linearly along the propagation direction, and by detecting the reflected waves with another meander-line coil having the reversed period variation of the generating coil. This configuration results in a compressed pulse with high amplitude. When an impulse is fed to the coil, the generator coil emits a wave package, in which the wavelength varies continuously with time, that is, a chirp signal. A narrow spacing generates higher frequencies, and a wide spacing generates lower frequencies. Unless the wave is dispersive, all the frequency components arrive at the matching coil elements with a common delay time. In other words, the coincidence between the wavelength and the coil period occurs only at one

specific time over the whole length of the receiving coil. At this moment, a current is induced in the coil, inducing a sharp pulse. However, care should be taken to avoid the influence of the higher order modes. The chirp signal contains frequency components of a certain bandwidth. If higher order modes occur, they can disguise the desired signal output.

Moreover, focusing of the angled shear and longitudinal waves on a focal line in a solid can be obtained by using a specially designed meander-line coil. The array of the meander-line elements is not uniform, and can focus the oblique shear waves propagates normal to the specimen on a line inside the material. This EMAT is called a line-focusing EMAT [40, 41]. The design of a line-focusing EMAT coil makes use of the radiated wave from a single line source on the surface. Thus the design spacing of each meander-line element can concentrate the radiated beams having incident angles centred on this angle to a focal line. Figure 2.6 shows a configuration of the line-focusing EMAT, which consists of a permanent magnet block to supply the bias field normal to the surface, and a meander-line coil to induce eddy currents and the dynamic fields in the surface region.

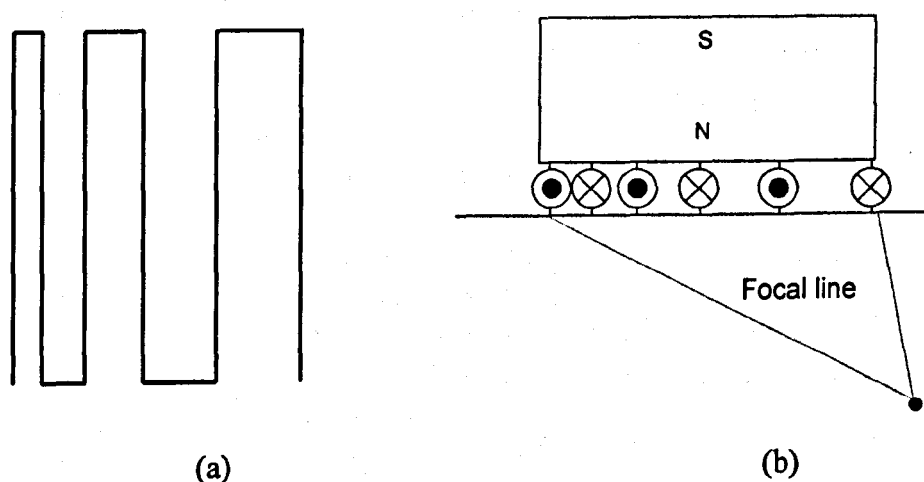


Figure 2.6: Focussing of the Shear-Vertical (SV) waves on a focal line in solid by the line-focusing EMAT.

Shearing forces arise parallel to the surface under the coil segments, which are caused by the Lorentz force mechanism in a nonmagnetic metal and by the magnetostriction force mechanism in a ferromagnetic metal. Ogi, *et al.*

[40] have demonstrated the determination of such meander-line spacing by using Newton's numerical method.

2.3.5 Periodic-Permanent-Magnet EMAT

Figure 2.7 illustrates a PPM-EMAT for generating shear waves polarised parallel to the specimen surface in both sides. The shear waves are launched not only along the surface but also into the material [3]. The EMAT has been often used for measurements with the surface or plate SH waves.

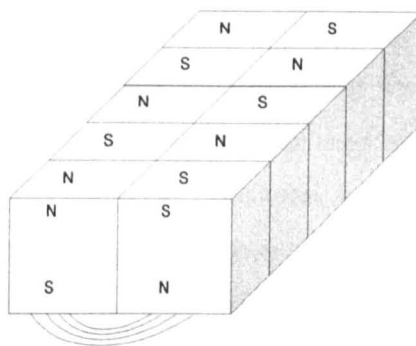


Figure 2.7: Appearance of the periodic-permanent-magnet EMAT (PPM-EMAT).

The polarity of the permanent magnets is alternately varied to cause tangential Lorentz and magnetostriction forces whose directions alternately change with the same period of the magnet array. Thinner magnets are required to generate high-frequency SH waves, which are preferable for the NDE of surface flaws. The maximum transfer efficiency occurs when the wavelength is tuned to the spacing of magnets. However, the efficiency drastically decreases with the magnet thinness. If magnets are ~ 1 mm thick, then the maximum shear wave frequency for common steel is ~ 1.6 MHz. Thus, a limitation of this EMAT is its operation frequency, usually only up to approximately this frequency.

2.3.6 Axial-Shear-Wave EMAT

An axially-polarised shear wave, called an axial shear wave, travels in the circumferential direction along a cylindrical surface of a circular rod or pipe specimen. Figure 2.8 shows the magnetostrictively coupled EMAT designed for

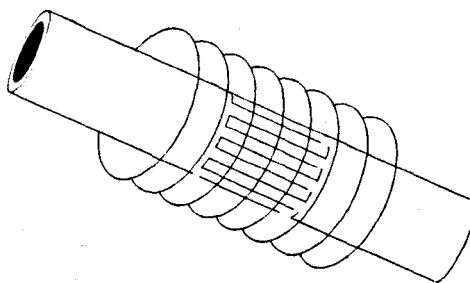


Figure 2.8: Axial-shear wave EMAT consisting of a solenoid coil and a meander-line coil surrounding the cylindrical surface.

the axial shear wave in ferromagnetic materials [42]. It consists of a solenoid coil to supply the biasing magnetic field along the axial direction, and a meander-line coil surrounding the cylindrical surface to induce the dynamic field in the circumferential direction. The total field oscillates about the axial direction at the same frequency as the driving currents and produces a shearing vibration through the magnetostriction effect, resulting in the axial shear wave excitation. The same coil works as a receiver through the reverse mechanism.

For a nonmagnetic material, the axial shear wave can be generated by the Lorentz force mechanism using permanent magnets arranged with radial polarity of alternating sign from one magnet to the next and a solenoid coil surrounding the cylindrical surface as shown as Figure 2.9.

The EMAT geometry of Figure 2.9 can be modified [43] for generation and reception of the axial shear resonance in the head of a bolt (Figure 2.10). It consists of thin permanent magnets arrayed to serve the alternating bias fields normal to the side faces, and the solenoid coil wound in a hexagonal shape. When the driving current is applied to the coil, the shearing forces in the axial direction arise periodically and generate the shear waves propagating in the circumferential direction with the polarisation along the both axis.

The axial shear wave design has been further modified for the development of trapping of vibration energy and non-contacting measurement. For example, Johnson *et al.* [44] presented an EMAT to trap torsional-vibration energy in a stepped rod. They also presented an approximate theory to explain the measurements. Figure 2.11 shows the configuration of a trapped-torsional-mode EMAT. The EMAT consists of magnets arranged with radial polarity and

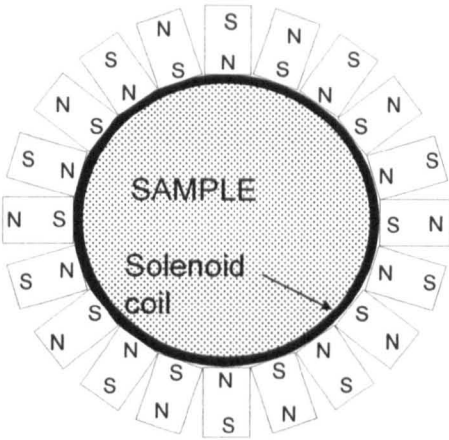


Figure 2.9: Axial-shear-wave EMAT consisting of periodic permanent magnets with the alternating radial polarity and a solenoid coil surrounding the cylindrical surface.

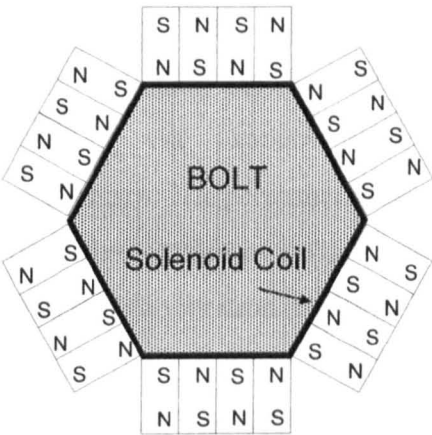


Figure 2.10: EMAT configuration for generating axial shear waves in a bolt head.

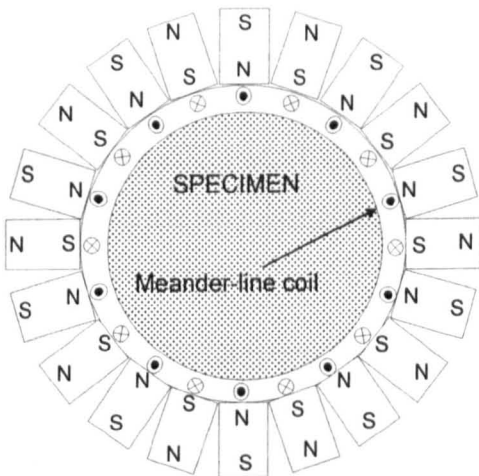


Figure 2.11: Schematic cross-section of the torsional-mode EMAT consisting of permanent magnets with alternating radial polarity and a meander-line coil.

alternating sign from one magnet to the next, and a meander-line coil surrounding the cylinder. Alternating currents in the coil result in Lorentz forces in the circumferential direction at the cylinder surface, thus coupling to torsional vibrations of the cylinder.

2.3.7 EMATs for High-Temperature Measurements

An EMAT for measuring elastic constants and internal friction of small specimens at high temperatures has been described by Ogi, et al [45]. A specimen was inserted in a solenoid coil located within a stainless steel cylindrical chamber. The solenoid coil was made with a Ni-alloy wire and its shape is held by a ceramic cement so as to operate at higher temperatures above 1000°C. A pair of permanent magnets located outside the chamber provides the static-magnetic field to the specimen for the electromagnetic excitation and detection of free vibration via Lorentz force mechanism and the magnetostriction force mechanism. The permanent-magnet assembly is mounted on casters, which facilitated the rotation of field direction about the cylindrical axis and selection of the detectable vibration modes.

Air or water-cooled EMAT retains compact structure and permits one-side access to a specimen even at high temperatures [46]. A short but very strong current produces high enough tangential magnetic fields near the surface region of specimen to achieve an electromagnetic coupling to a longitudinal wave. In fact, classical formulae predict that 1 T can be observed at the surface of a 2 mm diameter wire carrying 5000 A. Such a current is obtained for a short period of time by discharging a capacitor bank into the wire. The electromagnetic coupling between the EMAT and sample surface finish within a short time and then such a short life magnetic field is indeed practical.

2.4 Conclusions

EMAT theory and practice has been discussed in this Chapter. In many ways, electromagnetic acoustic transducers (EMATs) are very simple devices, but yet quite practical. Ultrasonic energy can be generated when a pulse of current through a coil is placed in a magnetic field on any electrically

conductive surface. The generation and reception of ultrasonic modes are greatly dependent upon the coil orientation and the direction of the applied bias magnetic field.

The rest of this thesis illustrates ways in which EMATs can be used effectively to make a wide range of measurements, in various of geometries, which should help to increase their range of application in NDE

2.5 References

- [1] R. B. Thompson, "Mechanisms of electromagnetic generation and detection of ultrasonic Lamb waves in iron-nickel alloy polycrystals," *J. Appl. Phys.*, vol. 48, pp. 4942-50, 12. 1977.
- [2] R. B. Thompson, "A model for the electromagnetic generation of ultrasonic guided waves in ferromagnetic metal polycrystals," *IEEE Trans. Sonics. Ultrason.*, vol. SU-25, pp. 7-15, 01. 1978.
- [3] W. P. Mason, R. N. Thurston and A. D. Pierce, *Physical Acoustics : Principles and Methods*. London : Academic Press, 1990.
- [4] K. Kawashima, "Experiments with two types of electromagnetic ultrasonic transducers," *J. Acoust. Soc. Am.*, vol. 60, pp. 365-73, 08. 1976.
- [5] K. Kawashima, "Electromagnetic acoustic wave source and measurement and calculation of vertical and horizontal displacements of surfaces waves," *IEEE Trans Sonics Ultrason*, vol. SU-32, pp. 514-22, 07. 1985.
- [6] I. V. Il'in and A. V. Kharitonov, "Theory of the EMA method of detecting Rayleigh waves for ferromagnetic and ferrimagnetic materials," *Sov. J. Nondestr. Test*, vol. 16, pp. 549-54, 07. 1980.
- [7] A. Wilbrand, "EMUS - Probes for bulk waves and rayleigh waves. Model for sound field and efficiency calculations." in *New Procedures in Nondestructive Testing*, 1983, pp. 71-80.
- [8] A. Wilbrand, "Quantitative modeling and experimental analysis of the physical properties of electromagnetic-ultrasonic transducers," *Rev. Prog. Quant. Nondestr. Eval.*, vol. 7A, pp. 671-680, 1988.
- [9] H. Ogi, "Field dependence of coupling efficiency between electromagnetic field and ultrasonic bulk waves," *J. Appl. Phys.*, vol. 82, pp. 3940-9, 10/15. 1997.

- [10] H. Ogi, E. Goda and M. Hirao, "Increase of efficiency of magnetostriction SH-Wave electromagnetic acoustic transducer by angled bias field: Piezomagnetic theory and measurement," *Jpn. J. Appl. Phys. Part 1 Regul. Pap. Short Note Rev. Pap.*, vol. 42, pp. 3020-3024, 2003.
- [11] M. R. Gaerttner, W. D. Wallace and B. W. Maxfield, "Experiments relating to the theory of magnetic direct generation of ultrasound in metals," *Phys. Rev.*, vol. 184, pp. 702-5, 08. 1969.
- [12] R. L. Wegel and H. Walther, "Internal Dissipation in Solids for Small Cyclic Strains," *Physics*, vol. 6, pp. 141-157, 1935.
- [13] R. H. Randall, F. C. Rose and C. Zener, "Intercrystalline Thermal Currents as a Source of Internal Friction," *Phys. Rev.*, vol. 56, pp. 343-348, Aug. 1939.
- [14] J. R. Houck, H. V. Bohm, B. W. Maxfield and J. W. Wilkins, "Direct Electromagnetic Generation of Acoustic Waves," *Phys. Rev. Lett.*, vol. 19, pp. 224-227, Jul. 1967.
- [15] E. R. Dobbs, "Electromagnetic generation of ultrasonic waves in metals," *J. Phys. Chem. Solids*, 1970, pp. 1657-67.
- [16] S. A. Filimonov, B. A. Budenkov and N. A. Glukhov, "Ultrasonic contactless resonance testing method," *Sov. J. Nondestruct. Test*, vol. 7, pp. 102-4, 1971.
- [17] Z. G. Nikiforenko, N. A. Glukhov and I. I. Averbukh, "Measurement of the velocity of elastic waves and acoustic anisotropy in plates," *Defektoskopiya*, pp. 74-82, 1971.
- [18] A. I. Butenko, I. N. Ermolov and Y. M. Shkarlet, "Electromagneto-acoustic non-destructive testing in the Soviet Union," *Non-Destructive Testing*, vol. 5, pp. 154-9, 06. 1972.
- [19] R. C. McMaster, American Society for Metals. and American Society for Nondestructive Testing., *Nondestructive Testing Handbook*. American Society for Metals, 1982-97.
- [20] B. W. Maxfield and C. M. Fortunko, "The design and use of electromagnetic acoustic wave transducers (EMATs)," *Mater. Eval.*, vol. 41, pp. 1399-408, 11. 1983.
- [21] G. A. Alers and L. R. Burns, "EMAT designs for special applications," *Mater. Eval.*, vol. 45, pp. 1184-9, 10. 1987.
- [22] H. Ogi, "Field dependence of coupling efficiency between electromagnetic field and ultrasonic bulk waves," *J. Appl. Phys.*, vol. 82, pp. 3940-9, 10/15. 1997.

- [23] A. Migliori and J. L. Sarrao, *Resonant Ultrasound Spectroscopy*. Chichester : Wiley, 1997.
- [24] K. Kawashima, "Nondestructive characterization of texture and plastic strain ratio of metal sheets with electromagnetic acoustic transducers," *J. Acoust. Soc. Am.*, vol. 87, pp. 681-90, 02. 1990.
- [25] K. Kawashima and O. B. Wright, "Resonant electromagnetic excitation and detection of ultrasonic waves in thin sheets," *J. Appl. Phys.*, vol. 72, pp. 4830-9, 11/15. 1992.
- [26] W. L. Johnson, S. J. Norton, F. Bendec and R. Pless, "Ultrasonic spectroscopy of metallic spheres using electromagnetic-acoustic transduction," *J. Acoust. Soc. Am.*, vol. 91, pp. 2637-42, 05. 1992.
- [27] W. Johnson, B. A. Auld and G. A. Alers, "Spectroscopy of resonant torsional modes in cylindrical rods using electromagnetic-acoustic transduction," *J. Acoust. Soc. Am.*, vol. 95, pp. 1413-18, 03. 1994.
- [28] A. V. Clark, C. M. Fortunko, M. G. Lozev, S. R. Schaps and M. C. Renken, "Determination of sheet steel formability using wide band electromagnetic-acoustic transducers," *Res. Nondestr. Eval.*, vol. 4, pp. 165-82, 1992.
- [29] M. Hirao, H. Ogi and H. Fukuoka, "Resonance EMAT system for acoustoelastic stress measurement in sheet metals," *Rev. Sci. Instrum.*, vol. 64, pp. 3198-205, 11. 1993.
- [30] G. L. Petersen, B. B. Chick, C. M. Fortunko and M. Hirao, "Resonance techniques and apparatus for elastic-wave velocity determination in thin metal plates," *Rev. Sci. Instrum.*, vol. 65, pp. 192-8, 01. 1994.
- [31] H. Ogi, M. Hirao and T. Honda, "Ultrasonic attenuation and grain-size evaluation using electromagnetic acoustic resonance," *J. Acoust. Soc. Am.*, vol. 98, pp. 458-64, 07. 1995.
- [32] S. Dixon, C. Edwards and S. B. Palmer, "Texture measurements of metal sheets using wideband electromagnetic acoustic transducers," *J. Phys. D*, vol. 35, pp. 816-24, 04/21. 2002.
- [33] M. Hirao, H. Ogi and H. Fukuoka, "Advanced ultrasonic method for measuring rail axial stresses with electromagnetic acoustic transducer," *Res. Nondestr. Eval.*, vol. 5, pp. 211-23, 1994.
- [34] W. P. Mason and Bell Telephone Laboratories., *Physical Acoustics and the Properties of Solids*. London : Van Nostrand, 1958.
- [35] H. Kwun and K. A. Bartels, "Magnetostrictive sensor technology and its applications," in *Ultrasonics International 1997*, 1998, pp. 171-8.

- [36] H. Kwun and C. M. Teller, "Magnetostrictive generation and detection of longitudinal, torsional, and flexural waves in a steel rod," *J. Acoust. Soc. Am.*, vol. 96, pp. 1202, 1994.
- [37] N. S. Tzannes, "Joule and Wiedemann Effects-The Simultaneous Generation of Longitudinal and Torsional Stress Pulses in Magnetostrictive Materials," *IEEE Trans. Sonics. Ultrason.*, vol. SU-13, pp. 33-40, 02. 1966.
- [38] T. Yamasaki, S. Tamai and I. Hirao, "Electromagnetic acoustic transducers for flaw detection in steel pipes and wires," in *Proceeding Os Symposium on Advances in NDT*, 1996, pp. 117-22.
- [39] T. Yamasaki, S. Tamai and M. Hirao, "Arrayed-coil EMAT for longitudinal wave in steel wires," *1998 IEEE Ultrasonics Symposium. Proceedings*, 1998, pp. 789-92.
- [40] H. Ogi, M. Hirao and T. Ohtani, "Line-focusing electromagnetic acoustic transducers for the detection of slit defects," *IEEE Trans. Ultrason. Ferroelectr. Freq. Control*, vol. 46, pp. 341-6, 03. 1999.
- [41] H. Ogi, M. Hirao and T. Ohtani, "Line-focusing of ultrasonic SV wave by electromagnetic acoustic transducer," *J. Acoust. Soc. Am.*, vol. 103, pp. 2411-15, 05. 1998.
- [42] K. Minoura, H. Ogi and M. Hirao, "Monitoring of rotating bending fatigue damage by axial-shear resonance using magnetostrictively-coupled EMAT," *Nippon Kikai Gakkai. Ronbunshu A, Part A*, vol. 62, pp. 2520-2526, 1996.
- [43] M. Hirao, H. Ogi and H. Yasui, "Contactless measurement of bolt axial stress using a shear-wave electromagnetic acoustic transducer," *NDT E. Int.*, vol. 34, pp. 179-183, 2001.
- [44] W. Johnson, B. A. Auld, E. Segal and F. Passarelli, "Trapped torsional modes in solid cylinders," *J. Acoust. Soc. Am.*, vol. 100, pp. 285-93, 07. 1996.
- [45] H. Ogi, S. Kai, T. Ichitsubo, M. Hirao and K. Takashima, "Elastic-stiffness coefficients of a silicon carbide fibre at elevated temperatures: acoustic spectroscopy and micromechanics modelling," *Philosophical Magazine*, vol. 83, pp. 503-12, 02/01. 2003.
- [46] L. R. Burns, D. T. MacLauchlan and G. A. Alers, "Compact EMAT receiver for ultrasonic testing at elevated temperatures," *Rev. Prog. Quant. Nondestr. Eval.*, vol. 7B, pp. 1677-1683, 1988.

Chapter 3

Application of Pulse-Compression Techniques to EMATs

As was mentioned in Chapters 1 and 2, EMATs have not yet found wide application in NDE, despite their obvious attractions as simple non-contact transducers. This is because of their low efficiency when compared to the more common piezoelectric transducers. In this Chapter, pulse-compression techniques have been applied to EMATs, using spiral pancake coils and swept-frequency (“chirp”) signals. The improvement of both signal-to-noise ratio (SNR) and data acquisition in EMAT measurements are demonstrated in this Chapter. This work has been published as a recent journal paper [1], and also as a conference presentation [2] in Canada.

3.1 Introduction

Some measurements are difficult to make with EMAT systems because of the low SNR associated with their operation, which usually necessitates signal averaging [3]. This becomes ineffective for some real-time applications, especially in situations where rapid changes in time-of-arrival or amplitude are present.

The traditional approach to drive EMATs is to employ high peak-power pulsers and low noise receivers for overcoming the lower transduction efficiency of EMATs. A high SNR ratio can be obtained by maximising the peak power delivered to the EMAT coil, and hence maximises the received signal amplitude. Recent work by Legendre *et al.* [4] uses a wavelet-transform method to analyse Lamb wave signals which were generated and received using EMATs in highly noisy environments. This technique was used for weld testing [5]. Another signal processing technique, known as cepstral analysis has also

been used to determine the separation of the peaks of the resonant frequencies, and to relate this to the time information of the received signals [6].

In this chapter, pulse-compression techniques have been applied to EMATs, using spiral coils and chirp signals. Pulse-compression has the ability to improve SNR in EMAT measurements, and thus potentially to increase the speed of measurements [7–9]. The technique has been used for air-coupled ultrasonic measurements using either polymer-filmed capacitance devices or piezoelectric devices [10–14]. It has been demonstrated in previous work that the pulse-compression signal processing technique provides an extended time waveform, such that high energy levels are transmitted, while still retaining a wide bandwidth [15]. It can also lead to excellent time resolution, while being able to recover small signals from well below the noise floor [16–17]. It was thus felt that pulse-compression was potentially a very useful method for use with EMATs in many measurements. This chapter investigates this, and illustrates the benefits in both thicknesses monitoring and imaging.

3.2 The Pulse-Compression Technique

The traditional method of using a single, simple drive pulse is limited by the radiated power, and time resolution by the pulse length. The pulse-compression technique has been developed to provide a solution for the requirements of simultaneous high SNR and resolution performance in ultrasonic systems. These are obtained without necessarily increasing the transmitter power of the drive pulse.

Pulse-compression basically involves the use of a drive waveform of a particular type, typically a long FM sweep, known as “chirp”. The received signal is cross-correlated with a replica of this signal, leading to many improvements over traditional transient excitation. The development of the pulse-compression signal processing technique allows a wide range of applications. Chang *et al.* [18] proposed the use of the pulse-compression technique for the ultrasonic testing of concrete, as ultrasound is strongly attenuated in concrete giving a low SNR. Using pulse-compression, the amount of ultrasonic energy introduced into the concrete and detected by the receiver

can be increased. After decoding the received signals, the resolution of the ultrasonic image of concrete can be enhanced as the SNR ratio is increased.

There are several papers in the literature addressing the issue of the signal compression relevant to medical diagnostic imaging. The improvement of the SNR in medical ultrasonic imaging was clearly demonstrated by Haider *et al.* [19]. Also O'Donnell *et al.* [20] demonstrated an improvement in real-time imaging system using a 3.3 MHz centre frequency coded pulse and pseudo-chirp sequence excitation. Similar results were reported by Misaridis *et al.* [21].

Various other types of coded waveforms have been investigated for use in ultrasonic measurements [22–24]. For example, there are linear frequency modulated FM, and quadratic FM signals, phase-reversal codes, polyphase phase-shift codes, frequency-shift codes, uniform pulse trains, and staggered pulse trains. The procedures and algorithms for optimally designing of a pulse-compression system have been described by Song *et al.* [25]. The procedure for selecting the best parameters of a pulse-compression system for ultrasonic imaging has been described by Behar *et al.* [26]. These include the selection of an appropriate match filtering algorithm with a good combination of amplitude weighting function. The effectiveness of an excitation/compression scheme also depends on the determination of an appropriate chirp-to-transducer bandwidth ratio, and the selection of amplitude quantisation (number of bits) when sampling.

Despite the above work, little seems to have been published on the use of pulse compression in EMAT measurements, despite the obvious attractions. This Chapter demonstrates that the approach has a real benefit. The theoretical background to pulse-compression is presented in the next Section, and this is followed by experiments demonstrating the performance of pulse compression in EMATs.

3.3 Theory

In the conventional transient excitation method, it is the large frequency content of a short pulse that accounts for its high resolution capabilities. The pulse-compression method essentially provides a long transmitted pulse, during

which the carrier frequency is swept linearly. This therefore contains the bandwidth required for the high resolution. The signal chosen for the pulse-compression system used in this study is characterised by a linear FM signal, also known as a chirp. The transmitted waveform for the linear FM pulse-compression signal can be written:

$$f(t) = \cos\left(w_0 t + \frac{\mu t^2}{2}\right) \quad (3.1)$$

where w_0 is the carrier frequency, μ is the rate of frequency sweep ($\Delta w/T$), Δw is the swept spectrum bandwidth ($\mu \times T$), and T is the pulse width. Figure 3.1(a) shows such a chirp signal. The spectrum of the linear FM signal is given by the Fourier transform, and this can be expressed as:

$$F(w) = \int_{-T/2}^{T/2} \cos\left(w_0 + \frac{\mu t^2}{2}\right) \exp(-j\omega t) dt \quad (3.2)$$

Figure 3.1(b) shows the frequency spectrum corresponding to the chirp signal in Figure 3.1(a), and Figure 3.1(c) shows the corresponding frequency time-delay characteristic. A matched filter is employed to delay one end of the pulse relative to the other (the filter having a linear time-delay vs. frequency characteristic of the opposite sense to the linear frequency sweep), which yields a correlation between time and frequency. Figure 3.1(d) shows a match-filter characteristic. The matched filter required for the receiver has an impulse response $h(t)$ that is the time inverse of the signal at the receiver input, and mathematically, $h(t)$ can be expressed as:

$$h(t) = \sqrt{\frac{2\mu}{\pi}} \cos\left(w_0 t - \frac{\mu t^2}{2}\right) \quad (3.3)$$

where $\sqrt{2\mu/\pi}$ is the factor that gives the filter unity gain. The linear time-delay characteristics of the filter acts to delay the high-frequency components at the start of the input pulse, more than the low-frequency components at the end of the pulse, with frequency components in between experiencing a proportional

delay. The output would be a time compression of the pulse which is of greater peak amplitude. Mathematically, the output of the matched filter is obtained by convolving $f(t)$ and $h(t)$, yielding:

$$g(\tau) = \int_{-\infty}^{\infty} f(t)h(\tau - t)dt \quad (3.4)$$

The matched filtering is equivalent to correlation processing. When $f(t)$ and $h(t)$ are matched, $g(\tau)$ represents the autocorrelation function of the input signal. If the signal and the filter are not matched, then $g(\tau)$ represents the cross-correlation of the two functions. The resolution (τ) depends on the transmitted pulse bandwidth (B), $\tau = 1/B$. The linear FM pulse-compression spectra are functionally dependent on the time-bandwidth factor (compression ratio). This can be expressed as:

$$\frac{P_o}{P_i} = \frac{T}{\tau} = T \times B \quad (3.5)$$

where P_o is the peak amplitude output pulse, P_i is the peak amplitude input pulse. An ideal linear FM matched filter waveform has a $(\sin x)/x$ shape (the “sinc” function). Figure 3.1(e) shows a compressed-pulse envelope.

In compressing a rectangular chirp pulse, an undesirable feature can be introduced in the form of sidelobes. In a complex interfering environment (*i.e.* the presence of multi-acoustic modes) where operation is required over a large dynamic range of received signals, the sidelobes of this function represent interfering signals. Techniques for reducing the relative side-lobe level have been extensively studied in antenna design. To suppress these sidelobes, a weighting scheme such as Hanning function (Gaussian windowing) is applied to the rectangular chirp pulse and can yield a good combination of minimising sidelobe levels whilst maintaining a high SNR. Mathematically, the weighting function is represented:

$$W(t) = \frac{1}{2} \left(1 - \cos \frac{2\pi t}{T} \right) \quad (3.6)$$

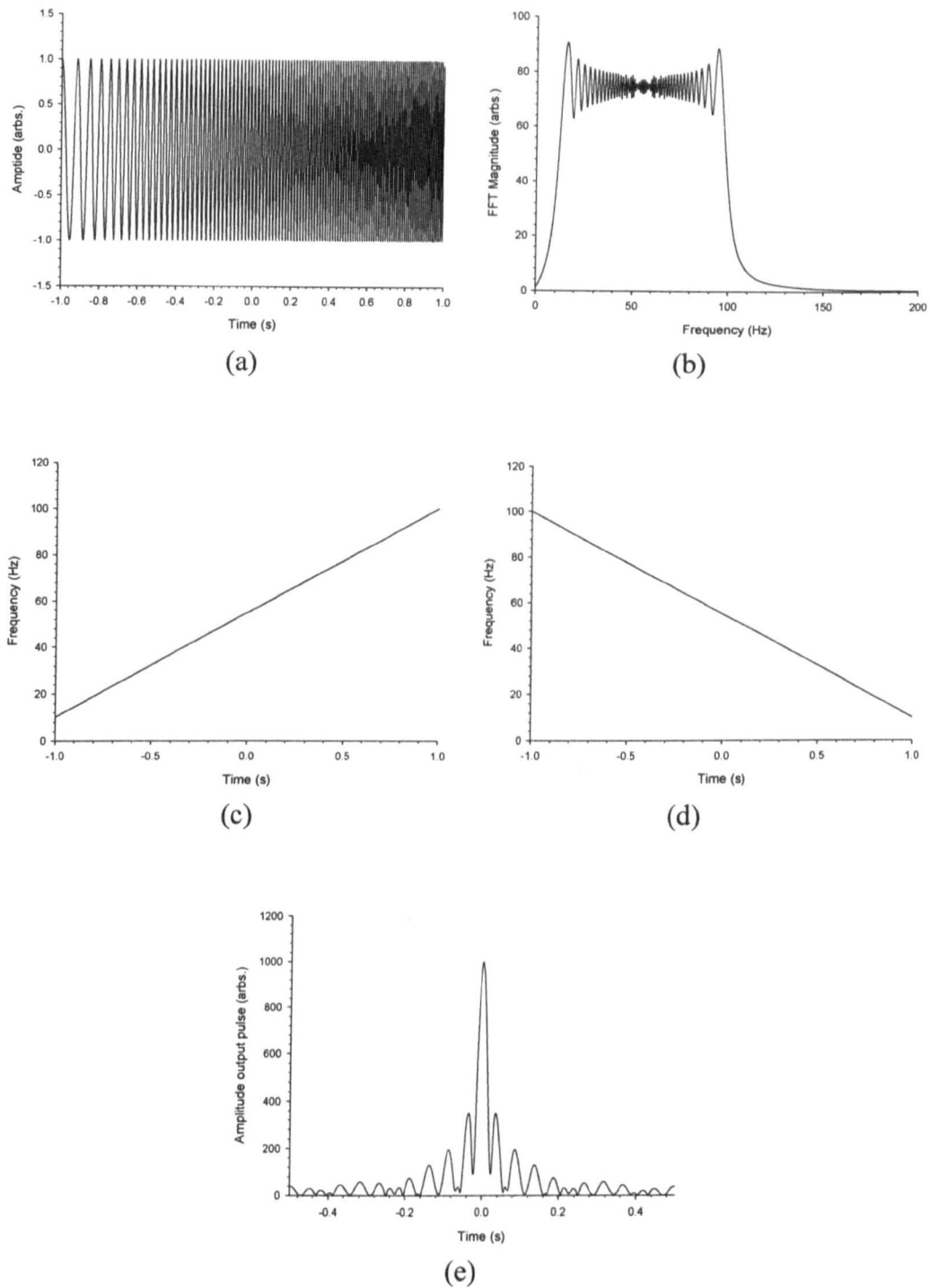


Figure 3.1: Characteristics of a typical chirp signal showing (a) the time domain waveform; (b) the corresponding frequency spectrum of (a); (c) the frequency vs. time delay characteristics of (a); (d) the equivalent matched filter characteristics, and (e) the compressed-pulse envelope.

The modulation of a rectangular chirp with a Hanning window transforms the waveform into a bell-shaped enveloped chirp signal. The Hanning window also reduces the severity of the amplitude ripples seen in the

frequency spectrum of the linear FM signal (Figure 3.1(b)) resulting in lower side-lobe level within the compressed pulse [10]. Such a reduction is accompanied by a slight, but inevitable, increase in pulse width, but leads to an improvement of the detection performance for a given peak power.

3.4 Simulations

In order to provide further understanding of the pulse-compression technique, a simulation was carried out using MatlabTM. Figure 3.2(a) shows an example of a chirp signal generated using Equation (3.1). It can be seen that the width of the signal varies with time. The duration of the chirp, T was set to 50 μs with both the centre frequency, f_c and the bandwidth, B being 2 MHz. Figure 3.2(b) shows the corresponding frequency spectrum, obtained via an FFT of Figure 3.2(a). In this simulation, it is assumed that ultrasonic waves have travelled through sample with a thickness of 50 mm and velocity of 3000 ms^{-1} . Several chirp signals with different time delays were added, assuming that multiple reflections within the sample occurred with a 35 μs round-trip time (and hence would overlap in time).

To demonstrate that the pulse-compression technique can be used to separate such multiple reflections, and to demonstrate the recovery of such signals buried in random noise, random noise at three times the amplitude of the chirp signal was added to the multiple chirp signals. This simulates the noise levels that could be encountered using EMATs. Figure 3.2(c) shows that the resultant signal is completely buried in noise and is impossible to identify without signal averaging.

The waveform in Figure 3.2(c) was then cross-correlated with the reference signal in Figure 3.2(a) and the result is shown in Figure 3.2(d). The SNR of the signal has been greatly improved compared to Figure 3.2(a). The signal has a SNR of approximately 12 dB where the standard deviation of signal and noise are approximately 15.6 and 3.8 respectively. The simulated multiple reflections can also be clearly identified at 35 μs intervals, and demonstrates that pulse-compression techniques have the ability to recover signal buried in noise without the use of signal averaging.

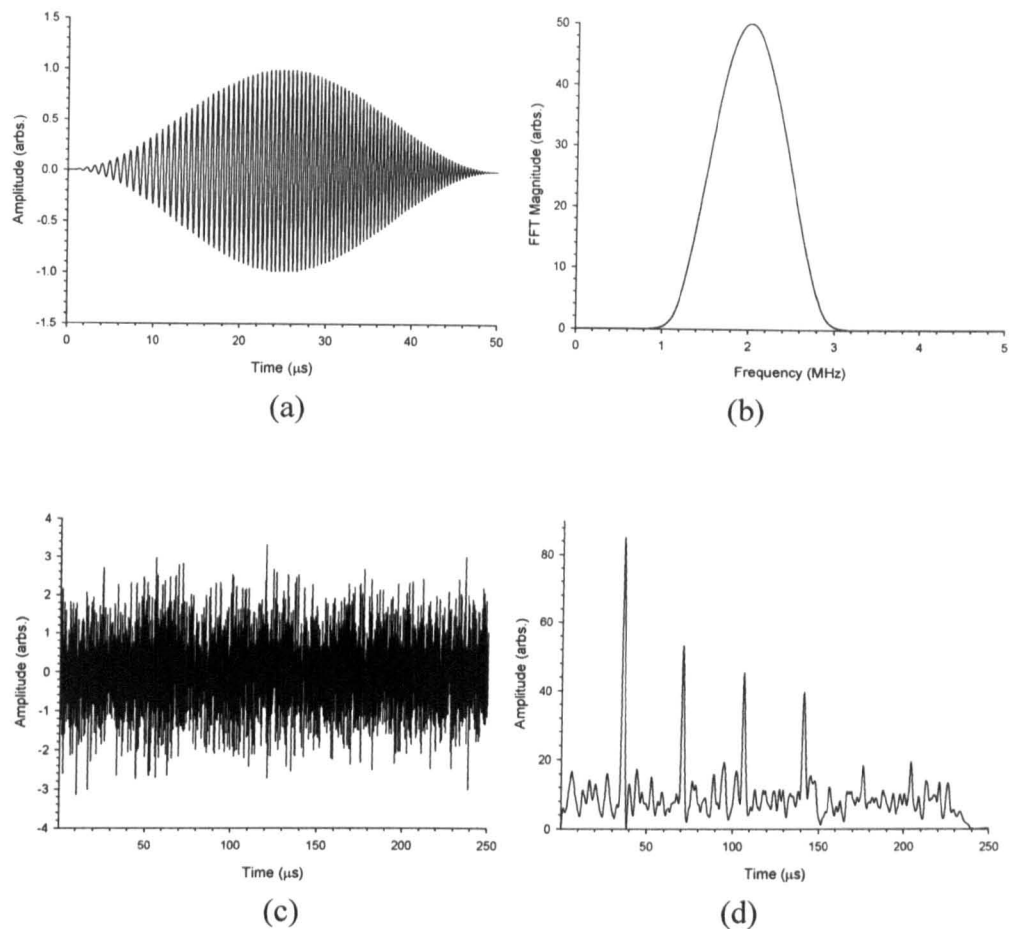


Figure 3.2: Numerical simulation of the pulse compression technique; (a) broadband reference chirp signal; (b) frequency spectrum of the reference signal; (c) simulated signal reflecting within a 50 mm thick plate with added noise, and (d) compressed signal after cross-correlation.

3.5 Experimental Arrangement

The EMAT used in the present work used a spiral pancake coil (see Figure 2.3), with 20 turns and a diameter of approximately 15 mm, with the magnet providing a magnetic field primarily in the direction normal to the surface. The first experiment characterised the bandwidth of the transducer in through-transmission mode within a 10 mm thick aluminium plate, using conventional transient excitation. The experimental setup is shown in Figure 3.3. A Panametrics pulser/receiver was used to drive the EMAT with a -250V transient signal. The captured echo was sent to an Agilent oscilloscope for recording and signal averaging.

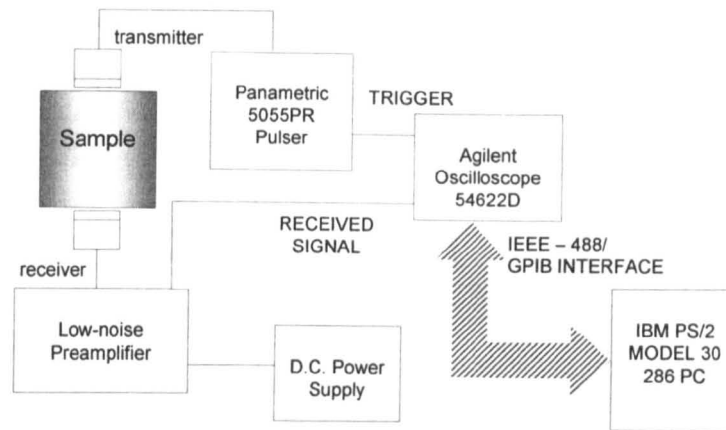


Figure 3.3: Basic through-transmission arrangement for characterisation of an EMAT using conventional transient excitation.

Figure 3.4(a) shows the single-shot waveform that resulted (*i.e.* without signal averaging). The radially-polarised shear wave signal that was recorded on the oscilloscope was weak and could not be clearly seen, as it was buried in noise. By averaging the signal over 1000 times on the oscilloscope, the SNR improved, as shown in Figure 3.4(b). Figure 3.4(c), showing the FFT of the signal in Figure 3.4(b), and indicates that the EMAT had a 3 dB bandwidth of approximately 6 MHz. The air gap distance of the EMATs and the test sample was ~ 1 mm. However, the use of a high degree of averaging is inefficient, especially for possible application to online measurements and non-contact imaging via scanning and arrays.

Experiments were also carried out using the pulse-compression technique, using the arrangement shown in Figure 3.5. The pulse-compression approach was implemented using a VN Instruments NCA-1000 pulser/receiver unit, which provided a chirp signal voltage drive signal and pulse-compression facilities for the receiver. The input signal to the source EMAT was a chirp signal with a centre frequency, f_c and bandwidth, B both set at 2 MHz. The chirp duration, T was 200 μ s. Radially-polarised ultrasonic signals generated by the source propagated through the sample, and the through-transmitted signal were received by the second EMAT. The output from the receiver was fed back into the NCA-1000 pulse-compression unit for data analysis. The pulse-compressed data was then recorded using a Tektronix TDS540 digital

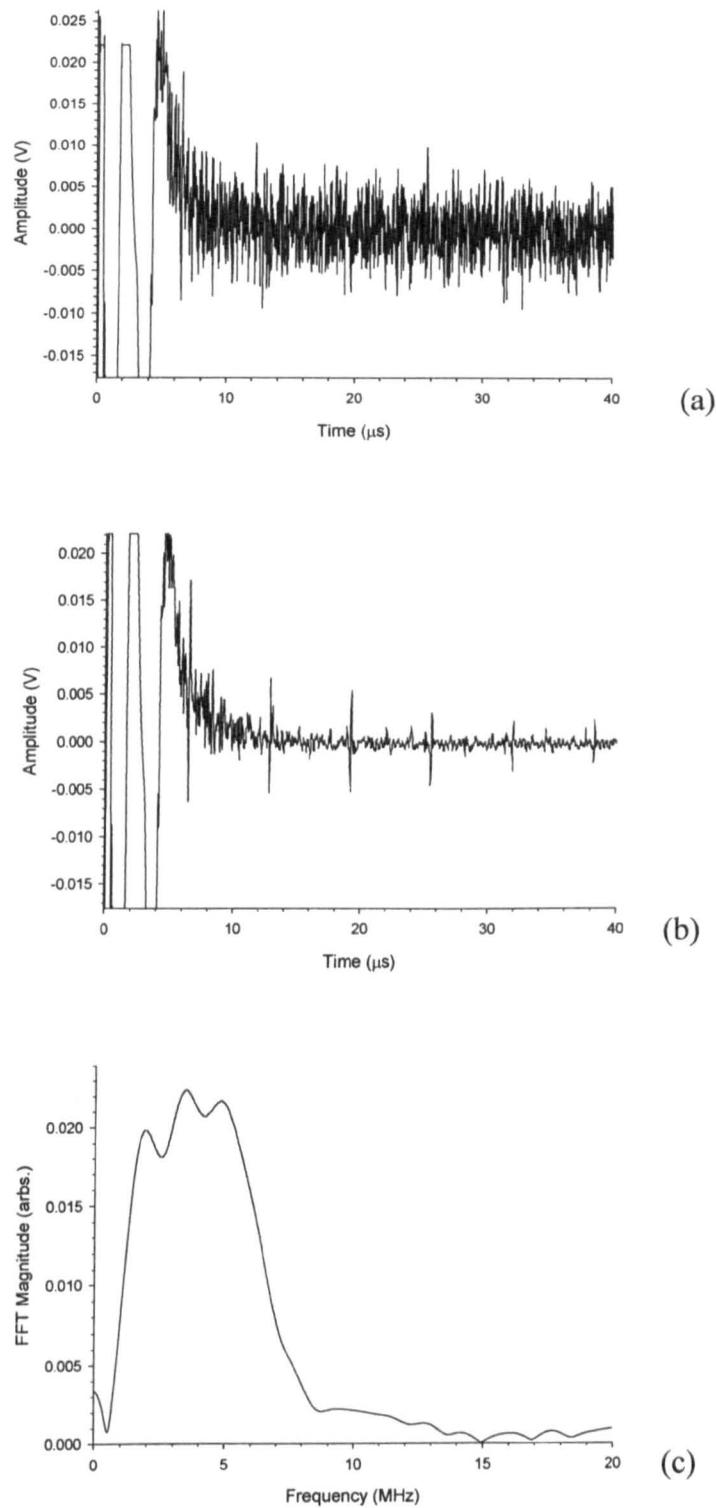


Figure 3.4: Characterisation of the pancake coil EMAT shown in Figure 2.3 in a 10 mm thick aluminium plate, using the apparatus of Figure 3.3. Shown are (a) a single shot waveform; (b) the result following 1000 averages, and (c) the spectrum resulting from the FFT of (b).

oscilloscope, before being transferred to a PC for data storage. Imaging was also possible, using an X-Y scanning stage, as shown in the Figure 3.5. The PC used for data collection was also used to control the X-Y stages. The total area of the scan was set to 60 mm \times 60 mm, at spatial intervals of 1 mm. The system has a data acquisition rate of 0.5 unit point/second, which corresponds to a 2Hz sampling rate. All scanning and data acquisition was controlled by LabViewTM software. This software also extracted peak amplitude data of the transmitted signal from each waveform in the scan, and stored the data into a grid file format. The image was then plotted using SurferTM version 7.0 software.

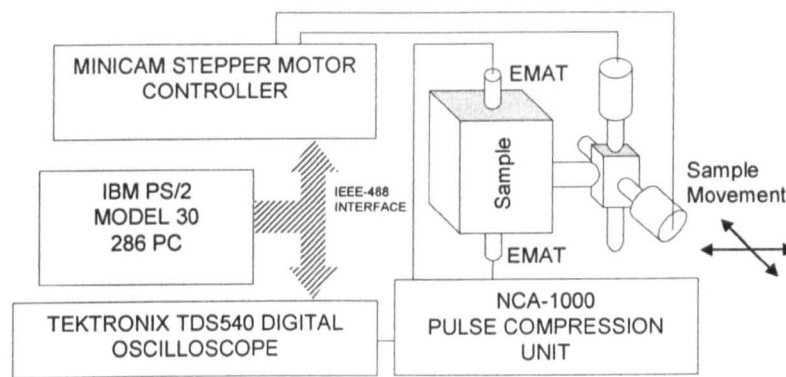


Figure 3.5: *Experimental arrangement for through-transmission measurements and imaging using two spiral pancake coil EMATs.*

3.6 Results and Discussion

The pulse-compression EMAT system has been compared to results obtained using conventional transient excitation, and used for both thickness measurements and ultrasonic imaging.

The combination of EMAT devices and pulse-compression was first tested on a 6.25 mm thick aluminium alloy plate. Figure 3.6(a) shows an example of a reference chirp waveform that has been used in pulse-compression signal processing. This chirp has the characteristic shape which results from the application of a Hanning window. The wide bandwidth of the chirp signal can be illustrated by performing a Fourier transform of Figure 3.6(a), with the result shown in Figure 3.6(b). The Hanning chirp signal was now applied to one of the EMATs, operating as a transmitter.

The chirp signal was transmitted across a 6 mm thick aluminium plate, and was then detected by another EMAT axially aligned on the opposite side. The chirp signal recorded by the receiver, prior to pulse-compression processing, is shown in Figure 3.6(c). It is difficult to identify the arrival time of individual signals, as most of the arrivals overlap. In order to identify each of the transmitted signals, including multiple reflections within the sample; pulse-compression was performed using the reference signal in Figure 3.6(a) and the received signal in Figure 3.6(c). The resultant waveform, shown in Figure 3.6(d), clearly shows the individual signals, represented as the monopolar peaks (expected from the simulations shown earlier in Figure 3.2(d)).

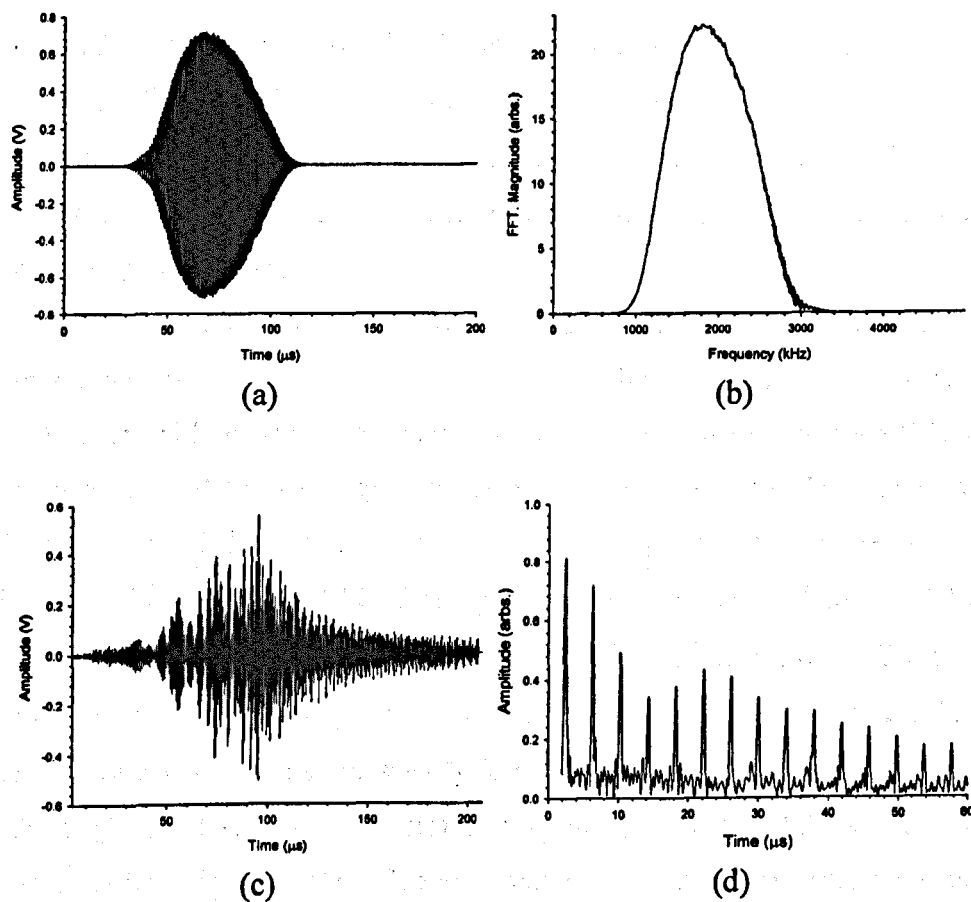


Figure 3.6: Results illustrating the use of the pulse compression technique to the spiral coil EMAT. (a) Chirp signal generated by the NCA 1000 unit and used as a reference signal; (b) FFT of the signal in (a); (c) unprocessed signal detected after propagation through a 6mm thick aluminium sample, and (d) compressed pulse resulting from the cross-correlation of signals (a) and (c).

Calculations using the arrival time of the peaks gave a wave velocity of $3150 \pm 8 \text{ ms}^{-1}$ (corresponding to an uncertainty of $\sim 0.25\%$). This agrees with published results for the shear velocity in aluminium of 3150 ms^{-1} [27]. There is also a good SNR, approximately 18 dB, where the standard deviation of the signal and noise are 0.24 and 0.029 respectively. The advantage of this technique is that the signal can be identified without the use of large amount of averaging to remove the background noise. These conclusions agree with the simulation Section.

The transducer pair was tested on a thinner (2.25 mm thick) aluminium plate, where the measurement would be more difficult because of overlap of echoes. The EMAT pair was first driven using a Panametrics pulser/receiver. The captured signal without any averaging is shown in Figure 3.7(a). It can be seen that no signal was visible above the noise. The SNR was improved by averaging 1000 signals on the oscilloscope, so that the signal was then identifiable (Figure 3.7(b)). The time taken for averaging was approximately 10 s. Although the noise had been removed, it was difficult to determine the first arrival of each transmitted component, as the signals were overlapping each other.

Figure 3.8 shows the result obtained using a chirp drive signal and pulse-compression, with no signal averaging. The arrival time of each peak can be clearly seen without any overlapping of signals, with a reasonable SNR. This demonstrates that the technique can be used to improve the SNR, and would allow more rapid data acquisition when performing on-line measurements. To illustrate this further, the EMAT-compression system was applied to a 10 mm thick aluminium plate and a block of brass with a thickness of 31.8 mm, the results being shown in Figures 3.9 and 3.10 respectively. In Figure 3.9, the shear wave reflections can be clearly identified. Figure 3.10 demonstrates that both longitudinal (L1, L3, L5 etc) and shear signals (S1, S3, S5 etc) were detected following multiple reflections and mode conversion within the brass block, identified from their propagation times across the sample. Note that the amplitude of the longitudinal signal was smaller than that of the shear wave; although the pancake-coil EMAT was optimised for shear waves, some sensitivity to longitudinal waves was present due to field fringing and other effects.

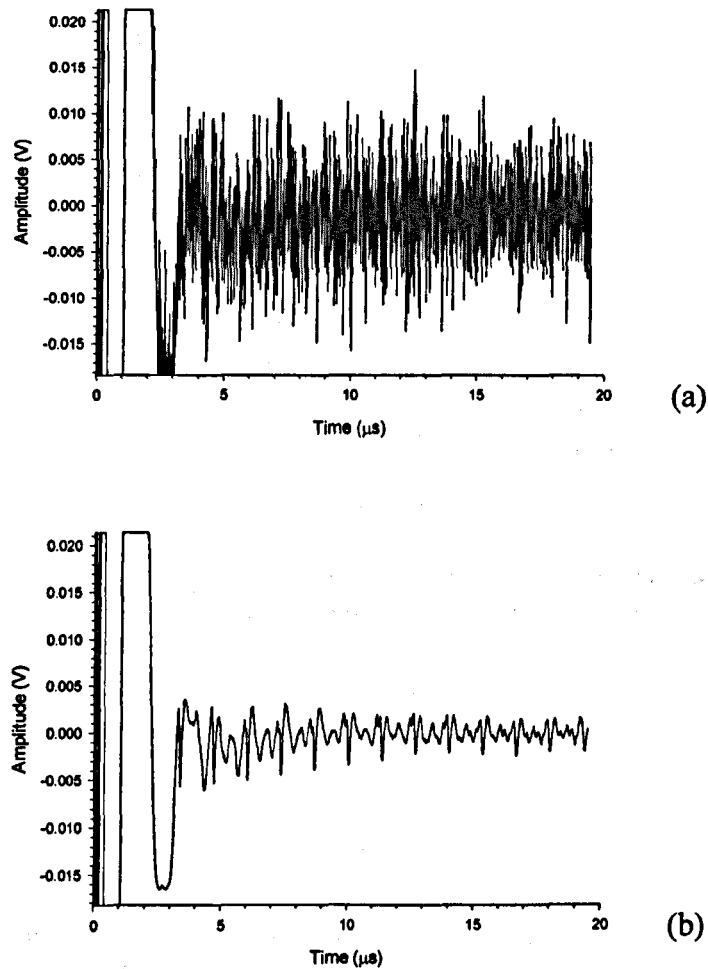


Figure 3.7: Through-transmitted signal across a 2.25 mm aluminium plate using (a) the Panametrics pulser/receiver with no averaging, (b) The Panametrics pulser/receiver with 1000 averages.

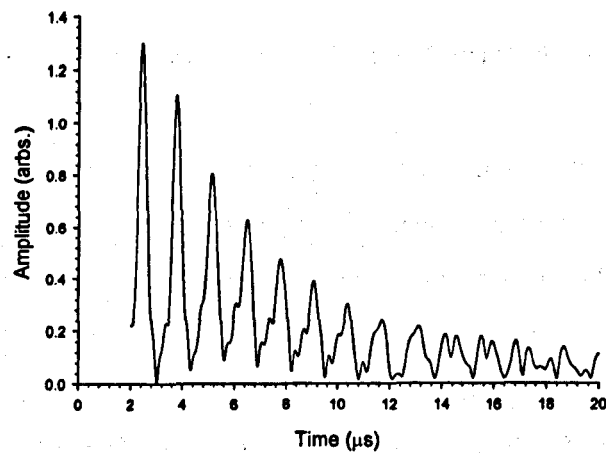


Figure 3.8: Through-transmitted signal across a 2.25 mm aluminium plate after using pulse compression without averaging.

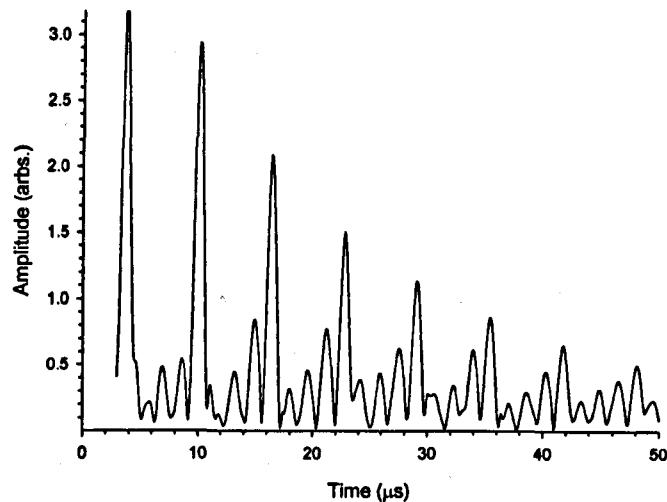


Figure 3.9: Example of the pulse compression output signal obtained across a 10 mm thick aluminium in through transmission mode.

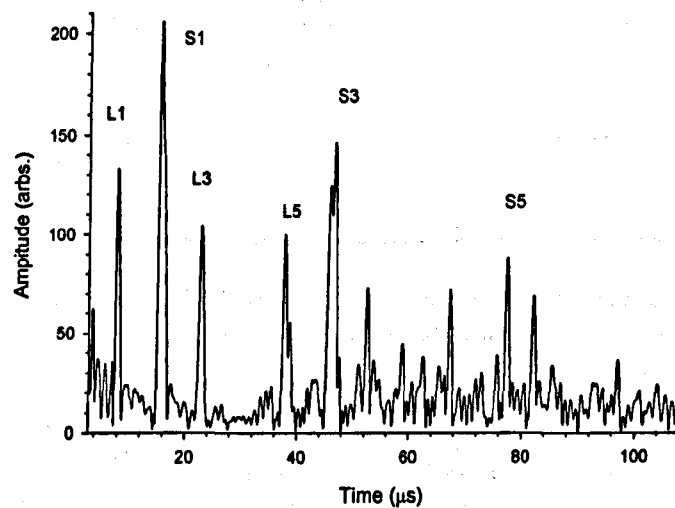


Figure 3.10: As Figure 3.8, but for a 31.8 mm thick brass plate.

Thickness measurements were performed on various metallic samples, including aluminium, brass and copper. The measurements were then compared with those from a Kennedy digital vernier caliper model 331-206. Figure 3.11 shows the results obtained using EMATs and pulse-compression system. This is indicated as circle in the figure. The results are compared to those measured using a vernier caliper shown as square. Table 3.1 and 3.2 show the measured values for brass and copper, including the calculated difference between the two

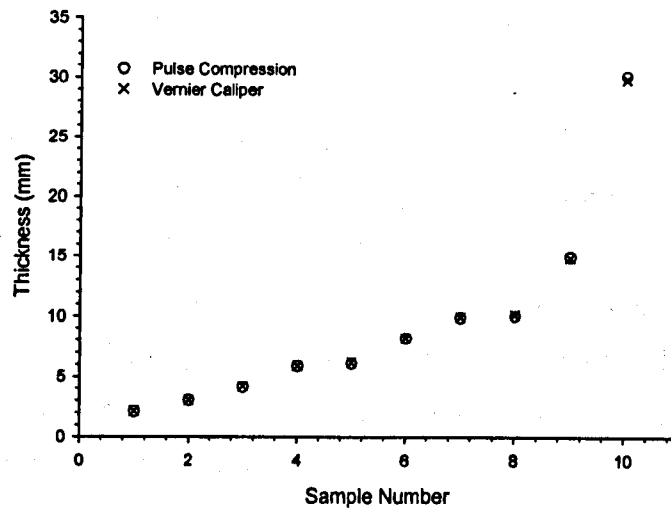


Figure 3.11: Thickness measurements of aluminium plates using EMATs and pulse-compression system (circles). The results are compared to those measured using a vernier caliper gauge, shown as squares.

Sample No.	Ultrasonic measurement (mm)	Vernier calliper (mm)	Percentage Error
1	3.95	4.00	1%
2	7.14	7.19	1%
3	9.89	9.96	1%
4	13.71	13.8	1%
5	16.83	16.9	0%

Table 3.1: Comparison of thickness measurements using a vernier caliper and EMAT pair of various brass plates.

Sample No.	Ultrasonic measurement (mm)	Vernier calliper (mm)	Percentage Error
1	5.00	5.00	0
2	7.77	7.84	1%
3	10.25	10.30	0%
4	13.00	13.17	1%
5	15.10	15.03	0%

Table 3.2: Same as Table 3.1 but with copper plates were used.

measurements. The results indicate that the measured thicknesses using the EMAT-compression system is well correlated with the vernier caliper.

Some ultrasonic imaging was now performed using the pulse-compression EMATs. The EMATs were first scanned in unison over the 6mm

aluminium plate, into which was machined a 6.5 mm diameter circular flat-bottomed hole of 3 mm depth. The first image, shown in Figure 3.12(a), was obtained using an EMAT pair driven by the Panametrics pulser/receiver system with 20 averages on the oscilloscope. The illustrated image shows that the defect is unclear. By increasing the averaging to 200 on the oscilloscope, the resolution of the image is improved and this is shown in Figure 3.12(b). The scan was then repeated using the pulse-compression approach with only 20 averages on the oscilloscope. It can be seen that the image in Figure 3.12(c) is much clearer compared to Figures 3.12(a) and 3.12(b). It can also be seen from these images that the EMAT pair is very sensitive to the change in air gap between the transducers and the sample, shown by the gradual DC shift across the images, caused by slight misalignment between the scanning stage and the sample.

Some additional images were created with an aluminium sample. Scans were performed on a sample with an internal defect in through-transmission. The defect is a 3.4 mm diameter hole located at the centre of the face of a uniform cross-section area. The cross-section is 10 mm thick, and the defect itself extended through 28 mm into the bulk of the specimen perpendicular to the cross-sectional face. Figure 3.13(a) was obtained using an EMAT pair driven by the Panametrics pulser/receiver system with 20 averages on the oscilloscope, and Figure 3.13(b) was driven by pulse-compression unit with 20 averages on the oscilloscope. It can be seen from these images that the results obtained from pulse-compression is much clearer than with a broadband pulse at the same level of averaging.

3.7 Conclusions

In conclusion, this chapter has shown that pulse-compression signal processing techniques can be applied to EMATs, due to their wide bandwidth. This leads to a wide range of possible applications. It has been demonstrated that measurements of various thicknesses of metal plates can be conducted. This work also shows that the use of the pulse-compression processing technique

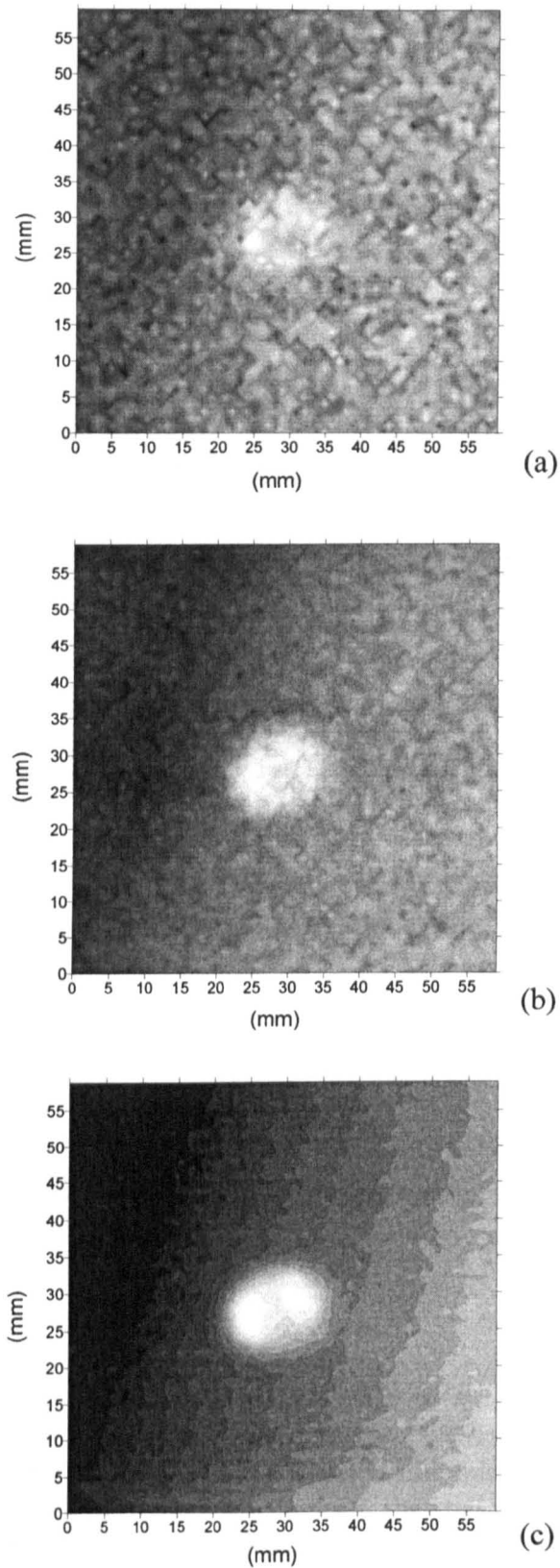


Figure 3.12: Through transmission images of a 6 mm thick aluminium plate having a 6.5 mm diameter circular hole, machined into one surface to a depth of 3 mm. (a) Panametrics pulser/receiver with 20 averages; (b) Panametrics pulser/receiver with 200 averages and (c) pulse compression signal processing technique using 20 averages.

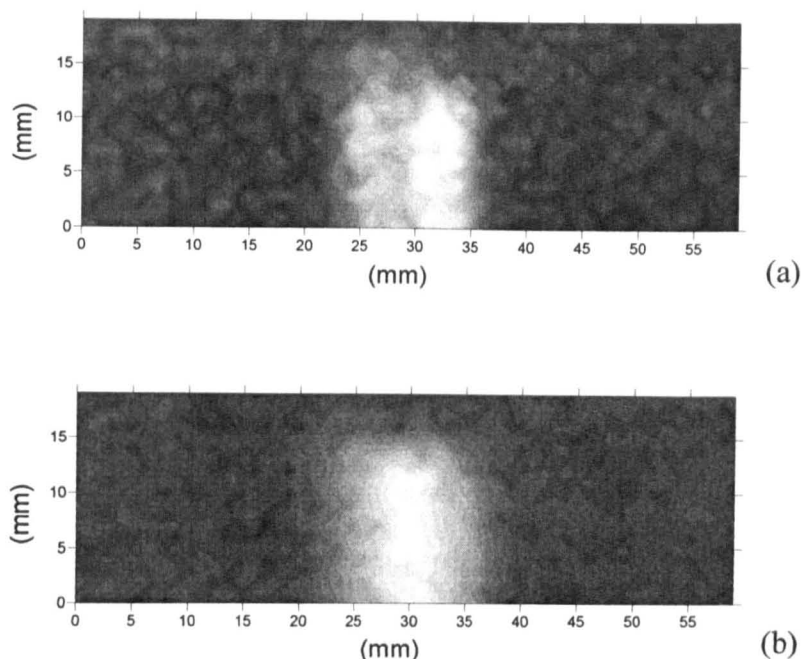


Figure 3.13: Through-transmission internal defect images in aluminium plate. (a) Image obtained using Panametrics-NDT pulse/receiver with 20 averages; (b) image obtained using pulse compression unit with the same number of averages.

reduces the amount of averaging required for data acquisition and thus improves the time taken for imaging and real time measurements. It is thus suggested that the combination of EMATs and pulse-compression can lead to a wide range of applications, such as on-line testing where fast time acquisition is required, and discrimination between multiple arrivals. In Chapter 4 to follow, a pulse-compression EMAT system is used for tomographic imaging in beverage cans, where the advantages of pulse-compression are further illustrated.

3.8 References

- [1] K. S. Ho, T. H. Gan, D. R. Billson and D. A. Hutchins, "Application of pulse compression signal processing techniques to electromagnetic acoustic transducers for noncontact thickness measurements and imaging," *Rev. Sci. Instrum.*, vol. 76, pp. 54902-1, 05. 2005.
- [2] T. H. Gan, K. S. Ho, D. R. Billson and D. A. Hutchins, "Application of pulse compression signal processing techniques to electromagnetic acoustic transducers for noncontact thickness measurements and imaging," in *16th WCNDT 2004 - World Conference on NDT*, 2004, pp. 51.

- [3] G. M. Graham and I. C. Ume, "Automated system for laser ultrasonic sensing of weld penetration," *Mechatronics*, vol. 7, pp. 711-21, 12. 1997.
- [4] S. Legendre, D. Massicotte, J. Goyette and T. K. Bose, "Wavelet-transform-based method of analysis for Lamb-wave ultrasonic NDE signals," *IEEE Trans. Instrum. Meas.*, vol. 49, pp. 524-30, 06. 2000.
- [5] S. Legendre, D. Massicotte, J. Goyette and T. K. Bose, "Neural classification of Lamb wave ultrasonic weld testing signals using wavelet coefficients," *IEEE Trans. Instrum. Meas.*, vol. 50, pp. 672-8, 06. 2001.
- [6] D. A. Hutchins, M. D. C. Moles, G. S. Taylor and S. B. Palmer, "Non-contact ultrasonic inspection of diffusion bonds in titanium," *Ultrasonics*, vol. 29, pp. 294-301, 07. 1991.
- [7] M. Pollakowski and H. Ermert, "Chirp signal matching and signal power optimization in pulse-echo mode ultrasonic nondestructive testing," *IEEE Trans. Ultrason. Ferroelectr. Freq. Control*, vol. 41, pp. 655-9, 1994.
- [8] N. A. H. K. Rao, "Investigation of a pulse compression technique for medical ultrasound: a simulation study," *Med. Biol. Eng. Comput.*, vol. 32, pp. 181-188, 1994.
- [9] B. Koehler, G. Hentges and W. Mueller, "Improvement of ultrasonic testing of concrete by combining signal conditioning methods, scanning laser vibrometer and space averaging techniques," *NDT E Int.*, vol. 31, pp. 281-287, 1998.
- [10] T. H. Gan, D. A. Hutchins, D. R. Billson and D. W. Schindel, "The use of broadband acoustic transducers and pulse-compression techniques for air-coupled ultrasonic imaging," *Ultrasonics*, vol. 39, pp. 181-94, 04. 2001.
- [11] T. H. Gan, D. A. Hutchins and D. R. Billson, "Preliminary studies of a novel air-coupled ultrasonic inspection system for food containers," *J. Food Eng.*, vol. 53, pp. 315-323, 2002.
- [12] E. Blomme, D. Bulcaen and F. Declercq, "Air-coupled ultrasonic NDE: experiments in the frequency range 750 kHz-2 MHz," *NDT E Int.*, vol. 35, pp. 417-26, 10. 2002.
- [13] E. Blomme, D. Bulcaen and F. Declercq, "Recent observations with air-coupled NDE in the frequency range of 650 kHz to 1.2 MHz," *Ultrasonics*, vol. 40, pp. 153-7, 05. 2002.
- [14] T. Folkestad and K. S. Mylvaganam, "Chirp excitation of ultrasonic probes and algorithm for filtering transit times in high-rangeability gas flow metering," *IEEE Trans. Ultrason. Ferroelectr. Freq. Control*, vol. 40, pp. 193-215, 05. 1993.

- [15] M. Pollakowski, H. Ermert, L. von Bernus and T. Schmeidl, "The optimum bandwidth of chirp signals in ultrasonic applications," *Ultrasonics*, vol. 31, pp. 417-20, 11. 1993.
- [16] Y. Iizuka, "High signal-to-noise ratio ultrasonic testing system using chirp pulse compression," *Insight Non Destr. Test Cond. Monit.*, vol. 40, pp. 282-5, 04. 1998.
- [17] M. Yoshino, R. Okuno, A. Nagamune and K. Nishifuji, "Next generation on-line ultrasonic testing system, using real-time chirp pulse compression processing," *Mater. Sci. Forum*, 1996, pp. 791-8.
- [18] Y. Chang and C. Lee, "Pulse compression technique applied to ultrasonic nondestructive testing of concrete," *J. Chin. Inst. Eng. Trans. Chin. Inst. Eng. Ser. A*, vol. 27, pp. 187-192, 2004.
- [19] B. Haider, P. A. Lewin and K. E. Thomenius, "Pulse elongation and deconvolution filtering for medical ultrasonic imaging," *IEEE Trans. Ultrason. Ferroelectr. Freq. Control*, vol. 45, pp. 98-113, 01. 1998.
- [20] M. O'Donnell, "Coded excitation system for improving the penetration of real-time phased-array imaging systems," *IEEE Trans. Ultrason. Ferroelectr. Freq. Control*, vol. 39, pp. 341-51, 05. 1992.
- [21] T. X. Misaridis, K. Gammelmark, C. H. Jorgensen, N. Lindberg, A. H. Thomsen, M. H. Pedersen and J. A. Jensen, "Potential of coded excitation in medical ultrasound imaging," *Ultrasonics*, , vol. 38, pp. 183-9, 03. 2000.
- [22] S. M. -. Song, W. -. M. Kim and Myung-Su Lee, "Optimization of radar pulse compression processing," *Proc. SPIE - Int. Soc. Opt. Eng.*, 1997, pp. 211-16.
- [23] V. Behar and D. Adam, "Parameter optimization of pulse compression in ultrasound imaging systems with coded excitation," *Ultrasonics*, vol. 42, pp. 1101-9, 08. 2004.
- [24] F. E. Nathanson, J. P. Reilly and M. N. Cohen , *Radar Design Principles : Signal Processing and the Environment*. London : McGraw-Hill, 1991.
- [25] C. E. Cook and M. Bernfeld, *Radar Signals: An Introduction to Theory and Application*. New York & London, 1967.
- [26] A. W. Rihaczek, *Principles of High-Resolution Radar*. London : Artech House, 1996.
- [27] J. Blitz, *Fundamentals of Ultrasonics*. London: Butterworths, 1967.

Chapter 4

Inspection of Drinks Cans using EMATs

This chapter investigates whether EMATs can be used, together with pulse-compression, to produce images of cross-sections through objects such as drinks cans. In particular, the increase in SNR level, and the ability to distinguish between different signal components, was considered to be a great advantage. This work has been published as a journal paper [1]. The chapter contains a description of the tomographic image reconstruction method used, and described how the use of pulse-compression leads to efficient separation of wanted signals from a complicated received signal.

4.1 Introduction

The detection and identification of foreign bodies in food and drink containers is becoming increasingly important for quality assurance. This is due to both increasing customer expectations and escalating litigation costs arising from contamination. Consequently, it is desirable that all such contamination is detected and removed before the product reaches the consumer. A foreign body, which refers to any unwanted object in a food product [2], is often introduced when food products are manufactured or packaged. Examples include metal or glass fragments, or other form of contaminants that have accidentally been introduced into the container either before or during filling. It is thus of major concern to the food industry that practical tools are available to identify and characterise the contents of containers. While this can be achieved by removing samples and performing tests off-line, it would also be helpful if an on-line non-destructive testing method was available.

Several authors have presented methods for detection and removal of foreign bodies, with discussion of existing techniques including metal detection, magnets, optical sorting, and physical separation methods [3]. Other potential

new technologies include surface penetrating radar, microwave techniques, nuclear magnetic resonance (NMR) [4], and near infrared (NIR) spectroscopy [5], although electromagnetic methods can only be used on non-metallic containers. NIR is particularly useful in that it is non-contact, and can be used to characterise a wide range of food types. NIR spectroscopy has been shown to provide rapid and non-destructive measurements of internal properties such as soluble solids concentration (SSC) and dry matter for many fruits and vegetables [6]. NIR spectroscopy has been shown to be useful for the detection of selected contaminants such as fecal matter in poultry [7] and the detection of changes in the properties of the skins of chickens [8]. γ -ray testing of containers has also been reported [9].

Ultrasound-based methods are well suited for food inspection. For example, Povey *et al.* [10] provided an account of ultrasound in food processing applications. More recently, research has been carried out to detect and identify foreign bodies in cheese using ultrasound [11]. The problem with conventional ultrasound is that it requires the transducers used to generate and detect ultrasonic signals to either touch the container or to use some form of liquid couplant. Both can be inconvenient. Thus, various authors have investigated non-contact methods whereby ultrasonic testing can be achieved. One approach is to use air-coupled ultrasound. This has been achieved in polymer-based soft drink bottles and microwaveable food containers [12]. Detection of almond nuts in milk chocolate using air-coupled transducers has been described [13], and the use of ultrasonic reflectance spectroscopy to characterise some aerated foods has also been demonstrated [14]. Another approach for non-contact ultrasonic inspection is to use electromagnetic acoustic transducers (EMATs). This approach, which requires the containers to be electrically-conducting, has been described in several papers [15, 16] using either EMATs only or with some other form of non-contact excitation (such as a plasma discharge or a pulsed laser source).

The work presented in Chapter 3 demonstrated that the pulse compression signal processing technique could be applied to EMATs for the non-destructive testing of metals. Here the work is extended by applying the technique specifically to EMATs for the tomographic imaging of metallic drinks

containers. The use of air-coupled inspection can be difficult in such situations, especially with thick-walled and highly curved containers, where refraction at air/metal interfaces is a problem. EMATs would have no such restrictions. In addition, as will be seen, the technique allows the separation of signals that have travelled through the liquid within the container (and which are wanted for imaging) from the guided Lamb waves that have travelled around the outside of the container. These latter signals potentially overlap in time with signals passing through the liquid, and could cause the identification of the correct signals to be very difficult. The use of chirp signals and cross correlation allows identification of each particular propagation mode, and hence selection of the correct signals for imaging. It will be demonstrated that this approach leads to the possibility of both liquid level estimation and foreign body detection.

In this chapter, EMATs have been used to both generate and detect ultrasonic waves in cylindrical beverage containers, but for the first time they have been used with chirp signal excitation and pulse compression for tomographic imaging and level detection. As will be seen, this has particular advantages for the selection of the correct propagation mode.

4.2 Tomographic Reconstruction Techniques

EMATs have been scanned over the surface of cylindrical metal drinks cans, and cross-sectional images of the internal contents produced using ultrasonic computed tomography. The filtered back-projection algorithm was chosen [17], as this is the algorithm now used by almost all commercially-available X-ray CT scanners. It has been shown [18] that the filtered back-projection algorithm is very suitable for data in a cylindrical geometry, and hence it was chosen for the present study. It should be noted, however, that care has to be taken with the exact geometry of data collection, as this has to be interpolated for input to the reconstruction algorithm. The equi-angular sampling geometry was employed in this study. A series of projections were generated using a stationary EMAT transmitter, with an EMAT receiver scanned around the cylindrical container to form a single fan-beam projection. Details of the fan-beam reconstruction theorem are given in [17].

Figure 4.1 shows the fan beam coordinate system and variables used in reconstruction. The transmitter is first located at O and α is the projection angle. M is the rotation centre and Cartesian origin of the system. Receiver positions are positioned along the arc FK , symmetrically about the middle ray OM . The receiver spacing being considered is equi-angular with an angle increment of $\Delta\theta$. The receiver angle θ is measured with respect to the central ray ($\theta = 0$) and ranges from $-\theta_m$ to θ_m . The next projection can be taken if the whole system is rotated about M by incrementing the projection angle α . In the most straightforward implementation α covers a complete rotation.

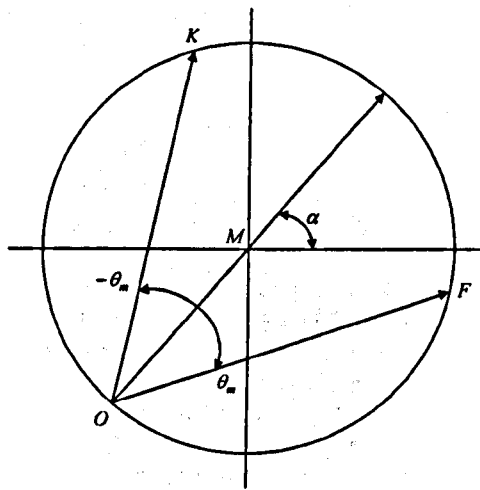


Figure 4.1: The fan beam coordinate system and variables used in reconstruction.

In this work, EMATs will be used to produce measurements in metallic food containers, using a combination of pulse compression and tomographic imaging. As outlined above, this gives the distinct advantage over other approaches that mode separation and signal to noise enhancement is possible simultaneously, allowing the measurement to take place much more easily. Note that pulse compression can also be used for air-coupled ultrasound, in both conventional imaging and tomography, as previous publications involving the authors have demonstrated [18, 19]. However, here the effects of refraction at the air/metal boundary can be significant at highly-curved surfaces. EMATs do not have this problem, as the signal is generated within the metal itself.

4.3 Experimental Setup

The EMAT coil configuration, fabricated using printed-circuit techniques, is shown schematically in Figure 4.2. The coil had 10 turns with an outer diameter of 10 mm. The track width and clearance were both set at approximately 0.2 mm. The coil layer was etched on a 1.55 mm double-sided FR4 PCB above a low impedance ground plane, and coated with a clear lacquer layer for insulation. The EMAT coil was placed against the flat face of circular disc-shaped magnet to provide a magnetic field primarily in the direction normal to the sample surface. A neodymium-iron-boron sintered magnet was used, with a maximum flux density B_r of $\sim 1.5\text{T}$.

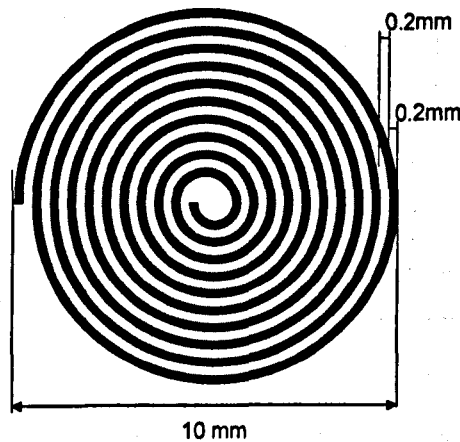


Figure 4.2: The spiral-coil geometry used in the EMAT.

The experimental configuration for collecting preliminary ultrasonic data, using conventional pulsed excitation (*i.e.* without chirp excitation and pulse compression) is shown schematically in Figure 4.3. The EMATs were located close to the sample, with an air-gap of typically ~ 0.3 mm, to allow high energy coupling between the EMATs and the metal surface. The sample aluminium container had an outer diameter of approximately 66 mm and a wall thickness of 0.15 mm, as measured with a micrometer. Experiments were performed in a through-transmission arrangement using two identical EMATs. The container was filled with tap water, and a longitudinal wave was transmitted directly across the sample. The source EMAT was driven with a -

400 V unipolar pulse from a Panametrics 5055PR pulse generator, with minimum damping. A high-gain, wide-bandwidth preamp was attached to the EMAT receiver. The preamp had a typical gain-bandwidth product of ~ 12.5 GHz. A high-pass filter was used to remove any low frequency noise, with the -3dB cut-off was chosen at 300 kHz. The time waveform was then recorded on an Agilent 54622D digital oscilloscope, with 512 signal averages. All measurements were taken at ambient laboratory conditions.

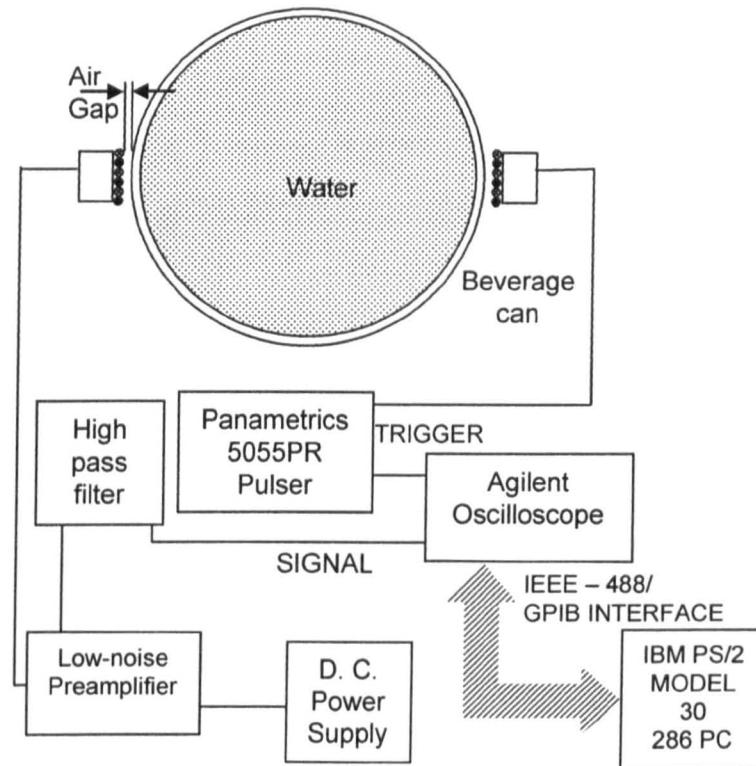


Figure 4.3: Schematic diagram of the experimental configuration used for collecting data using transient (pulsed) excitation.

The above describes how signals were obtained using conventional pulsed excitation. However, as will be seen later, it is possible to enhance the amplitude of the wanted L mode with respect to the other unwanted signals using pulse compression and careful control of chirp characteristics. The apparatus used for this is shown in Figure 4.4, which also shows the scanning system required for tomographic imaging. The chirp signal and cross-correlated processing was performed in real time, using a VN Instruments (NCA-1000) pulser/receiver unit. The input signal to the source EMAT was a linear-swept

frequency chirp signal with a centre frequency, f_c and bandwidth, B both set at 1 MHz. The chirp duration, T was 200 μ s, and transmitted chirp amplitude was 120 V (peak-peak). The same PC controlled the scanning system and the data acquisition for the collection of pulse compression output waveforms.

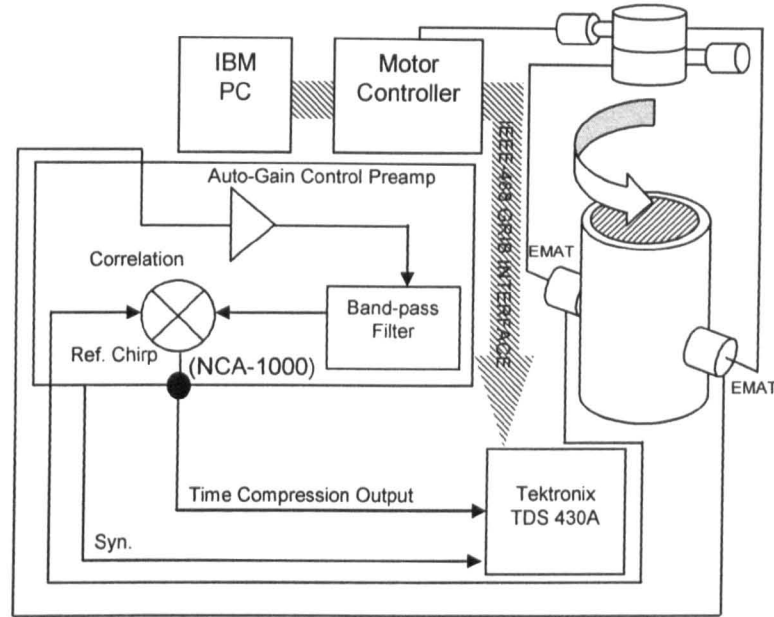


Figure 4.4: The experimental configuration used to obtain data for tomographic reconstruction.

4.4 Results and Discussion

Data was first collected using conventional pulsed excitation, using the apparatus of Figure 4.3, and a water-filled metallic beverage can, at 7° intervals over an angular range of $\pm 63^\circ$. The geometry used for experimental data collection is shown in Figure 4.5. Figure 4.6 shows an example of a received time signal (Figure 4.6(a)) and the corresponding frequency spectrum (Figure 4.6(b)) that was obtained at 0° . The first arrival at 18.5 μ s corresponded to the zero order s_0 symmetric Lamb wave (s_01), which travelled around the container wall, with a dominant frequency content centred at ~ 200 kHz and extending to around 800 kHz. A second echo of this (s_03) was seen at 59.8 μ s. Note that no higher order Lamb modes were observed. The smaller amplitude component that followed was the shear Horizontal (SH) wave, another guided wave mode

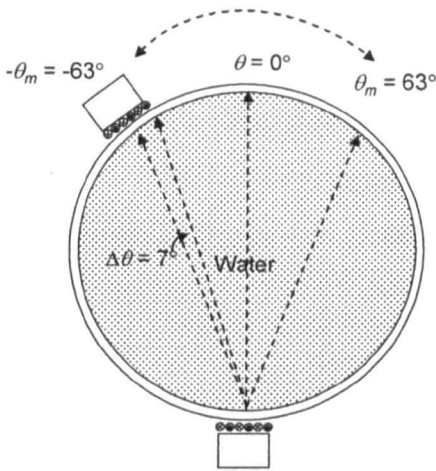


Figure 4.5: The experimental geometry used for data collection.

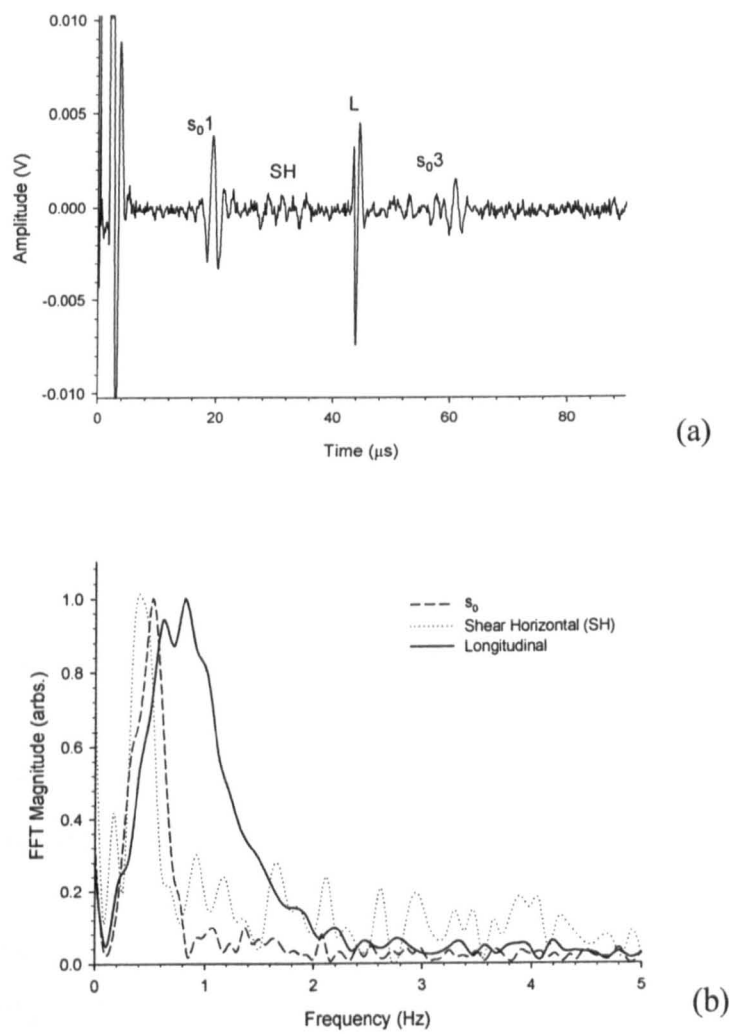


Figure 4.6: (a) A typical time signal that was generated and received across the beverage can filled with water, and (b) the corresponding frequency spectrum.

within the container wall, with a velocity of $\sim 3200 \text{ ms}^{-1}$. The larger amplitude component at $44 \text{ } \mu\text{s}$ was the longitudinal (L) wave transmitted directly across the water from source to receiver. Note that the longitudinal mode had a bandwidth ranging from $\sim 0.2 - 2 \text{ MHz}$. Waveforms were now collected at 7° intervals, the results being shown in Figure 4.7. Here 512 signal averages were used to reduce noise.

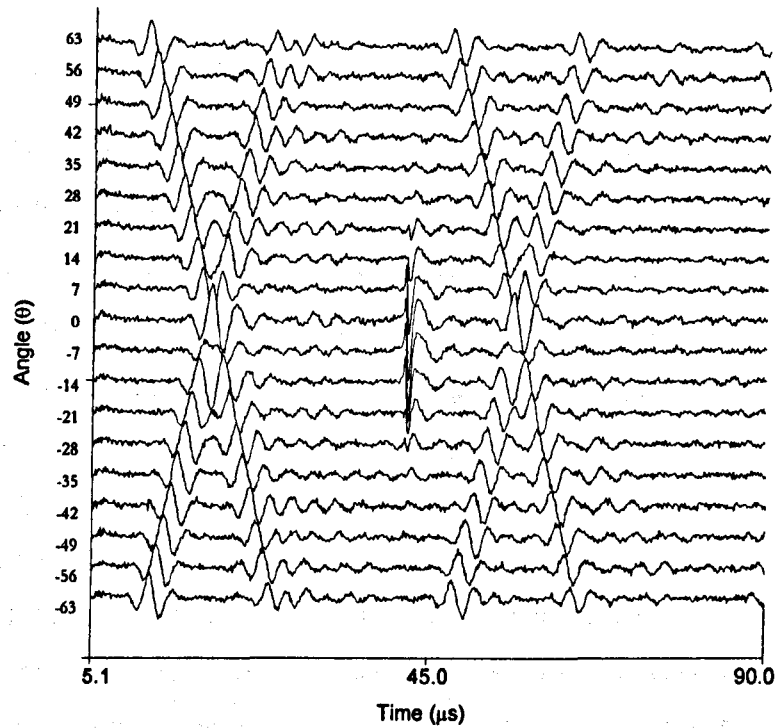


Figure 4.7: Experimental waveforms illustrating the arrival of multiple acoustic modes at various values of θ .

At $\theta = 0^\circ$, the s_0 guided mode from the source has travelled along equal path lengths around the circumference of the cylindrical container, leading to a constructive interference. However, at $\theta = 7^\circ$ and -7° , a destructive interference of s_0 signals occurred, because the waves travelling in counter-clockwise directions had slightly different path lengths. To understand this behaviour, theoretical dispersion curves were calculated. The phase and group velocity may be found using the Rayleigh-Lamb frequency relations [19].

For the symmetric (“s”) modes, these are:

$$\frac{\tan\left(\sqrt{1-a^2} \cdot d\right)}{\tan\left(\sqrt{b^2-a^2} \cdot d\right)} = \frac{4a^2 \left(\sqrt{1-a^2}\right)\left(\sqrt{b^2-a^2}\right)}{(2a^2-1)^2} \quad (4.1)$$

and for the asymmetric (“a”) modes:

$$\frac{\tan\left(\sqrt{1-a^2} \cdot d\right)}{\tan\left(\sqrt{b^2-a^2} \cdot d\right)} = \frac{(2a^2-1)^2}{4a^2 \left(\sqrt{1-a^2}\right)\left(\sqrt{b^2-a^2}\right)} \quad (4.2)$$

where $a = c_t/c_p$, $b = c_t/c_L$, and $d = 2\pi \times f \times t / c_t$, with c_t and c_L being the shear and longitudinal bulk wave velocities in the material, c_p is the phase velocity at frequency f , and t is the thickness of the plate. The group velocity is simply the differentiation of the phase-velocity curve with respect to frequency, so that $c_g = dw/dk$, where $w = 2\pi \cdot f$, and k is the wave number.

Figure 4.8(a) shows the phase velocity dispersion curves for Lamb waves propagating in an aluminium plate, and Figure 4.8(b) shows the corresponding group velocity curves. As can be seen, there are two possible modes below 10 MHz, which are the zero order s_0 and a_0 modes. Comparing the theoretical values with the calculated group velocities, it was confirmed that at this frequency-thickness combination only the s_0 mode is propagating along the tested cylindrical container sample and no higher modes are present. This single Lamb wave mode is located in a non-dispersive region. Calculations using the arrival time of the time compression peaks gave a wave velocity of $5600 \pm 250 \text{ ms}^{-1}$. As predicted, the propagation of the s_0 wave can lead to acoustic interference with the wanted (L) mode at θ around -70° , and 70° , and can mask the wanted (L) signal.

For these reasons, the pulse compression apparatus shown earlier in Figure 4.4 was used to deal with this problem. Using pulse compression, the waveform that resulted is shown in Figure 4.9 as the dotted line, where it should be noted that the signal was captured with no signal averaging. Each of the acoustic wave modes are represented as mono-polar peaks, as expected from cross-correlation processing as part of pulse compression. Calculations using the arrival time of the peaks gave s_0 , SH and L wave velocities of 5100 ± 250

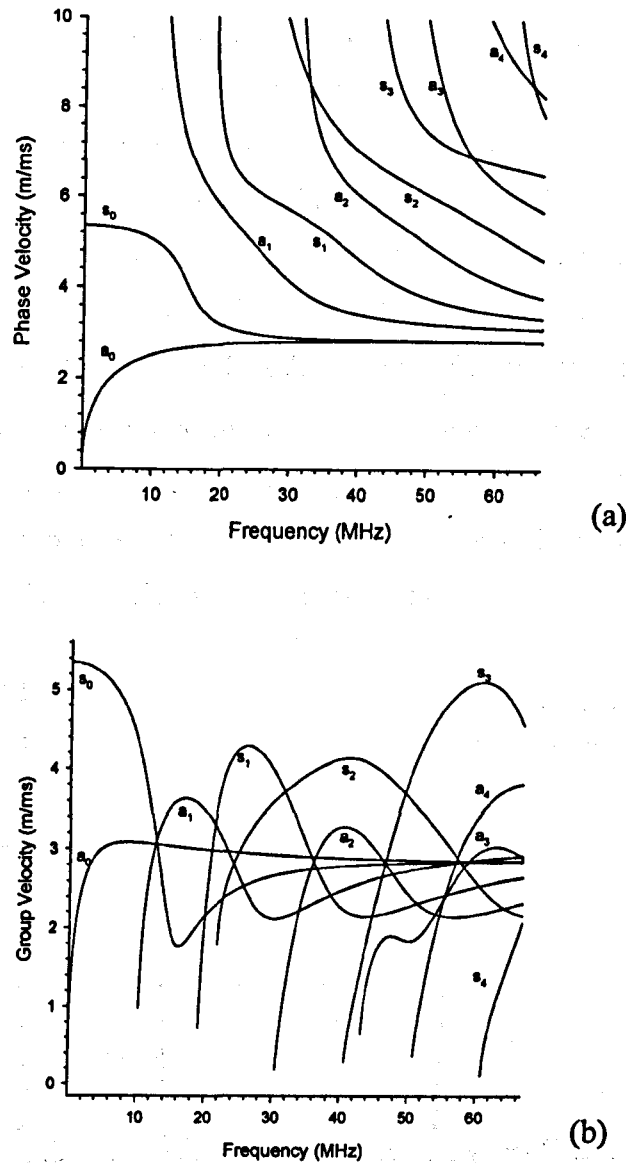


Figure 4.8: The velocity dispersion curves for Lamb waves propagating in an aluminium plate of thickness 0.15 mm, showing (a) phase velocity and (b) group velocity.

ms^{-1} , $3100 \pm 70 \text{ ms}^{-1}$ and $1485 \pm 5 \text{ ms}^{-1}$ respectively. As can be seen from the dotted-line, the signal obtained is similar to the waveform obtained in Figure 4.6(a). The number of modes present is a result of the large time-bandwidth product chosen for the experiment. It would be of great advantage, however, to be able to generate the L mode predominantly, without the s_0 mode making signal interpretation difficult. It was found that optimising the detection of a pure L mode from a complex acoustic signal was possible with an appropriate choice of time-bandwidth product. The waveform bandwidth and duration are

selectable within limits to provide a means of matching the coded waveform to eliminate any interference modes. This was obtained by shifting the dominant frequency employed in the chirp excitation to the signal bandwidth region of interest (*i.e.* the longitudinal mode). Note the spectral content of s_0 and L are different as shown in Figure 4.6b, and this is due to the finite aperture size of the EMATs. This feature allows the generation of L mode without the s_0 mode using pulse compression and EMATs. In the experiment, the duration of the chirp (T) was set to $50\text{ }\mu\text{s}$, with both the centre frequency and Bandwidth (B) being 1.5 MHz . The result is illustrated in Figure 4.9 as the solid line. Now the through-transmitted L1 mode was highly visible in the time domain, as was its multiple reflection (L3). This approach thus allowed individual arrivals or modes to be easily identified in a complex signal.

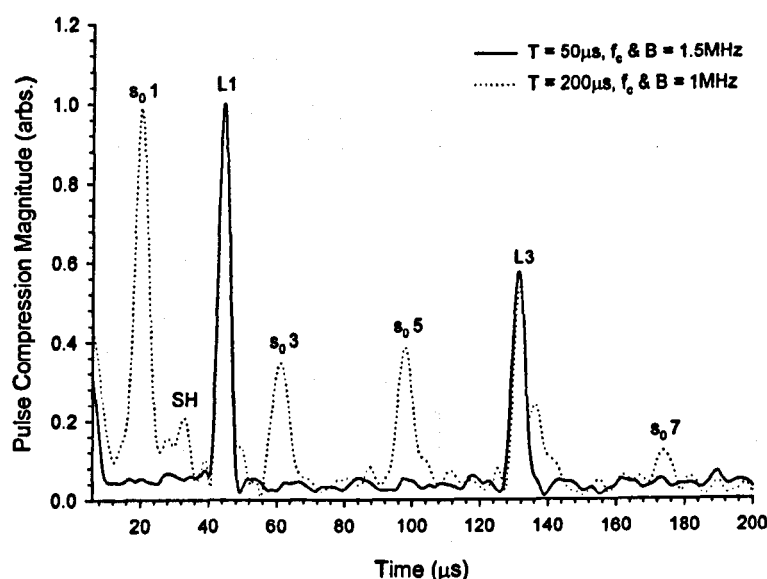


Figure 4.9: Waveforms obtained using the pulse compression approach. The dotted line is the waveform obtained following conventional pulse compression, and contains s_0 Lamb modes, Shear Horizontal (SH) waves and longitudinal (L) acoustic modes, with multiple arrivals of each denoted by additional numbers. The result of mode extraction of the longitudinal mode is shown as the solid line, where interference with other modes has been dramatically reduced.

The application of the pulse compression signal processing technique to EMATs was used to determine the location of a water-oil interface in the container. Experiments were performed to examine the passage of the radiated ultrasonic beam through a liquid layer using a pair of identical EMATs. The transducers were set up in a through-transmission configuration. The schematic

diagram of the experimental setup is shown in Figure 4.10. Both transducers were mounted to produce a beam perpendicular to the container surface. Pulse compression was used to improve the SNR of the measurement. Figure 4.11 shows the through-transmission pulse compression output obtained in water (solid line), oil (dotted line) and at the water-oil interface (dashed line).

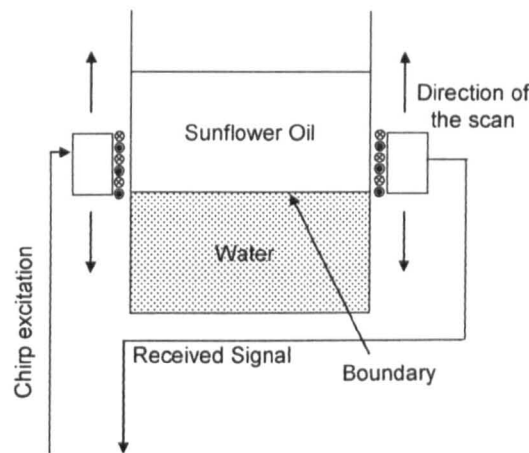


Figure 4.10: The schematic diagram of the experimental setup to determine the location of a water-oil interface in the container.

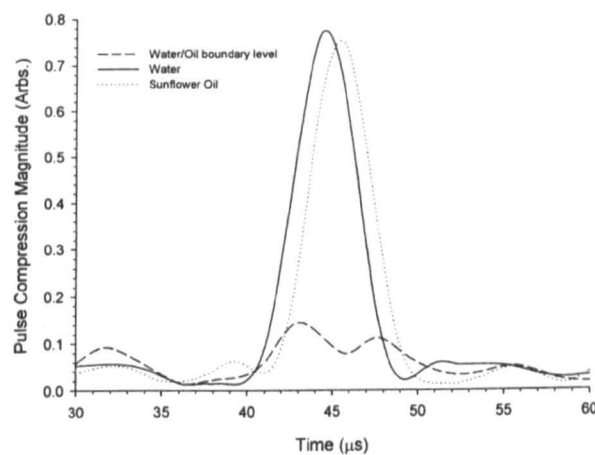


Figure 4.11: A single through-transmission signal obtained in water (solid line); oil (dotted line) and at a water-oil interface (dashed line).

The generation and detection of longitudinal wave across the container using EMATs does not require any coupling, this allowing a very high degree of accuracy for time arrival measurements (as no couplant is necessary from the transducers to the container wall). The calculations using these arrival times of the peaks gave a wave velocity of $1465 \pm 15 \text{ ms}^{-1}$ (water) and $1415 \pm 35 \text{ ms}^{-1}$

(sunflower oil) respectively. This agrees with published results for longitudinal velocity in water of 1480 ms^{-1} and sunflower oil 1450 ms^{-1} [20].

The EMATs were also scanned vertically down the container, and pulse compression outputs obtained at 1 mm intervals. At each location, the peak amplitude and the arrival time of the L mode waveform were recorded. A plot of the results is shown in Figure 4.12. Note the waveforms contained only the longitudinal mode. The first arrival (L1) corresponded to the through-transmitted longitudinal wave, and the subsequent smaller peak (L3) was the first multiple reflection. The liquid layer boundary is clearly visible, as the amplitude drops at the boundary, and the time of arrival of the signals changes at the same location. The predetermined position was compared to the actual location, giving an accuracy of $\pm 0.5 \text{ mm}$.

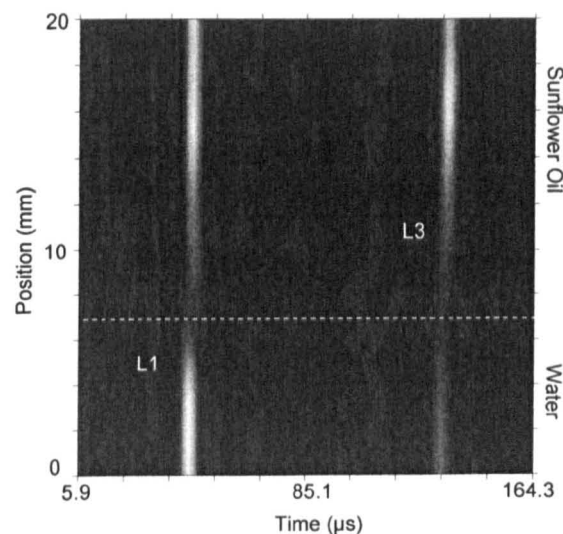


Figure 4.12: A grey-scale plot of the data obtained at various heights as the EMAT system was scanned vertically over the water/oil interface region.

A plot of the peak amplitude and arrival time, as a function of position (Figure 4.13(a)) indicates clearly the position of the boundary, although the latter gives a more accurate location. This is due to the received amplitude being dependant on the receiver aperture size. At the water-oil interface location, the attenuation is at maximum. Here, part of the radiated beam is transmitted via water and part transmitted via oil. Owing to the difference in acoustic properties through each of the two media, destructive interference results. To illustrate this, the frequency spectra obtained following measurements in water only (solid

line), oil only (dashed line), and at the interface between the two (dotted line) are shown in Figure 4.13(b).

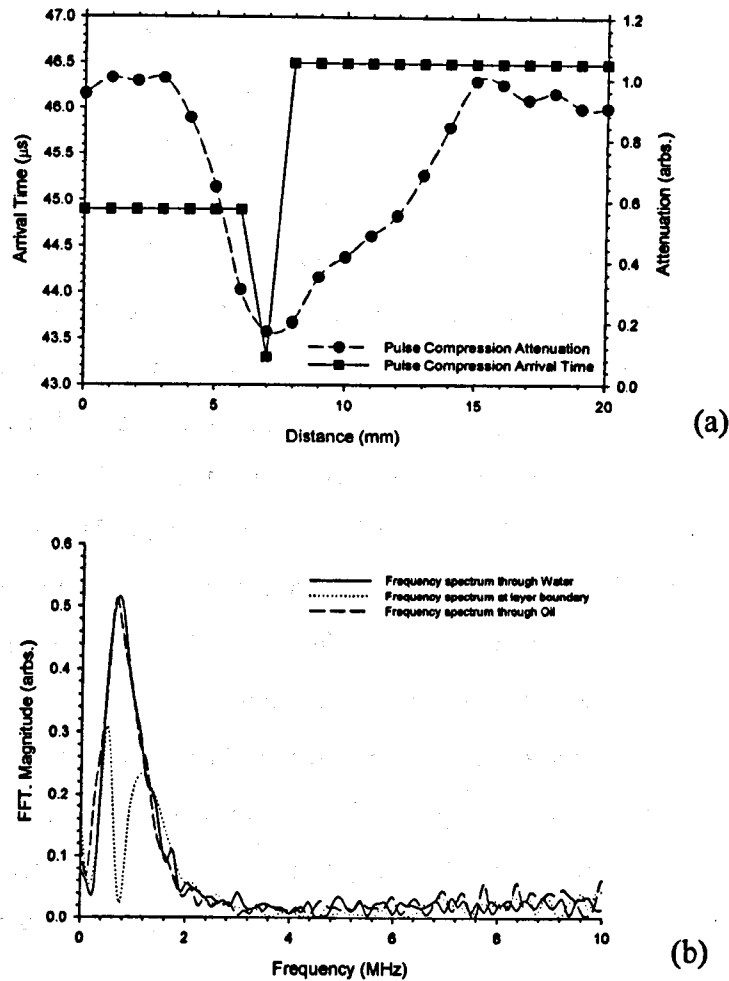


Figure 4.13: (a) The peak amplitude and the arrival time of the L mode as a function of vertical position; (b) Frequency spectra obtained in water (solid line), oil (dashed line), and at the interface (dotted line).

In isolation, the separate frequency response of oil and water are very similar, and similar to those obtained earlier in Figure 4.6 for the mode-extracted longitudinal mode. However, the spectrum obtained at the boundary between the immiscible mixture of oil and water clearly indicates that the water-oil interface is acting as a band-stop (notch) filter. This is most likely due to the fact that there is a phase mismatch between of the beams because of the difference in the speed of sound in each of these media and the consequent difference in the arrival time.

The apparatus shown earlier in Figure 4.4 was used to collect tomographic data using pulse compression and mode extraction. Each scan consisted of 41 receiver positions at 1 degree intervals opposite the source, and 72 source locations (5 degree intervals) covering in the complete range of the circular container. The output signals were of the form similar to that obtained as the solid line in Figure 4.9, namely as a distinct longitudinal peak without interference from other guided wave modes. The pulse compression data was processed in real time. The data was then input to the tomographic reconstruction software, and images obtained from the amplitude of the received longitudinal wave signal at each source and receiver position.

Figure 4.14(a) shows the attenuation image ($\text{dB}\cdot\text{mm}^{-1}$) of the cylindrical container filled with water with a 6.6mm diameter copper rod located at the coordinates (55, 35) mm. As no waveform could be readily identified travelling directly through the copper rod, the reconstructed attenuation within the solid is thought to be due to diffraction of the waves around its edge in water. The copper rod can be distinguished in this image. The experiment was repeated with two 7.2 mm diameter aluminium rods located separately at the coordinates (15, 33) mm and (48, 48) mm with 65 averages. The attenuation ($\text{dB}\cdot\text{mm}^{-1}$) of the reconstructed image is shown in Figure 4.14(b). Despite the slight distortion, the reconstruction still extracted an accurate position of the aluminium rod.

4.5 Conclusions

A pair of non-contact EMATs has been used in this study to generate and detect ultrasonic waves across beverage containers. A planar spiral EMAT prototype was designed and fabricated using PCB techniques. EMATs do not require any coupling, which allows a high degree of accuracy for time of arrival measurements. It was shown that ultrasonic wave propagation in a typical beverage container is complex due to geometrical considerations. Multiple acoustic modes (*e.g.* symmetrical Lamb modes (s_0), shear horizontal SH modes, and longitudinal (L) modes) were shown to be present when conventional transient pulse excitation was used, and the presence of s_0 and SH modes was

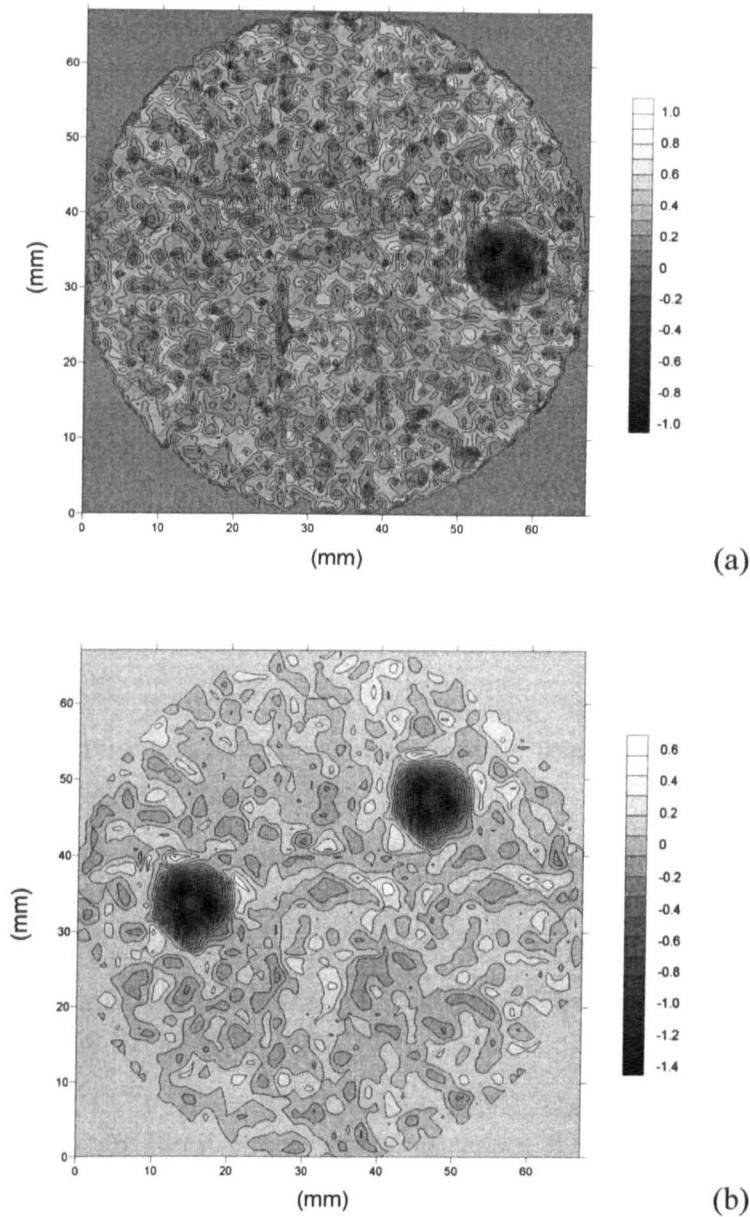


Figure 4.14: The reconstructed attenuation image ($\text{dB} \cdot \text{mm}^{-1}$) of the water-filled cylindrical container with (a) a 6.6 mm diameter copper rod located at the coordinates (55, 35) mm, and (b) two 7.2 mm diameter aluminium rods located separately at the coordinates (15, 33) mm; (48, 48) mm. Amplitude scales are arbitrary (1×10^{-4}).

seen to prevent the required through-transmitted longitudinal (L) wave from being identified at all locations. Pulse compression signal processing was thus employed for mode extraction while maintaining a high resolution and good signal to noise ratio. The application of the pulse compression signal processing technique to EMATs was also used to determine the location of water-oil interface in the container. The destructive interference at the boundary location was due to the mismatch of acoustic impedance between different media. The

resolution obtained via arrival time was better than that obtained using attenuation, thought to be due mainly to the finite aperture of the EMATs.

Fan-beam tomography was also employed for tomographic imaging of the size and location of solid objects in a cylindrical container. Here the use of mode extraction was seen to lead to clear images from the L mode, even though guided wave signals in the container wall were still present. This indicates that the combination of pulse compression and mode extraction, when applied to EMAT transducers for the testing of fluid-filled containers, gives a distinct advantage over other forms of testing such objects.

4.6 References

- [1] K. S. Ho, D. R. Billson and D. A. Hutchins, "Inspection of drinks cans using non-contact electromagnetic acoustic transducers," *J. Food Eng.*, vol. 80, pp. 431-44, 05. 2007.
- [2] B. Zhao, O. A. Basir and G. S. Mittal, "A self-aligning ultrasound sensor for detecting foreign bodies in glass containers," *Ultrasonics*, vol. 41, pp. 217-22, 05. 2003.
- [3] M. Edwards and I. Ebrary, *Detecting Foreign Bodies in Food*. Cambridge : Woodhead Pub, 2004.,
- [4] S. I. Cho, G. W. Krutz, H. G. Gibson and K. Haghighi, "Magnet console design of an NMR-based sensor to detect ripeness of fruit," *Trans. ASAE*, vol. 33, pp. 1043-1050, 1990.
- [5] P. Butz, C. Merkel, R. Lindauer and B. Tauscher, "Application of a multi-wavelength near infrared diode laser array for non-destructive food analysis," in *Near Infrared Spectroscopy: Proceedings of the 10th International Conference*, 2002, pp. 519-524.
- [6] V. Bellon, J. L. Vigneau and M. Leclercq, "Feasibility and Performances of a New, Multiplexed, Fast and Low-Cost Fiber-Optic NIR Spectrometer for the On-Line Measurement of Sugar in Fruits," *Appl. Spectrosc.*, vol. 47, pp. 1079-1083(5), 1 July 1993.
- [7] B. Park, K. C. Lawrence, W. R. Windham and R. J. Buhr, "Hyperspectral Imaging for Detecting Fecal and Ingesta Contaminants on Poultry Carcasses," *Trans. Am. Soc. Agric. Eng.*, vol. 45, pp. 2017-2026, 2002.

- [8] K. Chao, P. M. Mehl and Y. Chen, "Use of hyper- and multi-spectral imaging for detection of chicken skin tumors," *Appl. Eng. Agric.*, vol. 18, pp. 113-119, 2002.
- [9] M. P. Snell, "Gamma-Ray Technology: The Practical Container Inspection Alternative," *Port Technology International*, vol. 9, pp. 83-88, 2004.
- [10] M. J. W. Povey and T. J. Mason, *Ultrasound in Food Processing*. London : Blackie Academic & Professional, 1998.
- [11] E. Haeggstrom and M. Luukkala, "Ultrasound detection and identification of foreign bodies in food products," *Food Control*, vol. 12, pp. 37-45(9), January 2001.
- [12] T. H. Gan, D. A. Hutchins and D. R. Billson, "Preliminary studies of a novel air-coupled ultrasonic inspection system for food containers," *J. Food Eng.*, vol. 53, pp. 315-323, 2002.
- [13] M. C. Bhardwaj, *Non-Contact Ultrasound: The Last Frontier in Non-Destructive Testing and Evaluation*. John Wiley & Sons, 2001.
- [14] A. Kulmyrzaev, C. Cancelliere and D. J. McClements, "Characterization of aerated foods using ultrasonic reflectance spectroscopy," *J. Food Eng.*, vol. 46, pp. 235-241, 2000.
- [15] S. Dixon, C. Edwards and S. B. Palmer, "Non-contact ultrasonic liquid level measurement of drinks cans," *Proc SPIE Int Soc Opt Eng*, vol. 3589, pp. 52-57, 1999.
- [16] R. S. Edwards, A. Sophian, S. Dixon, G. -. Tian and X. Jian, "Dual EMAT and PEC non-contact probe: Applications to defect testing," *NDT and E Int.*, vol. 39, pp. 45-52, 2006.
- [17] A. C. Kak and M. Slaney, *Principles of Computerized Tomographic Imaging*. Philadelphia : Society for Industrial and Applied Mathematics, 2001.
- [18] L. A. Shepp and B. F. Logan Jr, "Fourier reconstruction of a head section," *IEEE Trans. Nucl. Sci.*, vol. NS-21, pp. 21-43, 1974.
- [19] I. A. Viktorov, *Rayleigh and Lamb Waves*. New York : Plenum Press, 1967.
- [20] J. Lubbers and R. Graaff, "Simple and accurate formula for the sound velocity in water," *Ultrasound in Medicine and Biology*, vol. 24, pp. 1065-1068, 1998.

Chapter 5

Lamb Wave Tomography and Wavelet Processing

5.1 Introduction and Background

This chapter uses spiral coil EMATs to generate and receive Lamb waves in plates. The generation and reception of such waves using EMATs over a wide bandwidth is usually complicated, due to the fact that EMATs produce low SNR signals, and the fact that Lamb waves are dispersive. In this chapter, a Wavelet Transform has been used to identify particular Lamb wave modes within a complicated wide bandwidth signal generated and detected by EMATs. It is demonstrated that tomographic Lamb wave images can be produced using the modes identified in this way. The work is the subject of a journal paper [1].

Lamb waves are used increasingly for certain non-destructive evaluation (NDE) problems, as they can propagate over long distances in plate-like structures. The properties of both Rayleigh and Lamb waves for NDE and monitoring applications are well documented [2]. For example, Lamb waves have been used to carry out rapid inspection of various structures [3], including boilers and heat exchanger piping [4]. They can also be used to determine the elastic properties of materials [5], and to measure the anisotropic properties of cold-rolled metals [6], an application investigated in more detail in Chapter 7. Other work has shown that they can be used for liquid level measurement in sealed metal tanks [7] and for corrosion thickness gauging in plates [8]. Lamb wave tomography and pipe corrosion monitoring have also been demonstrated [9]. There have also been developments in the area of non-contact Lamb wave ultrasonic excitation and detection, such as the use of laser techniques and air-coupled ultrasound [10, 11]. The technique could have application in the metal forming industry, where rapid imaging of sheet material using a fixed cylindrical EMAT array against a flat surface could highlight areas of defects at early points in the production process.

Lamb wave offers a powerful non-destructive technique for the health assessment of large structures as their propagation properties depend on the thickness and the mechanical properties of the material. For example, low cost and small piezoelectric transducers have been used for aircraft wing inspection [12]. An air-coupled ultrasonic method for the inspection of railroad tracks has been demonstrated in [13]. Air-coupled ultrasonic testing can benefit from non-contact probing and ease of transducer positioning. Structural health monitoring of composite structures using Lamb wave tomography has been illustrated by Prasad *et al.* [14], and Lamb wave diffraction tomography has been conducted by Wang *et al.* [15] for reconstructing images of structural damage, providing quantitative information on structural health.

It is well known that Lamb wave testing is complicated by the dispersive nature of Lamb waves. This is illustrated in Figure 5.1(a), which shows the phase velocity dispersion curves for Lamb waves propagating in a 1 mm thick aluminium plate. Figure 5.1(b) shows that the corresponding group velocity (the velocity at which energy propagates along the plate) also exhibits dispersion (*i.e.* is a function of the frequency-thickness product). Thus, if a broad bandwidth source is used, the different frequency components of the wave will travel at different speeds, and more than one mode can exist at any given frequency. At low frequency-thickness products, only two modes, a_0 and s_0 , can propagate. As the frequency-thickness increases, more modes are possible and the interpretation of signals tends to become more complicated.

An accurate determination of the particular mode of interest is essential as each mode has different through-thickness displacement values, and they are sensitive to different types of flaws. These characteristics make received signals difficult to interpret directly, and prevent Lamb waves from being applied easily in many NDE applications for plate-like structures. One approach to simplifying the interpretation of received signals is to excite a single Lamb mode. This can be achieved by reducing the bandwidth of the signal by employing tone-burst excitation. However, this method must be used with care as additional modes are easily excited if the tone-burst is too short [16]. Increasing the number of cycles in the tone-burst reduces the bandwidth, which can also help to improve the signal to noise ratio. However, the resultant increase in the duration of the propagating signal makes it more difficult to resolve multiple reflections.

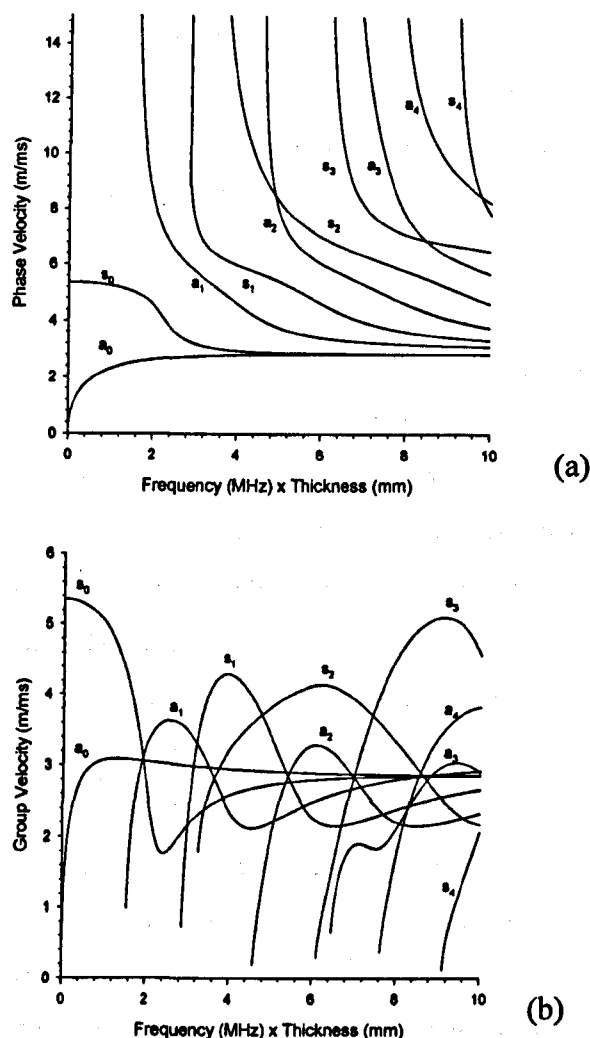


Figure 5.1: (a) Phase velocity and (b) group velocity dispersion curves for the first five Lamb wave modes in a 1 mm thick aluminium plate.

Another way to improve the wave localisation process is by considering only certain frequency components using a time-frequency analysis. For instance, the pseudo-Wigner-Ville distribution has been used to measure the group velocities of Lamb wave in a graphite/epoxy plate [17], and a time-frequency analysis based on the short time Fourier Transform (STFT) has been used to obtain the propagation times of scattered ultrasonic signals in many structural materials [18-20]. An efficient method for mode identification is the two-dimensional Fourier Transform (2D-FFT), which is employed to assist the interpretation of the complicated signals which are produced by mode conversion and dispersion [21]. This, however, requires multiple transducer

locations. More recent work has used a discrete-wavelet fingerprint technique (DWFP) for noise reduction and enveloping of Lamb wave signals generated by contact piezoelectric transducers [22]. Here the source was excited with a high power tone-burst signal, and a polynomial fit was employed to perform mode identification on the experimental data. The processed data was then used for cross-hole tomographic imaging.

In the work to be described in this Chapter, a Wavelet Transform has been used to identify particular Lamb wave modes, and quantitative information concerning each mode extracted from the experimental data. Note that guided waves have been used in many practical measurements where such a technique would have value [23, 24], and wavelet transforms have shown use in studying reflections of guided waves [25]. The particular measurement to be described here used a pair of EMATs over a wide bandwidth, to generate and detect Lamb waves in aluminium plates. It was demonstrated that tomographic Lamb wave images could be achieved using a single Lamb wave mode, even when both multiple propagation modes and reflections from the end of the sample were present. Thus, by combining time-frequency analysis with a broadband excitation source, different images could be obtained using different modes, without the need for repeat scans.

There are various wavelet approaches that could be used to treat ultrasonic Lamb wave data from EMATs. What is required is the efficient identification and isolation of the various propagating modes in a plate, and the subsequent reconstruction of tomographic images from the data supplied by wavelet processing. As mentioned from the beginning, two approaches are described in this chapter. The main one is the use of a continuous wavelet transform using a Gaussian or “Mexican Hat” wavelet, followed by a Hilbert Transform. This method leads to good results, and has been included in a journal paper that has been accepted for publication [1]. This approach forms the main part of this Chapter, with examples of mode extraction and tomographic Lamb wave images being shown in a later Section. It will be demonstrated that mode isolation can be achieved efficiently, and that both amplitude and arrival time data can be extracted for input to imaging algorithms of the type. In addition, an alternative wavelet, the Morlet wavelet, will also be investigated for mode identification, and the results for mode extraction are then

compared to the Mexican Hat approach. As will be seen, similar time-frequency plots result, indicating that both can give the required information.

5.2 The Continuous Wavelet Transform

Amongst the various techniques for time-frequency analysis, a Wavelet Transform (WT) is, in principle, particularly suitable for locating the high frequency components of Lamb waves [26]. For example, the Short Term Fourier Transform (STFT) may not give good resolution at high frequencies because of the use of a fixed window function. A number of studies have been conducted on the application of the WT in damage detection [27-29], where it has been shown that the time-frequency WT can improve the wave localisation process. Unlike the Fourier Transform, which uses sinusoidal functions as its basis, the WT uses more general basis functions, $\psi_{a,b}(t)$, known as daughter wavelets. The continuous wavelet transform of a particular function of time $f(t)$ is defined as:

$$Wf_{a,b} = \int_{-\infty}^{\infty} f(t)\psi_{a,b}(t)dt \quad (5.1)$$

where $Wf_{a,b}$ is the wavelet coefficient. Each daughter wavelet is derived from a prescribed function, called the mother wavelet $\psi(t)$, through scaling and shifting. Mathematically, this can be written as:

$$\psi_{a,b}(t) = \frac{1}{\sqrt{a}}\psi\left(\frac{t-b}{a}\right) \quad (5.2)$$

in which a and b are real positive continuous variables controlling the degrees of scaling and shifting, respectively. The value of b represents the shift of the wavelet in time, whereas the value of a represents a change in time scale, where $a > 0$.

As described above, the Gaussian or “Mexican Hat” function (Figure 5.2) will be studied initially as the mother wavelet and is proportional to the second derivative function of the Gaussian probability density function.

This function can be expressed as:

$$\psi(t) = \left(\frac{2}{\sqrt{3}} \pi^{\frac{1}{4}} \right) (1-t^3) \exp \frac{-t^2}{2} \quad (5.3)$$

and is useful for extracting a particular harmonic component of dispersive waves.

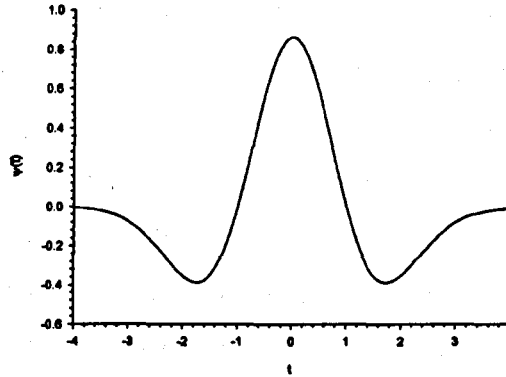


Figure 5.2: Mexican Hat or Gaussian wavelet function.

The peak of the magnitude plot of $Wf_{a,b}$ signifies the presence of a wave group whose frequency and arrival time are indicated by the corresponding scaling and shifting parameters, *i.e.*, a and b , respectively. The expression for the continuous wavelet transform (CWT) in discrete form, is now:

$$Wf_{a,b} = \frac{1}{\sqrt{a}} \sum_n f(n) \int_n^{n+1} \psi \left(\frac{t-b}{a} \right) dt \quad (5.4)$$

where $f(n)$ is a discrete time-signal which is obtained by sampling $f(t)$ at a sampling rate f_s . The centre frequency, f_c of the wavelet $\psi_{a,b}(t)$ is then related to the sampling period t_s , and when the wavelet is dilated by a factor a , this centre frequency becomes f_c/a . The discrete signal $f(n)$ then has the values at discrete-time points $n = t \times f_s$ for integer values of n . At any values of a and b , the wavelet coefficients $Wf_{a,b}$ are obtained by convolving $f(n)$ with a dilated and translated version of the mother wavelet, as described by Equation (5.4).

5.3 Simulations

The operation of the CWT can be illustrated using a simple simulated waveform such as that shown in Figure 5.3(a). The first arrival is a 10 μs long signal at a certain frequency f_1 , followed after a time delay of 55 μs by a second, higher frequency component f_2 of the same duration. The centre frequencies (f_c) of the f_1 and f_2 arrivals were set to 1.7 MHz and 4 MHz, respectively. The corresponding frequency spectrum, obtained via an FFT, is shown in Figure 5.3(b). Figure 5.3(c) shows the result of a CWT analysis of the simulated signal. As expected, the signal components are well localised in both time and frequency, demonstrating that the approach has merit for signal identification. However, the oscillatory nature of the signals makes identification difficult for the signal at frequency f_2 . For these reasons, it is more convenient to plot the envelope of these functions using a Hilbert transform of the CWT output. Such a technique has been used previously for envelope detection in vibration studies [30, 31], meteorological [32] and speech data [33].

Defining the real and imaginary parts of the complex CWT as $Wf_{a,b}(t)$ and $iWf_{a,b}I(t)$ respectively, so that:

$$|Wf_{a,b}(t)| = \sqrt{Wf_{a,b}(t)^2 + iWf_{a,b}I(t)^2} \quad (5.5)$$

where $Wf_{a,b}(t)$ is the wavelet coefficient obtained in Equation (5.4), and $Wf_{a,b}I(t)$ is associated to $Wf_{a,b}(t)$ obtained by the Hilbert Transform:

$$Wf_{a,b}I(t) = Wf_{a,b}(t) * h(t) \quad (5.6)$$

where $*$ is the convolution product and $h(t) = 1/(\pi t)$. Hence, substituting Equation (5.6) into Equation (5.5) can produced the smoothed CWT output of $Wf_{a,b}$.

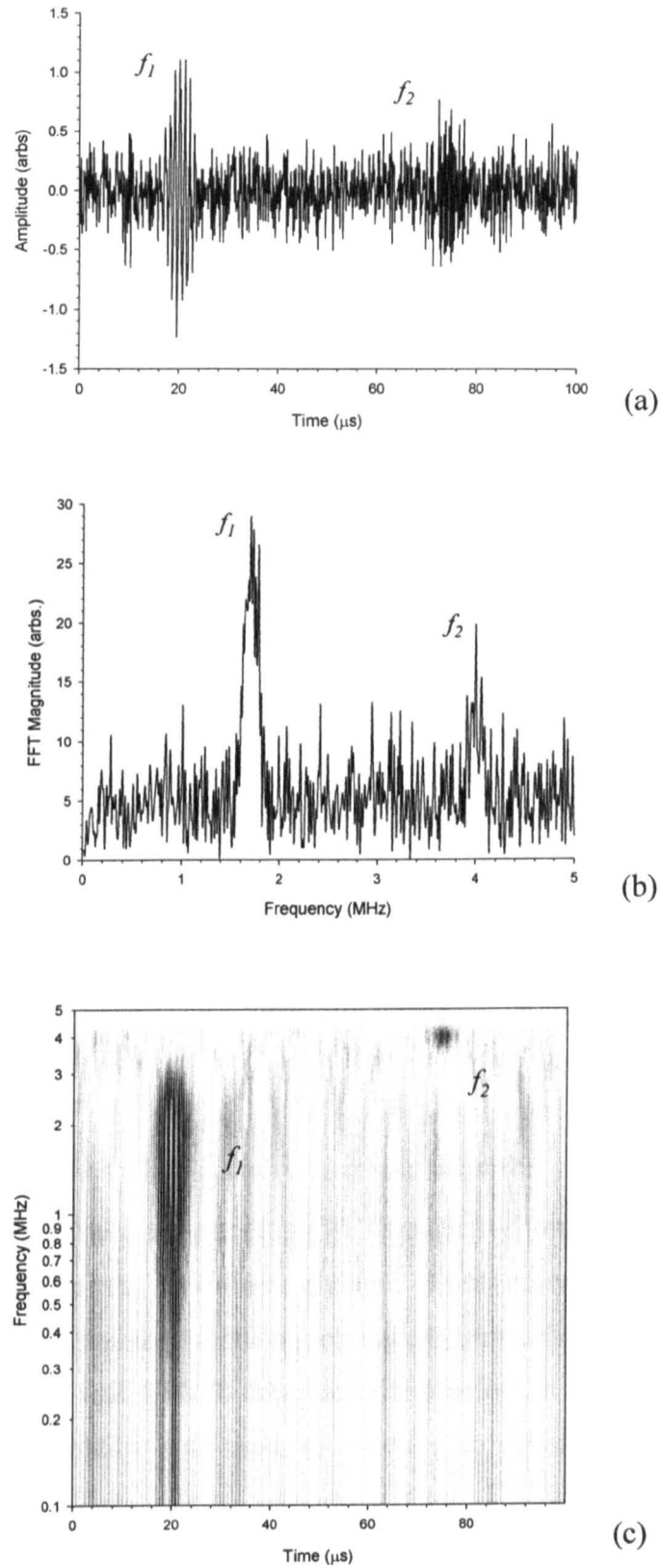


Figure 5.3: (a) Simple simulated signal containing two discrete frequencies (f_1 and f_2) travelling at different speed, with added random noise. (b) The corresponding frequency spectrum. (c) Continuous Wavelet Transform (CWT) of (a).

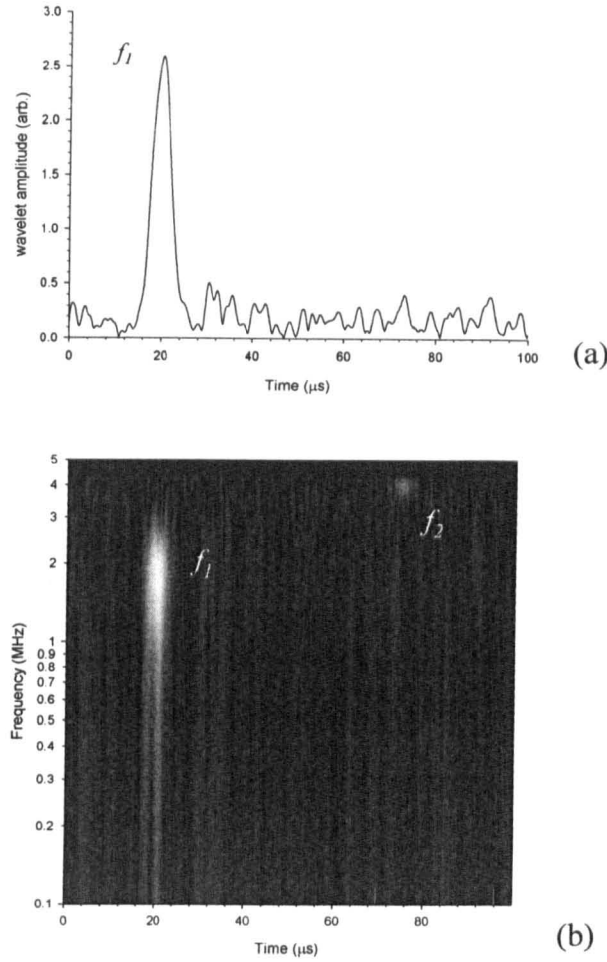


Figure 5.4: The effect of smoothing. (a) f_1 component extraction, and (b) CWT magnitude of the waveform shown earlier in Figure 5.3(a).

The smoothed CWT output which results for the f_1 component is shown in Figure 5.4(a). The corresponding CWT image is shown in Figure 5.4(b) for both components of the waveform, giving a clearer representation of the wave modes than was possible without smoothing (shown earlier in Figure 5.3(c)). In the processing of real EMAT data, described below, a filtering technique of variable width window was used, to produce an efficient method for time-frequency representation of the waveform. $|Wf_{a,b}|$ could then be plotted and used to determine whether a particular wave mode was present at that location on the time-frequency plot.

Ultrasonic Rayleigh and Lamb waves have been used in past work to reconstruct images in metal plates using water immersion techniques [34],

whereas other workers have used contact [35] and EMAT-based techniques [37]. This Chapter investigates the use of Lamb wave mode extraction using wavelets, so that tomographic images can be easily formed from waveforms where such modes overlap in time. Although various types of algorithm can be used to reconstruct tomographic images [38], the filtered back-projection algorithm [39], was used here, as it is efficient and easy to use. The tomography process can be explained by considering the sampling geometry shown schematically in Figure 5.5, in which data is collected by scanning transducer pairs at a fixed distance apart to form a projection p at an angle θ . Note that a variable has to be extracted for each particular mode using the CWT to produce an image, an example being time of arrival variations (leading to an image displaying changes in velocity). However, the image reconstruction technique can be used for any acoustic variable (*e.g.* attenuation or frequency shift). The CWT is the means by which the properties of each mode can be identified, from each individual path across the object.

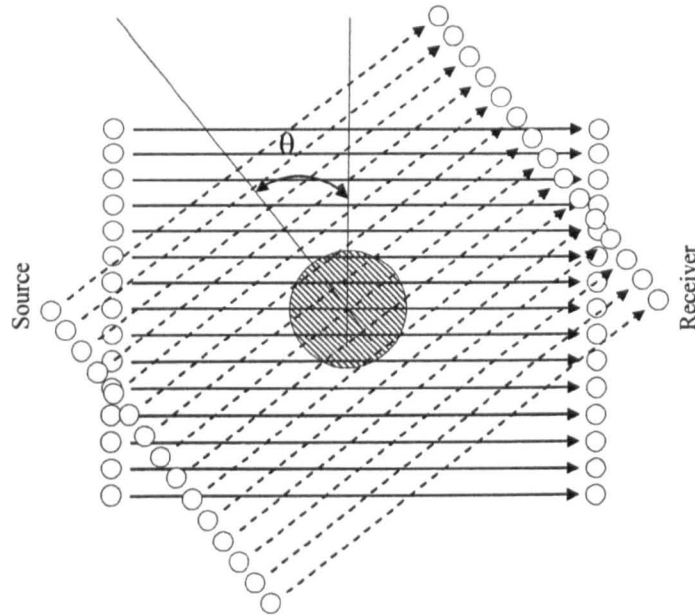


Figure 5.5: Sampling geometry used for tomographic reconstruction.

5.4 Experimental Setup

A spiral coil EMAT of 10 mm diameter was used in these experiments, and is shown schematically in Figure 5.6(a). The EMAT was constructed using

15 turns of 134AWP enamelled copper wire (0.22 mm diameter). The EMAT coil was placed against the flat face of a circular disc-shaped magnet to provide a magnetic field primarily in the direction normal to the sample surface. A neodymium-iron-boron sintered magnet was used, with a maximum flux density (B_r) of ~ 1.5 T. The experimental configuration is shown schematically in Figure 5.6(b), and used two similar EMATs. The source was driven with a 1 kV high voltage unipolar pulse of duration ~ 0.2 μ s from an AVTECH AVRH-1-C pulse generator. Lamb waves generated by the EMAT travelled along the plate to the receiver, which used a high impedance, high gain preamp (62 dB) fitted with a double-shielded cable to minimise electromagnetic noise pick-up. A second-order Butterworth high-pass filter was used to remove some of the random noise. The time waveform was the recorded on an Agilent 54622D digital oscilloscope. The two EMATs were separated by 50 mm (from centre to centre) in the work reported here.

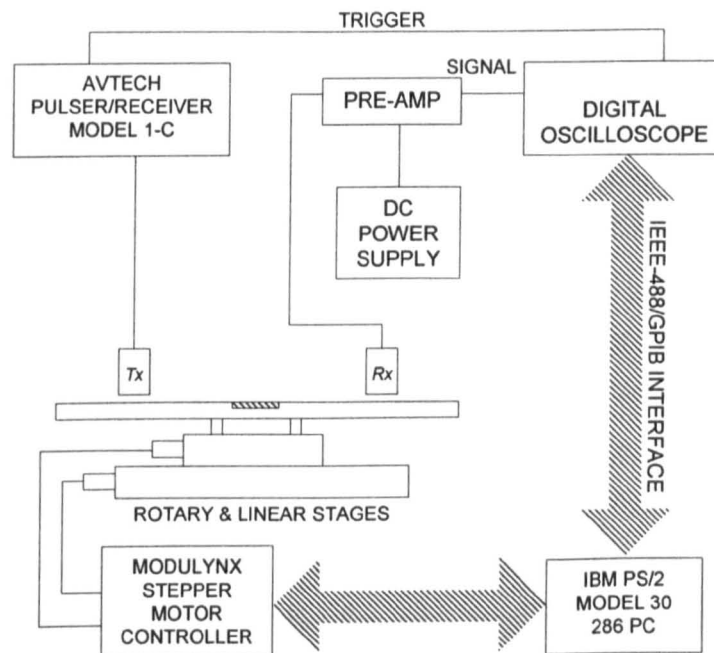


Figure 5.6: The experimental configuration for Lamb wave measurements.

Tomographic Lamb wave images were created by scanning the pair of EMATs, at a fixed 50 mm separation, across the surface of 0.69 mm thick aluminium plates containing known defects. The transducers were mounted on an X-Y translation stage driven by stepping motors, the exact position being

controlled by the computer via the motor drives. The data for tomographic images was obtained by scanning the transducer pair at some particular angle θ (see Figure 5.5) to form a projection, each of which consisted of 75 parallel measurements at 1mm intervals. The transducer pair was then rotated by an incremental angle $\Delta\theta$ of 12° , and the process repeated.

5.5 Results Using the Mexican Hat Wavelet

An example of the experimental EMAT data for a 1 mm thick aluminium plate is shown in Figure 5.7, including (a) the time signal, (b) the corresponding frequency spectrum, and (c) the result of the CWT where the magnitude (Equation (5.5)) of the coefficient is plotted as changes in grey-scale. Also plotted in Figure 5.7(c) are the expected group velocity curves for each mode. The large signal at the start of the time waveform in Figure 5.7(a) is electromagnetic pickup from the drive circuit, and this is followed by acoustic signals in the form of overlapping Lamb modes, which are difficult to identify. The large signal due to pickup was removed by windowing the original time signal (Figure 5.7(a)) from 7 μs to 100 μs to remove break-through noise. The frequency spectrum of Figure 5.7(b) shows that certain frequency bands are present, corresponding to certain modes of propagation. Thus, the first small peak is probably due to one or both of the two zero-order Lamb modes, but these are not identifiable separately. The next three modes are probably the a_1 , s_1 and s_2 from their cut-off values, although this again is not a certain prediction.

Processing with the CWT gives more information. Inspection of Figure 5.7(c) shows that both the a_0 and s_0 modes were present, primarily at frequencies below 1 MHz. Note that the large amplitude of the a_1 component makes analysis of other modes difficult (*e.g.* due to the large amplitude difference between the a_1 and s_2 modes). Hence, in Figure 5.7(c) and throughout such processing, the ultrasonic data was compressed by raising all values to the 1/4 power (*i.e.* the value of $|Wf(a,b)|$ was normalised within the plot, and then to discard contours within values lower than a 25% of the maximum in order to reduce clutter). This additional process improved the visibility of the lower amplitude modes, so that they were visible in the same time-frequency plot.

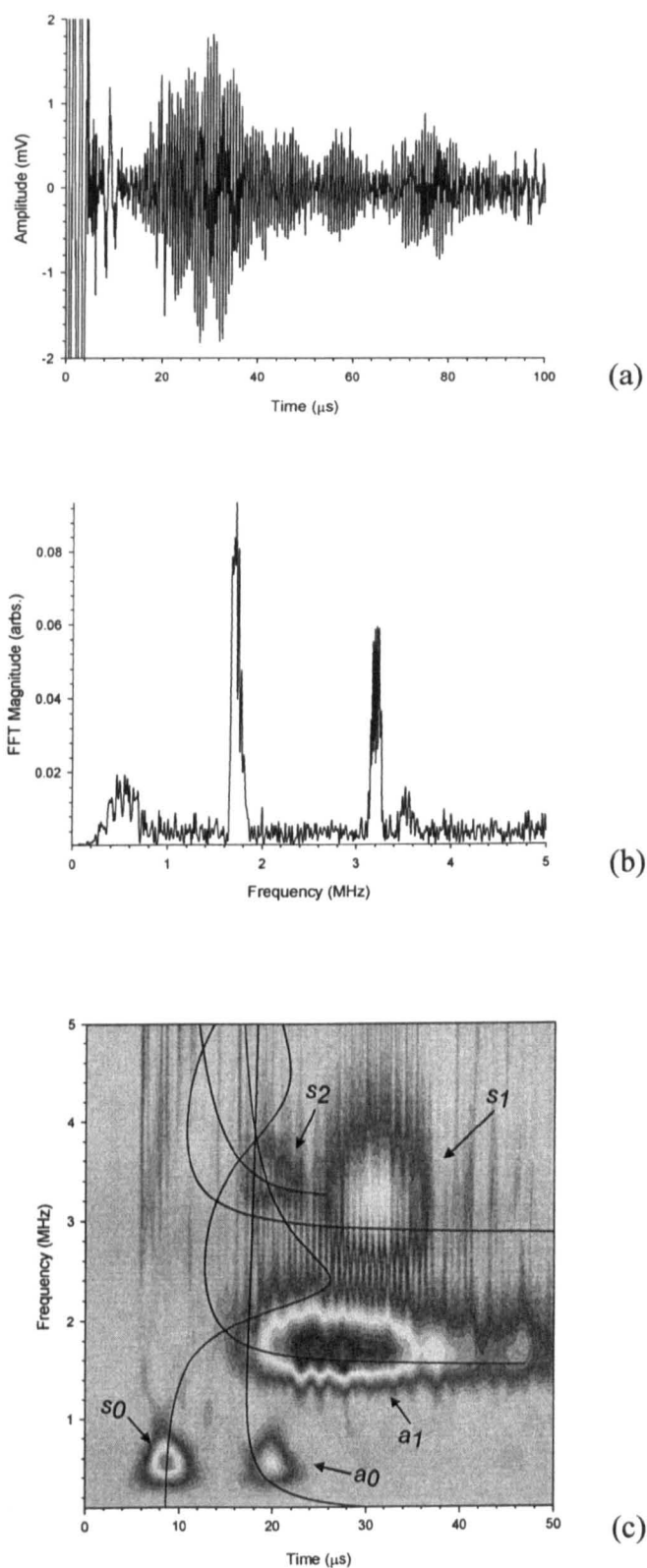


Figure 5.7: Experimental EMAT results for a 1 mm thick aluminium plate, showing (a) the received time waveform, (b) the corresponding frequency spectrum, and (c) CWT magnitude of the time waveform in (a).

Figure 5.7(c) demonstrates that the first mode to reach the receiver in the experimental waveform at the top of the figure is the s_0 mode. This is followed by the a_0 , s_1 and s_2 modes and later by the s_2 mode. The experimental data is consistent with theoretical predictions in that the data derived from the CWT lies on the theoretical dispersion curves. It is interesting to note that the EMAT source has succeeded in generating these modes with good signal amplitudes, with the a_1 mode having the largest amplitude and the s_2 being the least visible. This is thought to be a feature of the geometry of the spiral EMAT coil.

Because the modes are separated (*i.e.* are well-localised) on the time-frequency plot, a more accurate measurement of the group velocity of selected Lamb modes could be determined from the CWT output, at a particular frequency, by analysing the data at different propagation distances. An example is shown in Figure 5.8 for the s_1 Lamb mode in a 0.69 mm thick aluminium plate, at a frequency of 4.4 MHz. Here, ten measurements were taken at 5 mm increments in propagation distance, over a range of 50 mm to 95 mm, by scanning the EMAT receiver away from a fixed source location. A least-squares fit of arrival time versus distance was then used to calculate the propagation velocity at the chosen frequency of 4.4 MHz, which for the s_1 mode was found to be $2100 \pm 450 \text{ ms}^{-1}$.

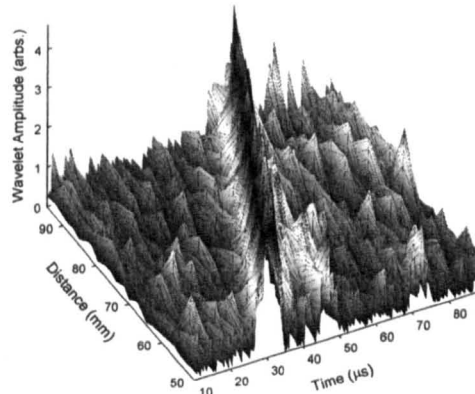


Figure 5.8: Measured s_1 mode group velocities on a 0.69 mm thick aluminium plate.

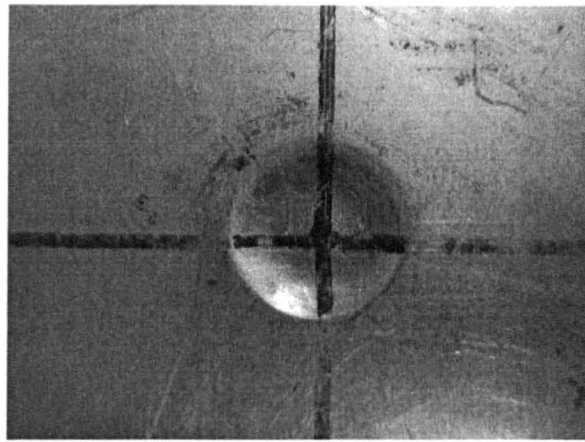
5.6 Lamb Wave Tomographic Imaging

As was illustrated in Figure 5.7, the CWT technique can assist in mode identification within EMAT Lamb waveforms over a wide bandwidth range.

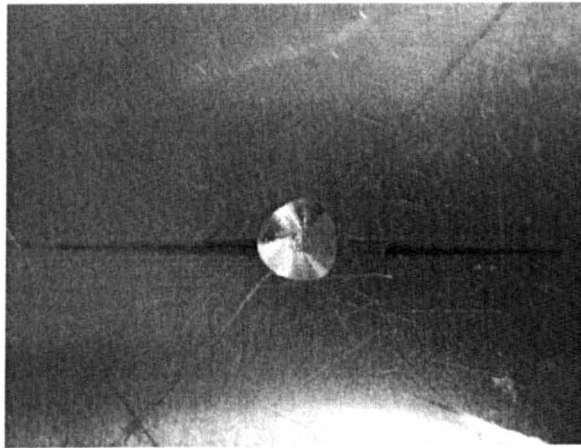
Each of these modes can be used to produce images of defects in plates. Thus, data for s_0 , a_1 and s_1 waveforms were obtained at particular frequencies in terms of peak amplitude, arrival time and centre frequency from the time-frequency plots. This data was then used as input to the tomographic reconstruction process for a given mode of propagation. A form of difference tomography was employed, in which all measurements were made with respect to the first ray path in each projection, which passed across defect-free material. The reconstructed image would then correspond to changes in a chosen parameter caused by the presence of a defect.

Three samples were imaged, each with a different artificial defect that was machined into the samples. Photographs of these three defects are presented in Figure 5.9. Consider first the 11 mm circular defect in the 0.69 mm thick aluminium plate. Images of attenuation in $\text{dB}\cdot\text{mm}^{-1}$ were produced using variations in peak amplitude of the s_0 , a_1 and s_1 modes, and the results are plotted in Figure 5.10. As can be seen, the a_1 mode (Figure 5.10(b)) seemed to give the better image in terms of dynamic range and resolution. The a_1 mode data was thus also used to produce images from both time of flight and peak frequency shift, with the results being presented in Figures 5.11(a) and (b) respectively.

Comparison to Figure 5.10 shows that, while the defect is visible in the centre of the images, the dynamic range is not as good as that obtained from amplitude data. Note the defect size indicated from attenuation data for the a_1 mode (Figure 5.10(b)) is larger than that of the original hole; this is due to diffraction and aperture effects. This is demonstrated further by a maximum of attenuation (darker region) at the centre of the image, surrounded by a lighter shade region of lower attenuation (*i.e.* higher amplitude), an effect of diffraction. The slowness image of Figure 5.11(a), obtained from time of flight data, indicates a more correct size for the defect, but contains more noise and reconstruction artefacts. This was also noted with the other defects of Figure 5.9(b) and 5.9(c), images of which using amplitude data are shown for the a_1 mode only in Figure 5.12. The different sizes of the two circular depressions in each of the plates (Figures 5.10(b) and 5.12(a)) cause qualitative changes in the resulting images, noting that the smaller defect is non-circular; further, the



(a)



(b)



(c)

Figure 5.9: Photographs of artificial defects in aluminium plates. (a) circular defect of ~ 11 mm diameter in 0.69 mm thick plate; (b) a non-circular defect of ~ 5.8 mm maximum width in a 1.25 mm thick aluminium plate; (c) a rectangular slot of dimensions 1.3 mm \times 10.5 mm machined through a 0.79 mm thick plate.

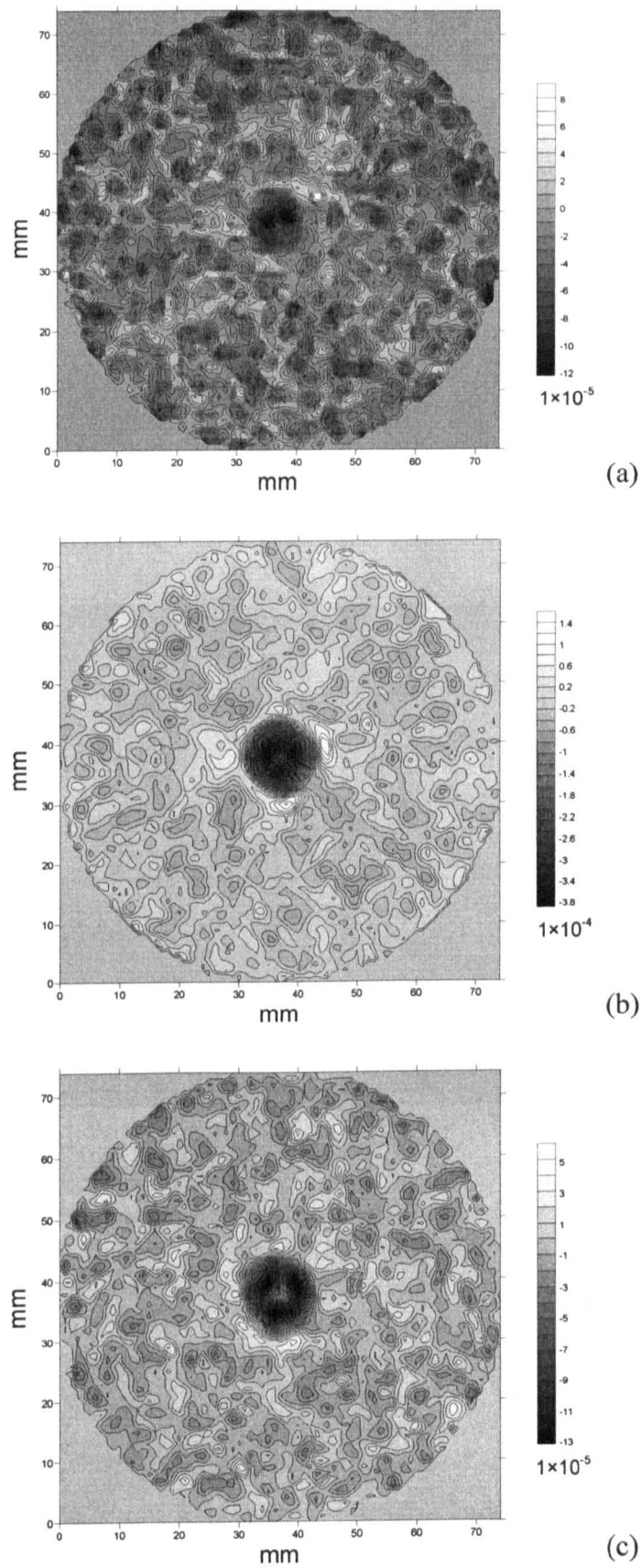


Figure 5.10: Tomographic attenuation image, formed from amplitude data, of the defect shown earlier in Figure 5.9(a), using data for (a) s_0 (b) a_1 and (c) s_1 modes.

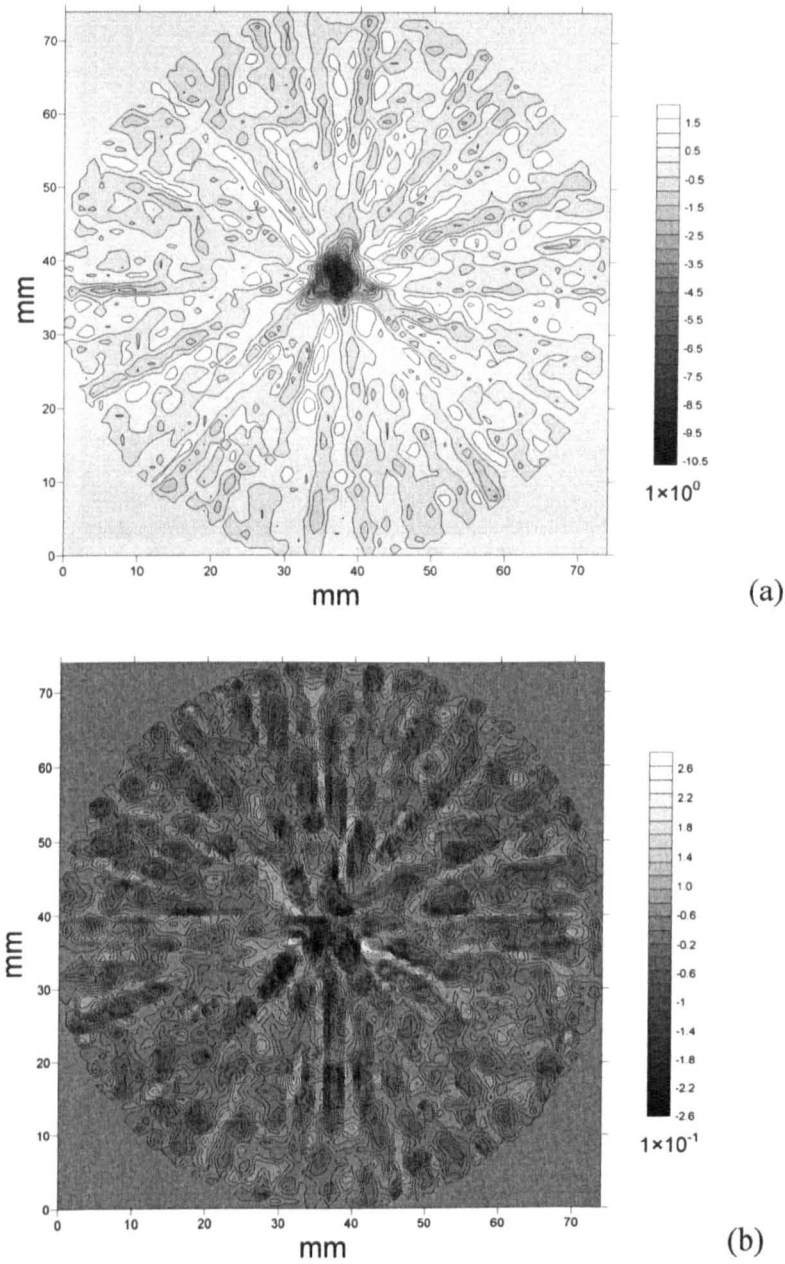


Figure 5.11: Tomographic reconstruction using the a_1 mode and the sample of Figure 5.9(a), in terms of, (a) a_1 arrival time (to give slowness image), and (b) shift in peak frequency.

image of the slot (Figure 5.12(b)) shows some asymmetry, indicating that it is non-circular.

The exact shape will not be reconstructed, due to the fact that the slot itself, being 10.5 mm long, was of the same order of size as the EMATs themselves (10 mm diameter). Thus, the relatively large transducer aperture would decrease imaging resolution. Further, the tomographic reconstruction

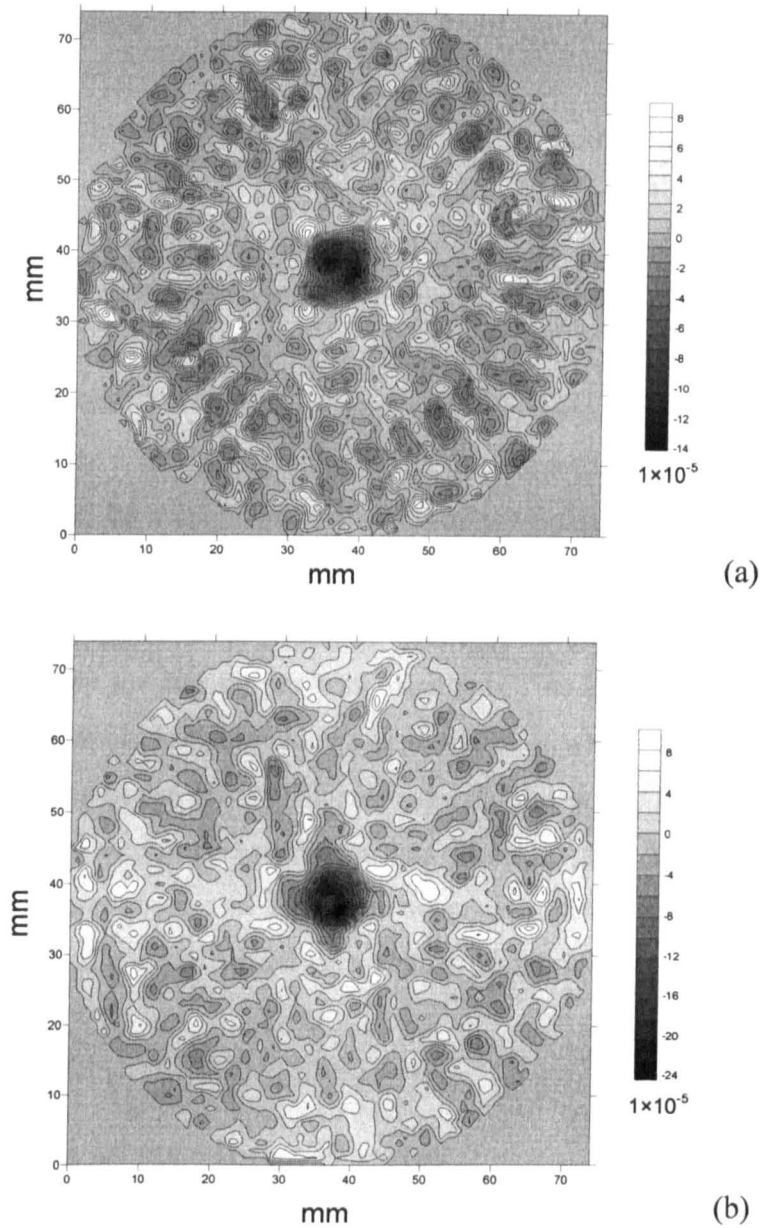


Figure 5.12: Tomographic attenuation images using the a_1 mode amplitude for (a) the smaller non-circular defect shown in Figure 5.9(b), and (b) the slot shown in Figure 5.9(c).

process uses interpolation, which tends to smooth out data in the θ direction (see Figure 5.5). These factors together dictate that the slot is not entirely resolved in shape; however, there is still evidence in the image of the presence of a non-circular defect. Note that, in addition, all time-frequency techniques have a limitation on resolution in either time or frequency, especially for finite duration signals. The EMAT aperture effect above will be in addition to these fundamental features of the WT approach.

5.7 Discussion

In this chapter, a time-frequency analysis method using a Continuous Wavelet Transform (CWT) has been used to characterise Lamb wave group velocity dispersion from broadband signals in plates. The use of a pair of non-contact EMATs generated Lamb waves containing both zero and higher order modes. These multiple modes were superimposed on each other in the time-domain waveform. The CWT was able to separate these modes in time-frequency space, a process known as mode extraction, to allow dispersion measurements to be made. The arrival times were then used with the known propagation distance to calculate the group velocity dispersion. The agreement between the time-frequency measured dispersion and the known theoretical dispersion curves for aluminium was excellent. The EMAT system was also used for tomographic imaging using Lamb waves. It was demonstrated that the performance was better for the higher order a_1 and s_1 modes than for the s_0 mode. Although amplitude-based data was found to give the best images in terms of dynamic range and signal to noise ratio, other methods using the frequency-shift of a given mode, or a change in mode arrival time, were also demonstrated.

5.8 The Use of the Morlet Wavelet

5.8.1 Background to the Morlet Wavelet

As stated at the start of this Chapter, there are various approaches to wavelet processing that could have been chosen. In the above, a “Mexican Hat” wavelet followed by a Hilbert Transform was used within the overall CWT approach, and this gave good results. The Mexican Hat wavelet has the ability to identify the positive and negative peaks of different frequency in a signal, and the Hilbert Transform was used to obtain the modulus of the wavelet coefficients, $|Wf(a, b)|$. However, the use of other wavelet types could be more efficient, as there are a wide variety of popular wavelet algorithms that exist,

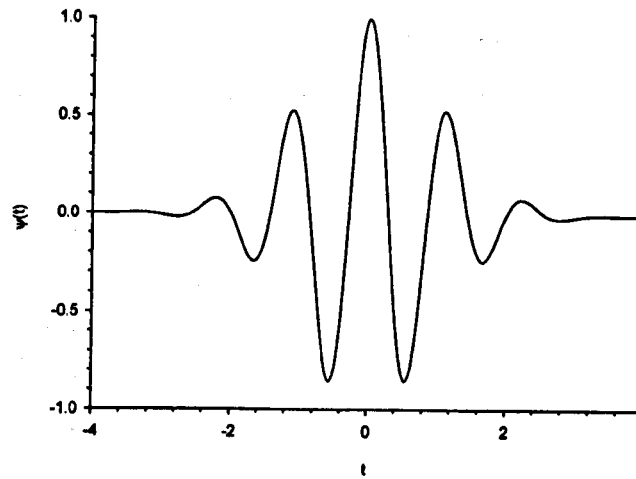
such as the Haar and Daubenchies. More examples of wavelet bases and functions can be found in [39].

Many other wavelets can thus be used to obtain time-frequency plot for ultrasonics mode identification. One example is the Morlet wavelet [40]. The Morlet wavelet is a complex-valued wavelet, and hence generates coefficients expressible with both a magnitude $|Wf(a,b)|$ and a phase $\varphi(a,b)$. Thus, a time-frequency analysis performed using the Morlet wavelet could be more sensitive to frequency information, and more detail concerning each ultrasonic mode could also be obtained. It was therefore decided to investigate the Morlet wavelet. The modulus of the wavelet coefficients computed by the Morlet wavelet can be presented using a wavelet map (in the same way as described in Figure 5.7), in which contours of constant amplitude of $|Wf(a,b)|$ are plotted versus time and frequency. The use of the Morlet wavelet has the advantage that a Hilbert Transform is not required, simplifying the analysis. The real and imaginary parts of a Morlet wavelet are shown in Figure 5.13, and the expression for the Morlet wavelet can be written as:

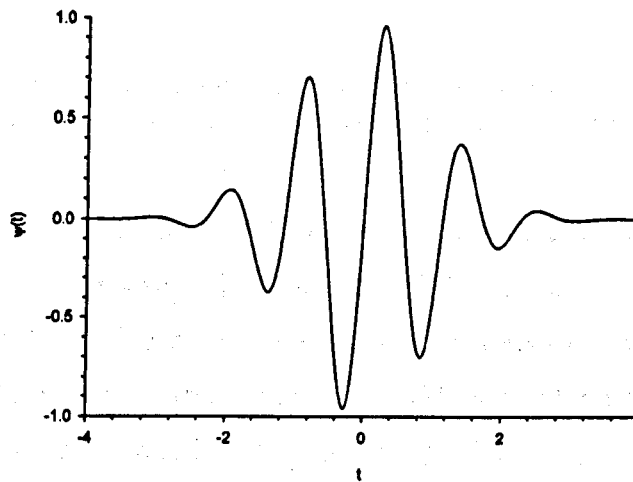
$$\psi(t) = \exp(iw_{\psi}t) \exp(-|t|^2/2) \quad (5.7)$$

where t is a dimensionless variable (e.g., a normalised time), and w_{ψ} is the dimensionless centre frequency of the wavelet [39-41]. The value of w_{ψ} determines the number of cycles relative to the central peak at $t = 0$. This value could affect the properties of the time-frequency analysis (i.e. the time-frequency uncertainty principle). The Morlet wavelet can thus be “tuned” for a particular application to provide an optimal compromise between time and frequency resolution.

In this chapter, $w_{\psi} = 1$ was chosen for the Morlet wavelet, which gives second, third, and fourth peak of amplitude 0.606, 0.135, and 0.011 times the central peak value respectively. The resultant wavelet is shown in Figure 5.13, identifying that the wavelet essentially vanishes after three oscillations. All other wavelets used in the analysis are translations and dilations of the mother



(a)



(b)

Figure 5.13: The complex-valued Morlet wavelet: (a) real part, (b) imaginary part.

wavelet, as was described in Equation (5.2). The value of a in equation (5.2) can be adjusted for a particular frequency range of interest. The wavelet transform algorithm presented in this chapter is therefore very flexible in producing time-frequency data. Applying the Fourier transform defined in Equation (5.7) gives the Morlet wavelet in the frequency domain [41], which can be defined as follows:

$$\psi(w) = (2\pi)^{-\frac{1}{2}} \exp\left(-\frac{(w - w_\psi)^2}{2}\right). \quad (5.8)$$

The Morlet wavelet can be viewed as a band-pass filter in the frequency domain. Figure 5.14 shows the resultant frequency spectrum for the Morlet wavelet function with two different values of scale a to illustrate this.

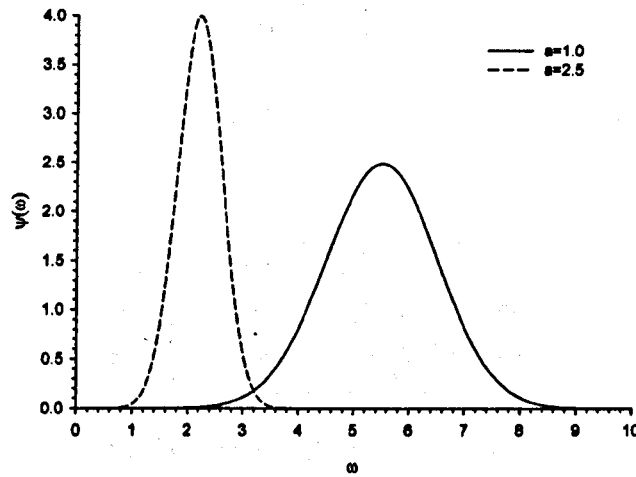


Figure 5.14: Frequency domain representation of the Morlet wavelet. An increase in wavelet scale, a , corresponds to a decrease in the centre frequency.

The wavelet family to which the Morlet wavelet belongs exhibit the property of linear phase, which is needed for signal analysis and image reconstruction [40]. These wavelets are both symmetric, which is useful in avoiding dephasing in wavelet processing [39], and exhibit infinite regularity, which is useful for getting high resolution image features [42]. More details can be found in [42].

The Morlet wavelet has been investigated in past work for the non-destructive inspection of concrete with a single receiving transducer [43]. It was suggested that the use of Morlet Wavelet to measure dispersion had the potential to separate the effects of inhomogeneities and damage. The use of Morlet wavelet has also been proposed for SNR improvement of highly scattering materials in ultrasonic NDT [44].

5.8.2 Analysis of EMAT data

Data from a pair of broadband EMATs on a 0.69 mm thick aluminium plate have been analysed using the Morlet wavelet. The recorded experimental waveform is shown in Figure 5.15(a), and the magnitude of the wavelet coefficients is plotted as changes in gray-scale as shown in Figure 5.15(b).

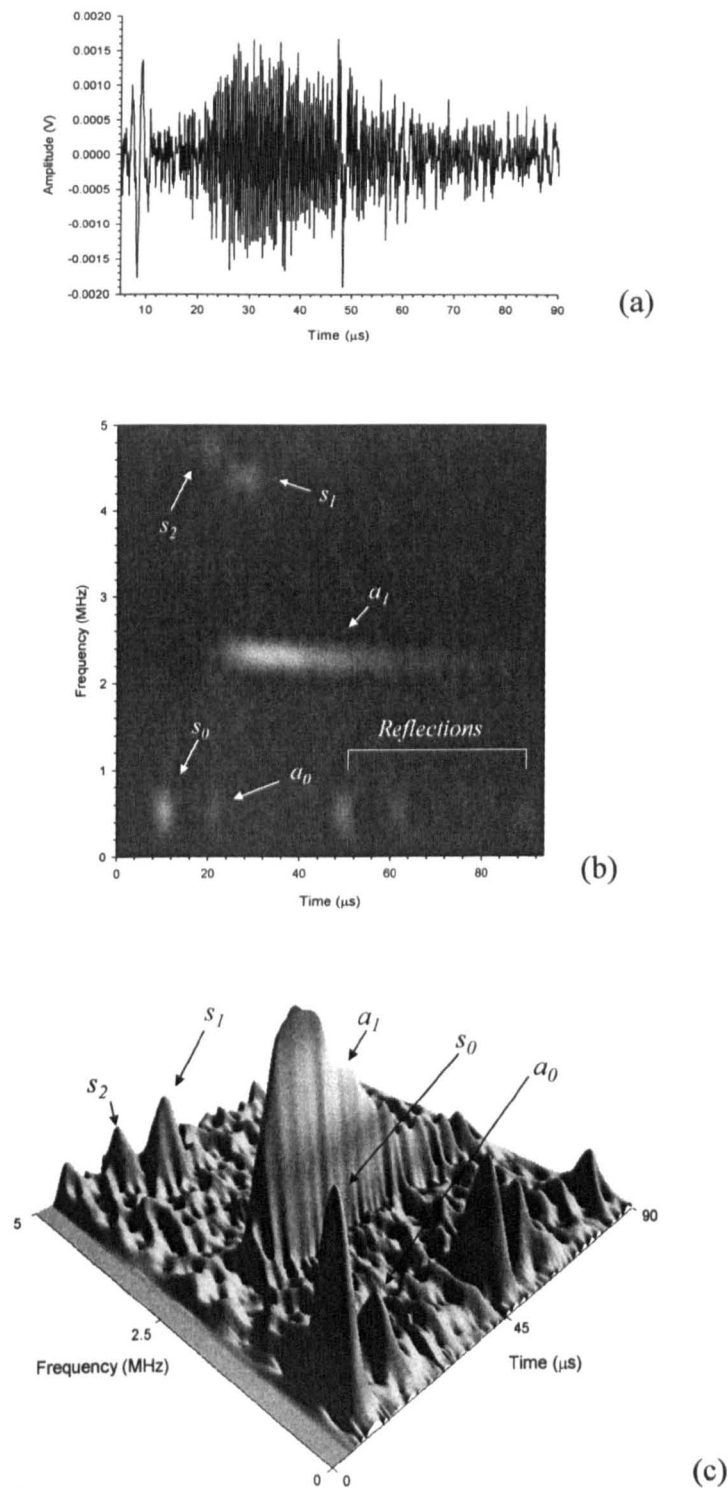


Figure 5.15: Experimental EMAT results for a 0.69 mm thick aluminium plate; showing (a) the received time waveform (expanded version of the waveform shown earlier in Figure 5.7(a)); (b) the corresponding CWT magnitude of the time waveform in (a); (c) 3D visualisation of the data shown in (b).

The low frequency range (*i.e.* the s_0 mode) corresponded to the wavelet coefficients that were obtained by the high scale version of the wavelet (*i.e.*, the mother wavelet being stretched in time). Similarly, the low scale wavelet (*i.e.*, being compressed) produced the high frequency range. This method has efficiently used a variable-width window-filtering technique to allow mode separation of wave modes in a waveform. Correlation magnitude values are then used to determine whether a wave mode is present at that pixel location. The separation of the modes is obvious, and it is clear that, as expected, the original time waveform contained both zero and higher order Lamb modes. The predicted modes are labelled. There is also evidence of reflections from the edge of the plate. Note that a 5 MHz frequency range was used for the display. Figure 5.15(c) shows a 3D visualisation plot corresponds to Figure 5.15(b).

To compare the results of the Morlet Wavelet to that of the “Mexican Hat” approach, Figure 5.16 shows the results from an experimental signal in 1 mm thick aluminium. This is the same data as used earlier in Figure 5.7, so that a direct comparison between the two wavelets can be made. The distance, l , was kept at ~ 50 mm centre to centre apart and the apparatus used was as discussed above. As before, the original time (Figure 5.16(a)) and CWT domain transforms (Figure 5.16(b)) are also shown, with the theoretical group dispersion curves for the 1 mm thick aluminium plate that superimposed on the experimental data in Figure 5.16(b). The experimental data is consistent with theoretical predictions in that the data lies on the predicted curves. However, the s_1 mode has the largest uncertainty as shown in the wavelet map. This is most likely due to the finite diameter of the devices, and the error associated to the thickness of the entire plate. Comparison to Figure 5.7 shows that the Morlet wavelet is very well localised in frequency, *i.e.* it has much sharper resolution in frequencies, whereas the Mexican hat followed by Hilbert Transform spectrogram has broader spreading in general for the experimental data in both time and frequency. This is because the Mexican hat is real-valued, and captures both positive and negative oscillations of the time series. The Morlet wavelet is complex-valued, and therefore can be more sensitive to the frequencies incorporated within the Wavelet Transform. The Morlet wavelet also has a good band-pass filter characteristic in frequency domain as shown earlier, and hence the results are better localised in frequency.

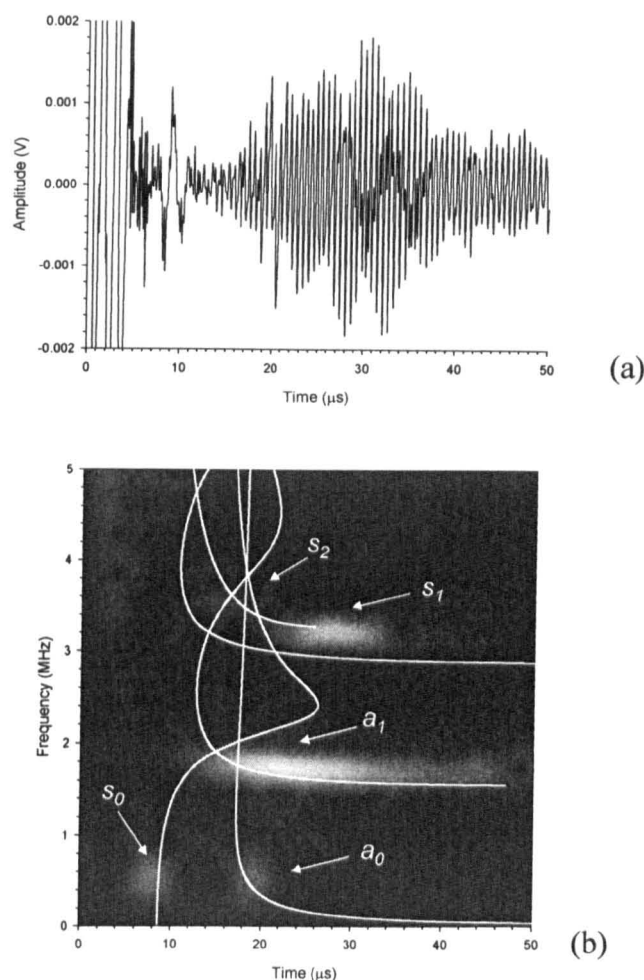


Figure 5.16: Experimental EMAT results for a 1 mm thick aluminium plate, showing (a) the received time waveform; (b) CWT magnitude using Morlet wavelet of the time waveform.

5.9 Discussion and Conclusions

The wavelet transform approach is very useful when wide bandwidth measurements are made, such as when EMATs are used, and where more than one acoustic mode is present. It allows the modes to be identified so that one particular mode can be chosen easily from a complicated time waveform. This approach is likely to be useful for many other applications where reflections and multiple modes are likely to be encountered.

The use of different types of wavelet, such as Mexican hat and Morlet, have been demonstrated to be powerful tools for mode detection and Lamb wave analysis. The most noticeable difference between the two wavelet

approaches is the fine structure in frequency resulting from the Morlet wavelet. The Mexican hat is real-valued and captures both the positive and negative oscillations of the time series as separate peaks. The subsequent use of a Hilbert Transform combines both positive and negative peaks into a single broad peak. Conversely, the Morlet is a complex wavelet in nature and contains both the magnitude and phase information, and hence, the resultant wavelet power combines both positive and negative peaks into a single sharp peak. The use of the Morlet wavelet would produce a plot similar to that from the Mexican hat approach.

Overall, the same features appear in both plots, approximately at the same location. However, a complex wavelet function will return information about both amplitude and phase and is better adapted for capturing oscillatory behaviour and modes isolation. Hence, this approach is recommended for better fast and efficient detection of complicated ultrasonic modes. However, in general it can also be stated that wavelet analysis is a good approach to the treatment of Lamb wave data from broad bandwidth EMATs.

5.10 References

- [1] K. S. Ho, D. R. Billson, D. A. Hutchins, "Ultrasonic Lamb wave tomography using scanned EMATs and wavelet processing," *Nondestr. Test. Eval.*, Accepted for Publication / In Print, 2006.
- [2] I. A. Viktorov, *Rayleigh and Lamb Waves*. New York : Plenum Press, 1967.
- [3] S. S. Kessler and C. T. Dunn, "Optimization of lamb wave actuating and sensing materials for health monitoring of composite structures," in *Proc. SPIE Int. Soc. Opt. Eng.*, 2003, pp. 123-133.
- [4] S. Zongqi, Y. Mao, W. Jiang and D. Zhang, "Mode analysis of lamb waves in hollow cylinder by means of 2-D fourier transformation," in *Proc. IEEE Ultrason. Symp.*, 1999, pp. 831-834.
- [5] Y. Hayashi, S. Ogawa, H. Cho and M. Takemoto, "Non-contact estimation of thickness and elastic properties of metallic foils by the wavelet transform of laser-generated Lamb waves," *NDT E Int.*, vol. 32, pp. 21-27, 1999.

- [6] R. Murayama, "Non-destructive evaluation of formability in cold rolled steel sheets using the SH₀-mode plate wave by electromagnetic acoustic transducer," *Ultrasonics*, vol. 39, pp. 335-343, 2001.
- [7] V. E. Sakharov, S. A. Kuznetsov, B. D. Zaitsev, I. E. Kuznetsova and S. G. Joshi, "Liquid level sensor using ultrasonic Lamb waves," *Ultrasonics*, vol. 41, pp. 319-322, 2003.
- [8] F. Jenot, M. Ouaftouh, M. Duquennoy and M. Ourak, "Corrosion thickness gauging in plates using Lamb wave group velocity measurements," *Meas. Sci. Technol.*, vol. 12, pp. 1287-1293, 2001.
- [9] J. Pei, M. I. Yousuf, F. L. Degertekin, B. V. Honein and B. T. Khuri-Yakub, "Lamb wave tomography and its application in pipe erosion/corrosion monitoring," in *Proc. IEEE. Ultrason. Symp. Part 1 (of 2)*, 1995, pp. 795-798.
- [10] C. B. Scruby and L. E. Drain, *Laser Ultrasonics : Techniques and Applications*. Adam Hilger, 1990.
- [11] D. A. Hutchins and D. W. Schindel, "Advances in non-contact and air-coupled transducers [US materials inspection]," in *Proc. IEEE Ultrason. Symp.*, 1994, pp. 1245-54.
- [12] X. Zhao, T. Qian, Z. Popovic, R. Zane, G. Mei, C. Walsh, T. Paing and C. Kwan, "A wireless ultrasonic guided wave structural health monitoring system for aircraft wing inspection," in *Review of Progress in Quantitative Nondestructive Evaluation*, 2007, pp. 1548-55.
- [13] J. D. McNamara and Lanza di Scalea, F., "Advances in health monitoring of railroad tracks," in *Smart Nondestructive Evaluation for Health Monitoring of Structural and Biological Systems*, 2002, pp. 250-61.
- [14] S. M. Prasad, K. Balasubramaniam and C. V. Krishnamurthy, "Structural health monitoring of composite structures using Lamb wave tomography," *Smart Mater Struct*, vol. 13, pp. 77-79, 2004.
- [15] C. H. Wang and L. R. F. Rose, "Plate-wave diffraction tomography for structural health monitoring," *AIP Conference Proceedings*, pp. 1615-22, 2003.
- [16] D. N. Alleyne and P. Cawley, "The interaction of Lamb waves with defects," *IEEE Trans. Ultrason. Ferroelectr. Freq. Control*, vol. 39, pp. 381-97, 05. 1992.
- [17] W. H. Prosser, M. D. Seale and B. T. Smith, "Time-frequency analysis of the dispersion of Lamb modes," *J. Acoust. Soc. Am.*, vol. 105, pp. 2669-76, 05. 1999.
- [18] C. Eisenhardt, L. J. Jacobs and J. Qu, "Experimental lamb wave spectra of cracked plates," in *AIP Conf. Proc.*, 2000, pp. 343-9.

- [19] P. S. Mahadev, K. R. Vinu, K. Balasubramaniam and C. V. KrishnaMoorthy, "Imaging of defects in composite structures using guided ultrasonics," in *Proc. SPIE - Int. Soc. Opt. Eng.*, 2003, pp. 700-3.
- [20] K. Luangvilai, L. J. Jacobs, P. Wilcox, M. J. Lowe and J. Qu, "Characterization of lamb waves in absorbing plates," in *Proc. SPIE - Int. Soc. Opt. Eng.*, 2004, pp. 33-41.
- [21] D. N. Alleyne and P. Cawley, "The measurements and prediction of lamb wave interaction with defects," in *IEEE 1991 Ultrasonics Symposium Proceedings*, 1991, pp. 855-7.
- [22] K. R. Leonard and M. K. Hinders, "Multi-mode Lamb wave tomography with arrival time sorting," *J. Acoust. Soc. Am.*, vol. 117, pp. 2028-38, 04. 2005.
- [23] J. L. Rose, M. J. Avioli and W. -. Song, "Application and potential of guided wave rail inspection," *Insight Non Destr. Test Cond. Monit.*, vol. 44, pp. 353-358, 2002.
- [24] A. Demma, P. Cawley, M. Lowe, A. G. Roosenbrand and B. Pavlakovic, "The reflection of guided waves from notches in pipes: A guide for interpreting corrosion measurements," *NDT and E Int.*, vol. 37, pp. 167-180, 2004.
- [25] M. Niethammer, L. J. Jacobs, J. Qu and J. Jarzynski, "Time-frequency representation of Lamb waves using the reassigned spectrogram," *J. Acoust. Soc. Am.*, vol. 107, pp. 19-24, 05. 2000.
- [26] L. B. Magalas and J. Kwasniewski, "Selected applications of the wavelet transform," *Diffus. Def. Data Pt. B*, vol. 89, pp. 355-64, 2003.
- [27] S. T. Quek, Q. Wang, L. Zhang and K. H. Ong, "Practical issues in the detection of damage in beams using wavelets," *Smart Mater. Struct.*, vol. 10, pp. 1009-17, 10. 2001.
- [28] M. Lemistre and D. Balageas, "Structural health monitoring system based on diffracted lamb wave analysis by multiresolution processing," in *Smart Mater. Struct.*, 2001, pp. 504-11.
- [29] R. Gubbala and V. S. Rao, "Health monitoring of adhesively bonded composite patch repair of aircraft structures using wavelet transforms of lamb wave signals," in *Proc. SPIE - Int. Soc. Opt. Eng.*, 2003, pp. 33-40.
- [30] Yuh-Tay Sheen and Chun-Kai Hung, "Constructing a wavelet-based envelope function for vibration signal analysis," *Mech. Syst. Signal Process*, vol. 18, pp. 119-26, 01. 2004.
- [31] Liu Chong Chun and Q. Zhengding, "A method based on morlet wavelet for extracting vibration signal envelope," in *Proceedings of 5th International Conference on Signal Processing*, 2000, pp. 337-40.

- [32] A. Ouergli, "Hilbert transform from wavelet analysis to extract the envelope of an atmospheric mode: examples," *J. Atmos. Ocean. Technol.*, vol. 19, pp. 1082-6, 07. 2002.
- [33] Y. Xiao and Y. Juebang, "Complex analytical wavelet transform for the extraction and analysis of speech signal envelopes," *Acta Electronica Sinica*, vol. 27, pp. 142-4, 05. 1999.
- [34] D. P. Jansen and D. A. Hutchins, "Immersion tomography using Rayleigh and Lamb waves," *Ultrasonics*, vol. 30, pp. 245-54, 1992.
- [35] J. C. P. McKeon and M. K. Hinders, "Parallel projection and crosshole Lamb wave contact scanning tomography," *J. Acoust. Soc. Am.*, vol. 106, pp. 2568-77, 11. 1999.
- [36] D. A. Hutchins, D. P. Jansen and C. Edwards, "Lamb-wave tomography using noncontact transduction," *Ultrasonics*, vol. 31, pp. 97-103, 1993.
- [37] A. C. Kak and M. Slaney, *Principles of Computerized Tomographic Imaging*. Philadelphia : Society for Industrial and Applied Mathematics, 2001.
- [38] R. M. Lewitt, "Reconstruction algorithms: transform methods," *Proc IEEE*, vol. 71, pp. 390-408, 03. 1983.
- [39] D. F. Walnut, *An Introduction to Wavelet Analysis*. Boston : Birkhauser, 2002.
- [40] D. B. Percival and A. T. Walden, *Wavelet Methods for Time Series Analysis*. Cambridge : Cambridge University Press, 2000.
- [41] H. Stark, *Wavelets and Signal Processing : An Application-Based Introduction*. New York : Springer, 2005.
- [42] S. G. Mallat, *A Wavelet Tour of Signal Processing*. London : Academic Press, 1998.
- [43] M. L. Peterson, S. Srinath, T. Lambert, D. Woodham and M. Schuller, "Wavelet display of dispersion in concrete using Paul and Morlet wavelets," *Nondestr. Test. Eval.*, vol. 15, pp. 151-169, 1999.
- [44] N. Ruiz-Reyes, P. Vera-Candeas, J. Curpian-Alonso, R. Mata-Campos and J. C. Cuevas-Martinez, "New matching pursuit-based algorithm for SNR improvement in ultrasonic NDT," *NDT&E International*, vol. 38, pp. 453-8, 2005.

Chapter 6

Texture Measurement of Metal Sheets

6.1 Introduction

As has been discussed elsewhere in this thesis, the excitation and detection of Lamb waves is complex and generally consists of many dispersive modes. The characteristics of Lamb waves vary with frequency, material properties, and thickness of a plate; furthermore, modes with different velocities can be excited at the same time. This makes mode identification difficult. In order to estimate the arrival times efficiently without the disturbance of modes overlapping in a dispersive media or from noise, the Continuous Wavelet Transform (CWT) approach was described in Chapter 5 as a very useful tool for adapting to the mode extraction and arrival times estimation. The CWT is superior approach for time-frequency analysis tools because its time scale width of window can be stretched to match the original signal, especially in ultrasonic Lamb wave studies. This makes it particularly useful for non-stationary signal analysis, such as noises and transients. In addition, a more efficient approach can be obtained by using Digital Wavelet Transform (DWT) signal processing technique. This fast algorithm is the multi-resolution analysis, which is a non-redundant decomposition [1]. However, the drawback of non-redundant transform is their non-invariance in time, *i.e.*, the original signal can not be synthesised from the wavelet coefficients perfectly.

In this Chapter, multiple ultrasonic Lamb wave modes are considered for the non-destructive characterisation of texture and formability of metal sheets. Because the standard DWT is translation variant owing to the sub-sampling procedure, the signals reconstructed from these wavelet coefficients may include some distortion. This is undesired especially for physical acoustic characterisation. In order to extract the accurate wave modes and to estimate their arrival time from ultrasonic signals quickly and efficiently for on-line

applications, a method based on the undecimated DWT [2] is used in this Chapter. This process is called the stationary wavelet transform (SWT), which was introduced to make the wavelet decomposition time invariant [3]. This technique is well established and it has been used to improve the performance of wavelets in signal de-noising [4–7]. Moreover, the existence of a fast iterative implementation of the SWT decomposition used in this work makes this method very practical for work in texture measurement.

6.2 Overview of Texture Measurements

Any polycrystalline metal contains texture, whether natural or induced. Such materials have a slightly anisotropic character, which originates from the preferred orientation of the crystallite of texture [8, 9]. The texture is characterised by a set of dimensionless parameters W_{lmn} , called orientation distribution coefficients (ODCs). The characteristics of these sheets can be effectively controlled by this texture. For instance, steel sheets for the outer panels of automobiles and refrigerators have characteristics which prevent damage during press forming through control of this texture. This type of steel sheet has good formability.

There are several metallic materials where the chemical composition and manufacturing conditions are carefully controlled to develop appropriate texture for specific purposes. One good example is grain-oriented Fe-3%Si alloy sheets, which have easy directions of magnetisation closely aligned along the rolling direction. Because of the strong magnetic polarisation [10], these electrical sheets are used as core materials for power transformers. Another example is cold-rolled steel sheets used for automobile body parts, beverage cans, etc. Because the sheets are pressed and stretched to form parts, they should have such a plastic anisotropy that they deform easily in the sheet plane with little thickness reduction.

Traditionally, ODCs are obtained through X-ray [11] or neutron diffraction techniques [12, 13]. However, while these techniques are generally preferred for laboratory studies, problems arise while applying these techniques in a production environment. Neutron techniques are usually impractical

because of the absence of portable sources, and X-ray techniques are rather expensive and introduce safety questions associated with the presence of radiation. Hence ultrasonic techniques have received considerable attention as an alternative technology for monitoring the texture of metal sheet over the past decades [14–23]. Many of these studies used EMATs for ultrasonic generation and detection.

Determining ultrasonic velocities enables the measurement of the degree of anisotropy in polycrystalline metals. These change with the propagation and polarisation directions relative to the rolling and normal directions, and in the case of a rolled plate, showing an orthorhombic symmetry [24, 25]. During thermomechanical processes, crystallites rotate during crystal slip and the crystal orientations tend to be partially aligned in a certain direction. However, the magnitude of the anisotropy is usually small and the absolute velocity differences are $\sim 100 \text{ ms}^{-1}$ at most [15]. Other aspects including grain size, shape, precipitation particles, and even lattice defects are less influential than the anisotropy when lower measurement frequencies are used [26, 27]. The effect of the texture is much larger than that caused by stress [28], although there is an interest in measuring residual stress non-destructively [29]. For pure stress measurements, texture effects should be minimised [30]. Various ultrasonic modes have been proposed for use in texture measurement. These include the symmetrical Lamb wave (s_0) mode [31], the Shear Horizontal wave (SH) [32], and Rayleigh wave [33].

In a typical experimental setup, the velocities of the waves are measured as a function of wave propagation angle with respect to the rolling direction of the plate. Lamb waves, as illustrated in Chapter 5 are dispersive, and this dispersion must be considered in order to isolate the small, texture-induced shifts in the velocity. There are two approximate dispersion correction methods, one proposed by Thompson, et al [11] and the other introduced by Hirao and Fukuoka [26]. Later in [34], it is found that when the plate thickness to wavelength ratio, t/λ is less than 0.15, both Thompson's and Hirao's methods work satisfactorily. When the t/λ ratio exceeds 0.3, neither Thompson's nor Hirao's dispersion correction method provide adequate corrections for the texture measurement techniques. Within the range of 0.15 - 0.3, Thompson's

method is recommended for weakly anisotropic sheets and plates and Hirao's method may be more appropriate for some strongly anisotropic cases.

In this Chapter, EMATs are used to generate multiple ultrasonic Lamb wave modes for the characterisation of texture in metal sheets. While this has been studied in many previous papers, as described above, a different approach to the analysis is taken in this thesis. Since only three constants (W_{400} , W_{420} , and W_{440}) define the elastic anisotropy in the most commonly used approximation, in previous work, these constants were evaluated using ultrasonic velocities measured typically at 0° , 45° and 90° with respect to the metal sheet. However, greater accuracy in calculating these ODCs values can potentially be obtained by fitting the theoretical angular dependent velocity to the experimental data. It is then possible to extract the ODCs and obtain some degree of confidence in the values from the correlation of the fit. This process will use the Stationary wavelet transform (SWT) as a convenient and accurate technique for extracting the required data from selected Lamb wave modes. So that this approach can be implemented conveniently in the presence of multiple Lamb modes.

6.2.1 Theoretical Background

Several authors have developed a quantitative relation between the observed elastic constants of polycrystalline metal, the acoustic velocities in various directions and the crystallographic orientation distribution of the material. This is most often written in terms of the orientation distribution coefficients W_{lmn} . Roe [8, 9] showed that by considering the elastic coefficients for each individual grain's crystallographic orientation and averaging over the whole range of possible crystallographic orientations subject to the crystalline orientation distribution function (CODF), written as $w_{(\varepsilon\theta\varphi)}$, the effective elastic coefficients of a polycrystalline metal sheet can be determined. This is a function of the values of, W_{lmn} , as follows:

$$w_{(\varepsilon\theta\varphi)} = \sum_{l=0}^{\infty} \sum_{m=-l}^l \sum_{n=-l}^l W_{lmn} Z_{lmn}(\varepsilon) \exp^{-im\theta} \exp^{-in\varphi} \quad (6.1)$$

Here, $Z_{lmn}(\epsilon)$ are associated Legendre functions as defined by Roe [9]. The effective elastic constants in the reference frame of the sheet can then be determined by integrating a suitable equation (between the elastic constants in the sheet reference frame and the reference frame of an individual grain) over all angles subject to the CODF. It has been shown by Sayers [35] that, using symmetry arguments, the effective elastic coefficients are determined by only three independent ODCs; using Roe's notation [9] these are referred to as W_{400} , W_{420} and W_{440} . Equations have been derived [34] relating the variation in acoustic velocity ($V(\theta)$) parallel to the sheet as a function of angle (θ) to the three ODCs:

$$(V(\theta))^2 = \alpha_1 + \alpha_2 W_{400} - \alpha_3 W_{420} \cos(2\theta) + \alpha_4 W_{440} \cos(4\theta). \quad (6.2)$$

Here, α_1 , α_2 , α_3 , and α_4 are all constants that depend on the specific Lamé constants and density for the isotropic material. Obtaining the values of the ODCs is typically performed by firstly measuring velocities at 0° , 45° , and 90° to the rolling direction, and this can be expressed as:

$$4\alpha_4 W_{440} = V(0)^2 + V(90)^2 - 2V(45)^2 \quad (6.3)$$

$$2\alpha_3 W_{420} = V(90)^2 - V(0)^2 \quad (6.4)$$

$$4\{\alpha_1 + \alpha_2 W_{400}\} = 2\{V(45)^2 + V(0)^2\} + \{V(90)^2 - V(0)^2\} \quad (6.5)$$

where again $V(\theta)$ is the velocity in the direction at an angle θ to the rolling direction.

The approach to be described here involves measuring the velocity over many angles, through 360° , giving a curve which can be fitted to theory using an optimisation procedure. The ODCs obtained by fitting the velocities can be calculated using Equation (6.2). The anisotropy is then estimated by varying the theoretical parameters to achieve this best fit. This is a more accurate method than simply using measurements in three directions. The ODCs obtained by

using three velocity values at 0° , 45° , and 90° can be calculated using Equations (6.3) - (6.5).

A simulation has been carried out in Matlab to illustrate the difference between the two approaches. Figure 6.1 shows the estimated velocities through 360° using Equation (6.2). The velocity values were first obtained by assuming the ODCs are known, and these were W_{400} , W_{420} and W_{440} of 2.82×10^{-3} , -5.18×10^{-4} and 4.29×10^{-3} respectively. Note the ODCs are dimensionless. The physical parameters used are the same as those used in [33]. For comparison, the ODCs were then calculated using only three simulated velocities at 0° , 45° , and 90° . The ODCs can be obtained using Equation (6.3) - (6.5), giving values for W_{400} , W_{420} and W_{440} of 2.82×10^{-3} , -5.1768×10^{-4} and 4.3×10^{-3} respectively. The two different approaches yield ODCs that are close to each other. The agreement between the two approaches demonstrates that using just three measurements is a valid approach, in some circumstances, where accurate data can be obtained. However, in some other situations, where there is greater uncertainty (e.g. very noisy measurements), a curve fitting procedure is much more likely to give better results. This is the main reason for investigating this method.

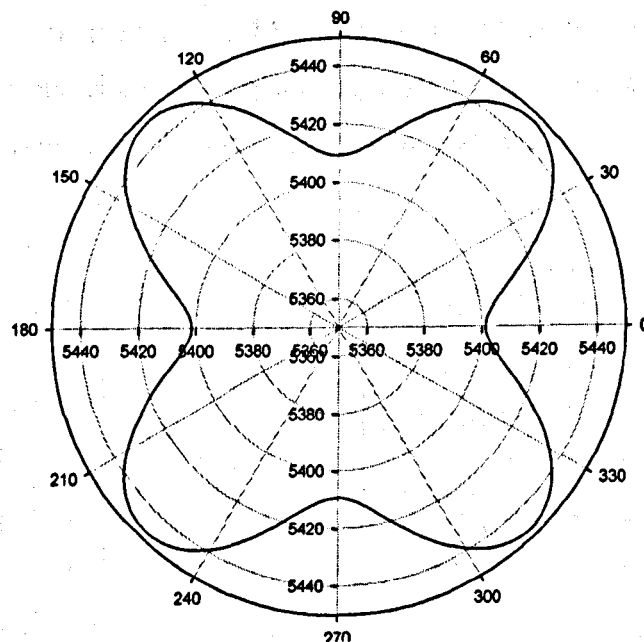


Figure 6.1: The estimated velocities (ms^{-1}) through 360° simulations.

6.3 Transducer design

In this Chapter, magnetostrictive type EMATs have been used to transmit and receive Lamb waves for the inspection of ferromagnetic metal sheets. This is due to the fact that for the case of the magnetostrictive type EMAT, the required driving current for optimum transduction efficiency is much less in comparison to the Lorentz force type EMAT [36, 37]. The magnetostrictive effect occurs when a dynamic field is generated in the direction parallel to the static magnetic field. This configuration produces periodic patterns of tensile and compressive strains (longitudinal displacement) in a ferromagnetic substrate [38, 39]. The stress varies the magnetic permeability of the ferromagnetic material. This results in a flux density change under the static field, and the eddy current is then introduced into the coil. This configuration generates little ultrasonic energy in a non-magnetic metal, since the induced eddy currents are parallel to the bias field and the driving Lorentz forces vanish. Hence, the texture work presented here is aimed towards ferromagnetic materials such as certain steels.

Thin metal sheets are widely used to manufacture the bodies of cars and in electrical products. The inspection of these thin metal sheets can be carried out using Lamb waves, as described earlier in Chapter 5. The phase velocity generated using meanderline EMAT may be found using the Rayleigh-Lamb frequency relations shown in Equation (4.1) and (4.2). Figure 6.2 shows the schematic diagram of EMAT meanderline configuration.

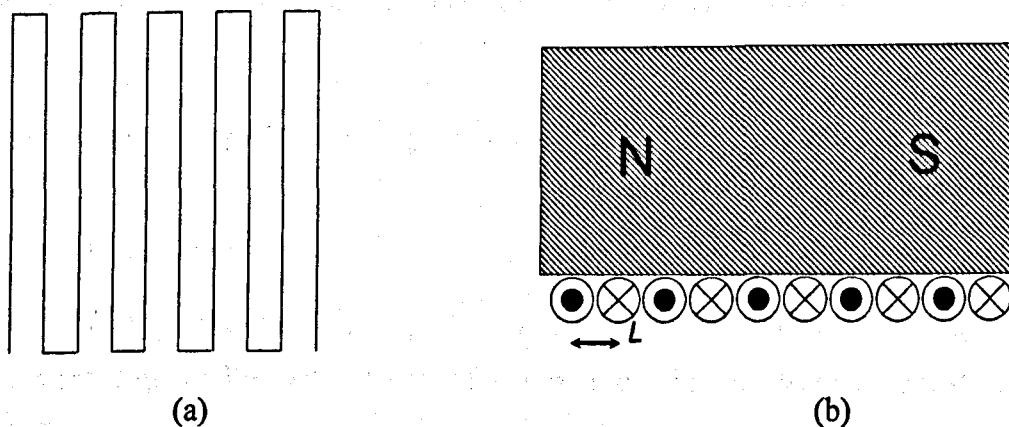


Figure 6.2: Schematic diagram of a meanderline EMAT showing (a) the coil geometry, and (b) the EMAT meanderline configuration.

The EMAT consists of a meander-line coil and a permanent magnet which applies the magnetic field in the propagation direction. The spacing of the coil L , corresponds to the half wavelength of the Lamb wave, *i.e.* $L = \lambda/2$. Hence, the cut-off frequency, f associated to the detectable Lamb mode is obtained by:

$$f = \frac{c_p}{2.L} = \frac{c_p}{\lambda} \quad (6.6)$$

The fundamental characteristic of a Lamb wave is its phase velocity c_p which is a function of the frequency of the wave and the thickness of the plate.

The generation and the reception of the possible Lamb modes using an EMAT meanderline configuration corresponding to a frequency range up to 11 MHz is predicted and is shown in Figure 6.3. Figure 6.3(a) shows the relationship between the driving frequency and the phase velocity for a 0.39 mm steel sheet. The straight line in Figure 6.3(a) corresponding to the wavelength (λ) defined by the meanderline spacing ($\lambda = 1.8$ mm). The calculation was obtained using Equation (6.6). As can be seen in Figure 6.3(a), it is possible to transmit and receive s_0 , a_0 , s_1 , a_1 , and s_2 wave modes using a 1.8 mm wavelength meanderline EMAT. In other words, this indicates that the multiple Lamb modes can be generated when the distance between the coil spacing, L is narrow, and only the lower-order modes can be generated when L is large. Figure 6.3(b) shows the relationship between the driving frequency and the group velocity for a 0.39 mm steel sheet. Hence, the group velocity for the s_0 , a_0 , s_1 , a_1 , and s_2 modes can be predicted, as shown in Figure 6.3(b).

6.4 Stationary Wavelet Processing

6.4.1 Introduction

Wavelet processing is expected to be an effective method to analyse the transient signal. The advantages of using a continuous wavelet transform (CWT) for signal localisation was demonstrated in Chapter 5. This Chapter

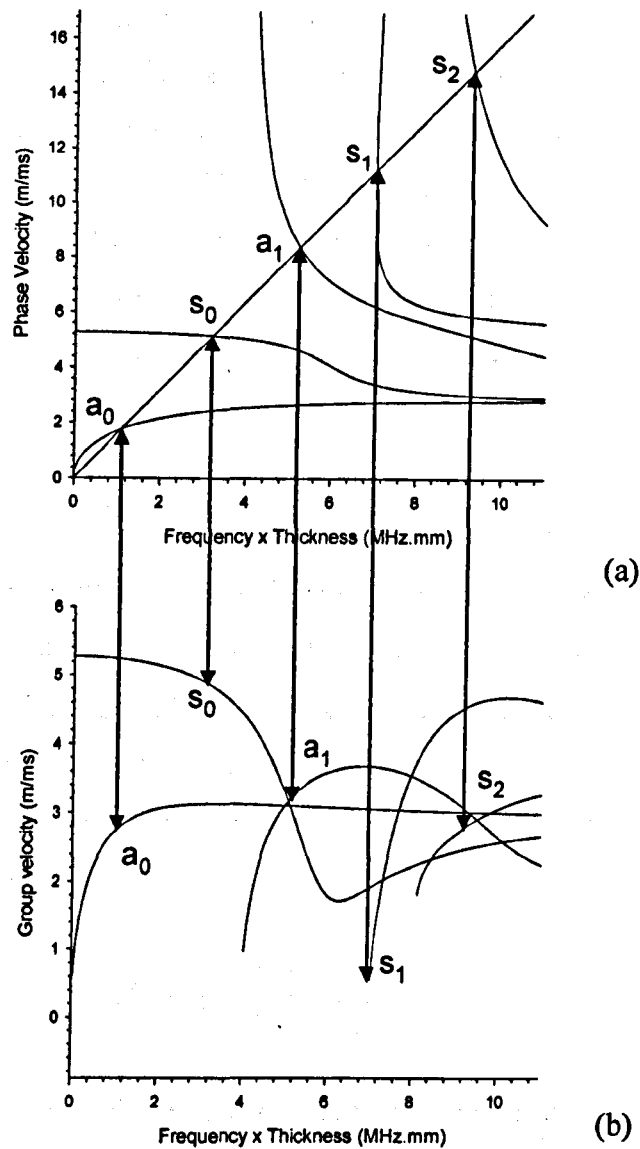


Figure 6.3: Lamb wave modes prediction in steel using the Rayleigh-Lamb dispersion curves, showing (a) phase velocity and (b) group velocity. The straight line in (a) corresponds to the wavelength (λ) defined by the meanderline spacing ($\lambda=1.8\text{mm}$).

focuses on the multi-scale discrete wavelet method where the analysis in time and in scale is discrete as opposed to the CWT where the analysis occurs continuously. There are certain advantages to using SWT analysis. For example, the band centre frequency for the SWT is changed by a factor of two when rescaling and the band centre frequency of CWT is changed continuously when rescaling. Hence, the multiple modes and reflections can be identified and separated more efficiently by using the SWT approach.

As we have seen, wavelets are mathematical functions that split up data into different frequency components, and each component represents a

resolution that is matched to its scale. Wavelet decomposition introduces the notation of scale as an alternative to frequency, and maps a signal into a time-scale plane, which is equivalent to the time-frequency plane used in the short time Fourier Transform (STFT) [40]. Each scale in the time-scale plane corresponds to a certain range of frequencies in the time-frequency plane. When compared to traditional Fourier transforms that lose the time resolution of non-stationary signals, wavelet transforms retain both the time and frequency resolution [41].

6.4.2 Theoretical Background

The SWT provides the decomposition of the original signal $f(t)$ onto a set of basis functions that are obtained by dilation of a mother wavelet $\psi(t)$. The signal is decomposed by time convolution with a set of elementary wavelets, often called daughter wavelets, which are scaled (*i.e.* they are stretched or compressed versions of the mother wavelet, $\psi(t)$). Mathematically, this can be written as:

$$\psi_{j,k}(t) = \frac{1}{2^j} \psi\left(\frac{\tau}{2^j} - k\right) \quad j, k = 1, 2, \dots \quad (6.7)$$

In discrete wavelet transforms the frequency parameters (s) are taken as an integer power of 2, *i.e.* $s = 2^j$, $j = 1, 2, \dots$. The time parameter τ is taken as a series of integers k . For simplicity, reference to frequency, f is replaced by reference to scale, a , where $f = 1/a$. Another aspect of the wavelet transform is that the localisation or compactness of the wavelet increases as frequency or scale increases. In other words, a higher scale corresponds to a finer localisation and vice versa. The multi-resolution formulation needs two closely related basic functions. In addition to the mother wavelet $\psi(t)$, there is a need for another basic function called the scaling function, often called the father wavelet, which is denoted by $\phi(t)$. The scaling and translation of $\phi(t)$ is defined similar to Equation (6.7). The scaling function $\phi(t)$ coefficients are derived by reversing the order of the wavelet function $\psi(t)$ coefficients, and then reversing the sign of every second coefficient index. Mathematically, this is written as:

$$\varphi(t)_n - (-1)^n \psi(t)_{(2N+1-n)} \quad n = 1, 2, \dots, 2N \quad (6.8)$$

where n is the coefficient index. Here, let A_j and D_j be a pair of operators, at j th resolution. $A_j[f(t)]$ is an approximation (low-frequency contents) of the signal $f(t)$ and $D_j[f(t)]$ represents the detail of the signal (high-frequency contents). This can be written as:

$$A_j[f(t)] = f(t) * \phi_j(t) \quad (6.9)$$

$$D_j[f(t)] = f(t) * \psi_j(t) \quad (6.10)$$

where $\phi_j(t)$ are the smooth scaling orthogonal bases, $\psi_j(t)$ the orthogonal wavelet bases, and $*$ denotes convolution. Furthermore, $\phi_j(t)$ and $\psi_j(t)$ are convoluted through a pair of quadrature mirror filters QMF, $h(t)$ and $g(t)$ defined as:

$$\phi_j(t) = h(t) * \phi_{j-1}(t) \quad (6.11)$$

$$\psi_j(t) = g(t) * \psi_{j-1}(t) \quad (6.12)$$

where $j = 1, 2, \dots, t = 1, 2, \dots, N$, and

$$h_{j+1}(k) = [h]_{\uparrow 2} * h_j(k) \quad (6.13)$$

$$g_{j+1}(k) = [g]_{\uparrow 2} * g_j(k) \quad (6.14)$$

where the subscript $\uparrow m$ indicates the up-sampling by a factor of m , and k is the equally sampled discrete time. At each level, when the high-pass and low-pass filters are applied to the data, the two new sequences have the same length as the original sequence, and the filters at each level are modified by padding them

out with zeros. It is helpful to think of the coefficients, $\phi_j(t)$ and $\psi_j(t)$ as a time-varying filter. These two orderings of the coefficients are called a QMF pair in signal processing, and the matrix is applied in a hierarchical algorithm. The SWT decomposition processes are schematically shown in Figure 6.4. Each step only involves a convolution with the basic filters h_j and g_j , and up-sampling is obtained by inserting an appropriate number of zeros. This will be illustrated in the simulation shown in Section 6.4.2. Each matrix application brings out a higher resolution of the data while at the same time smoothing the remaining data. To assemble the components back into the original signal is called reconstruction or synthesis. The signal's reconstruction from the approximation coefficients, $A_j[f(t)]$ and the detail coefficients, $D_j[f(t)]$ can be obtained by the convolution process shown in Equation (6.11) and (6.12), except that the scaling function $\phi_j(t)$ and the wavelet function $\psi_j(t)$ filtering functions are in the reverse order (the functions are flipped from left to right). The mathematical manipulation that described the synthesis is called the inverse stationary wavelet transform (ISWT). The SWT reconstruction also has a fast iterative implementation, and the mathematical expression is written in the same form as Equation (6.13) to (6.14) where up-sampling is performed at every level.

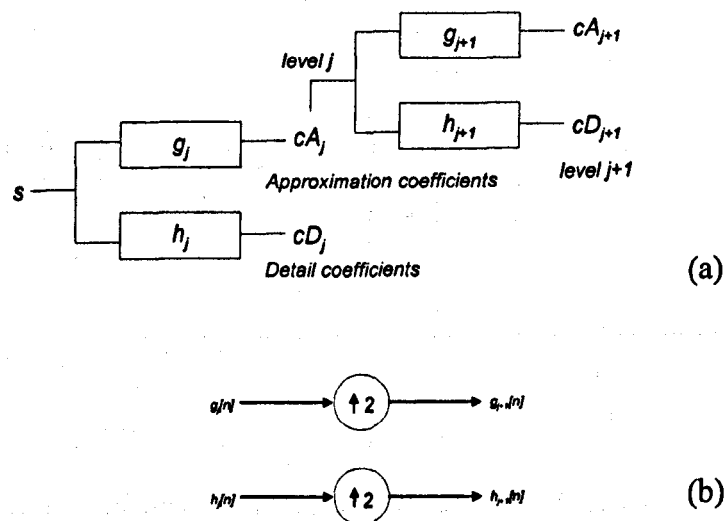


Figure 6.4: The SWT signal decomposition procedure, (a) A schematic diagram of a single level signal decomposition procedure using SWT, and (b) filter characteristics.

6.4.3 SWT Simulation

The ability to perform signal decomposition and reconstruction using a SWT is illustrated in Figures 6.5 to 6.8. The input signal, $f(x)$, is composed of the sum of two sine waves with arbitrary scale amplitude. Figure 6.5(a) shows the first simulated sine wave. The sine wave is the lower frequency component consisting of 8 cycles and the frequency was set to 1 MHz. Figure 6.5(b) shows the other simulated sine wave, which is the higher frequency component consisted of 75 cycles and the frequency was set to 8 MHz. These two sine waves are superimposed (added) in time and this is shown in Figure 6.5(c), and the frequency content of this superimposed signal is shown in Figure 6.5(d).

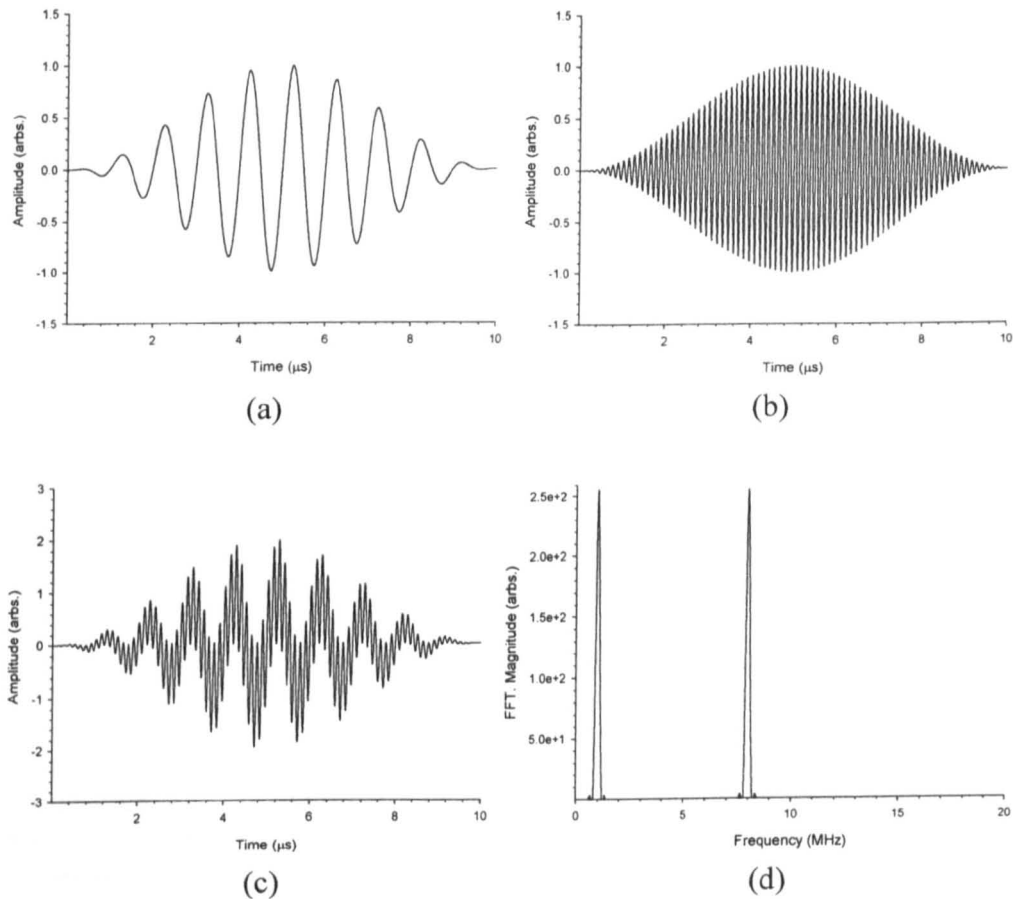


Figure 6.5: Simulated input signals used for the SWT, (a) 1 MHz wave component, (b) 8 MHz wave component, (c) simulated waves (a) and (b) superimposed, and (d) frequency spectrum of (c).

The mother wavelet used in this simulation and through-out in this study was a Finite Impulse Response (FIR) based approximation of the Meyer

wavelet, *dmeyer*, allowing fast wavelet coefficients calculation using SWT. An example of a *dmeyer* wavelet function is shown in Figure 6.6(a), and the existence of the corresponded scaling function is shown in Figure 6.6(b). The *dmeyer* wavelet, $\psi(t)$ and scaling function $\phi(t)$ coefficient can be represented as a High-pass and a Low-pass filter respectively. The frequency spectra corresponding to the *dmeyer* $\psi(t)$, and $\phi(t)$ are shown in Figure 6.6(c) and 6.6(d) respectively. This simulation was performed using three hierarchically levels.

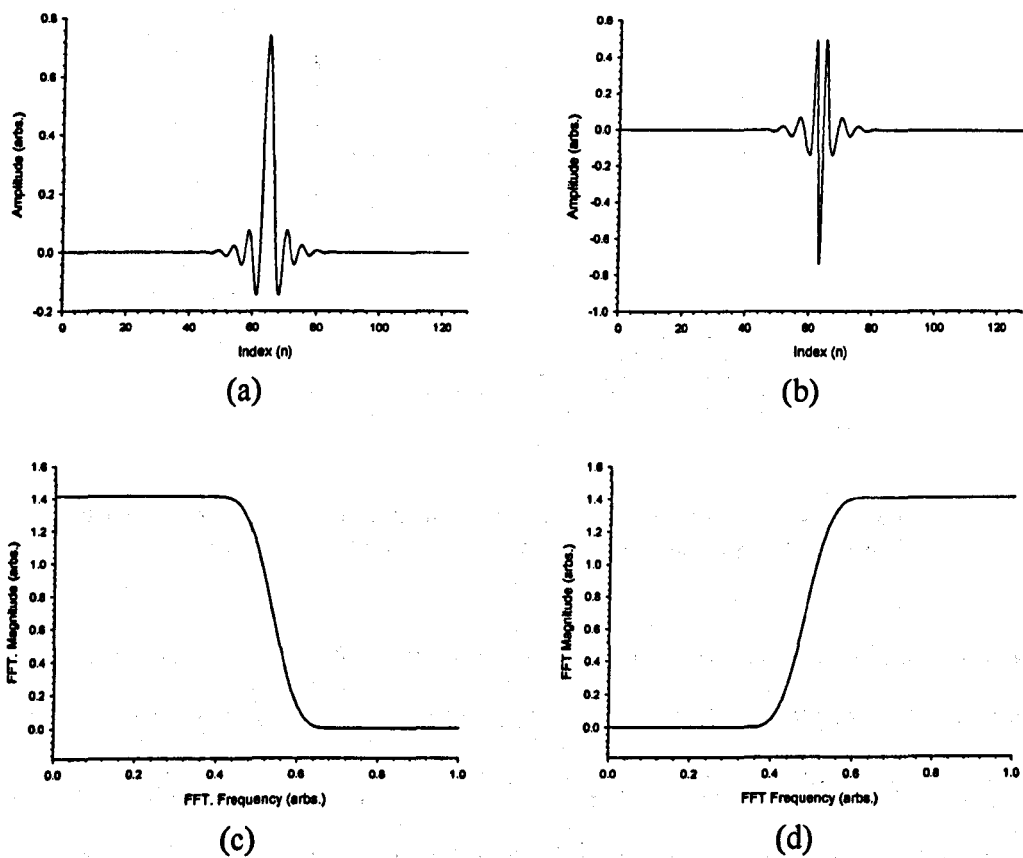


Figure 6.6: The FIR based approximation of the Meyer wavelet, (a) Mother wavelet function, (b) father scaling function, (c) frequency domain characteristic of the Wavelet filter correspondent to (a), and (d) Frequency domain characteristic of the scaling filter correspondent to (b).

The three level up-sampling filter characteristic used in this simulation is shown in Figure 6.7. Figure 6.8 shows the three stage wavelet and scaling decomposition coefficient obtained using Equation (6.7) to (6.14). Wavelet

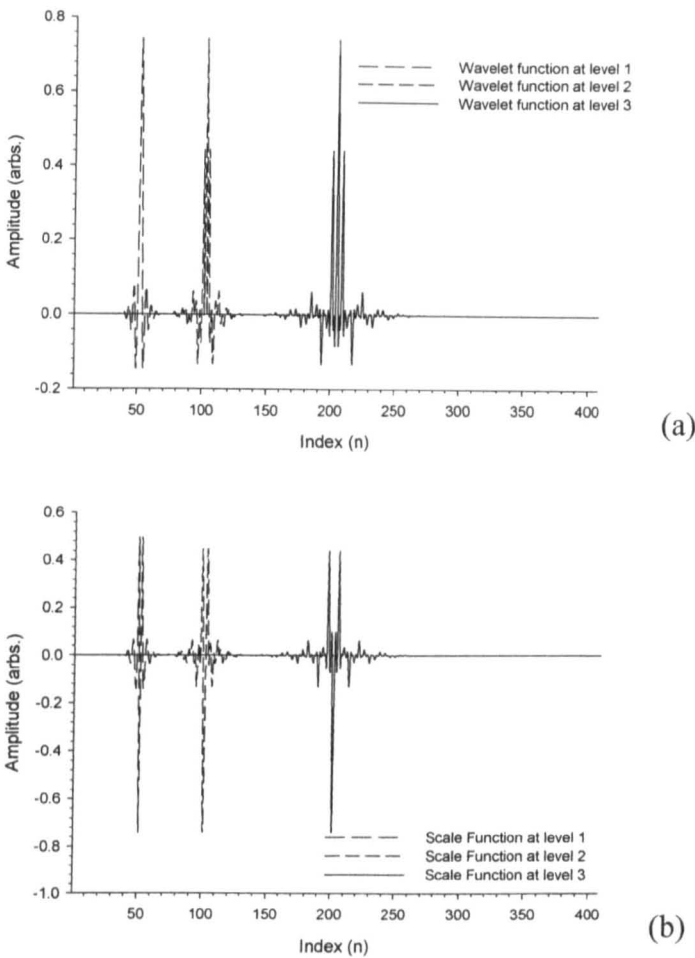


Figure 6.7: The SWT filters characteristics, (a) three levels up-sampling of wavelet function and (b) three levels up-sampling of scaling function.

analysis consisted of decomposing a signal into a hierarchical set of ‘approximations’, cA_j and ‘details’, cD_j , whereas cA_j taking into the account of low frequencies of $f(x)$ and the cD_j , corresponded to the high frequency correction. The selection of a suitable level for the hierarchy will depend on the signal and experience. The reconstruction of the ‘approximations’ and ‘details’ using the inverse SWT is shown in Figure 6.8(c) and Figure 6.8(d). The reconstructed signal associated with A_3 and D_3 yields the reconstruction giving a close resemblance to the actual simulated signal, shown earlier in Figure 6.5(a) and 6.5(b). To produce an accurate synthetic time signal, the criterion used was to select the filter level producing a synthetic time signal that most closely resembled to the actual signal being analysed.

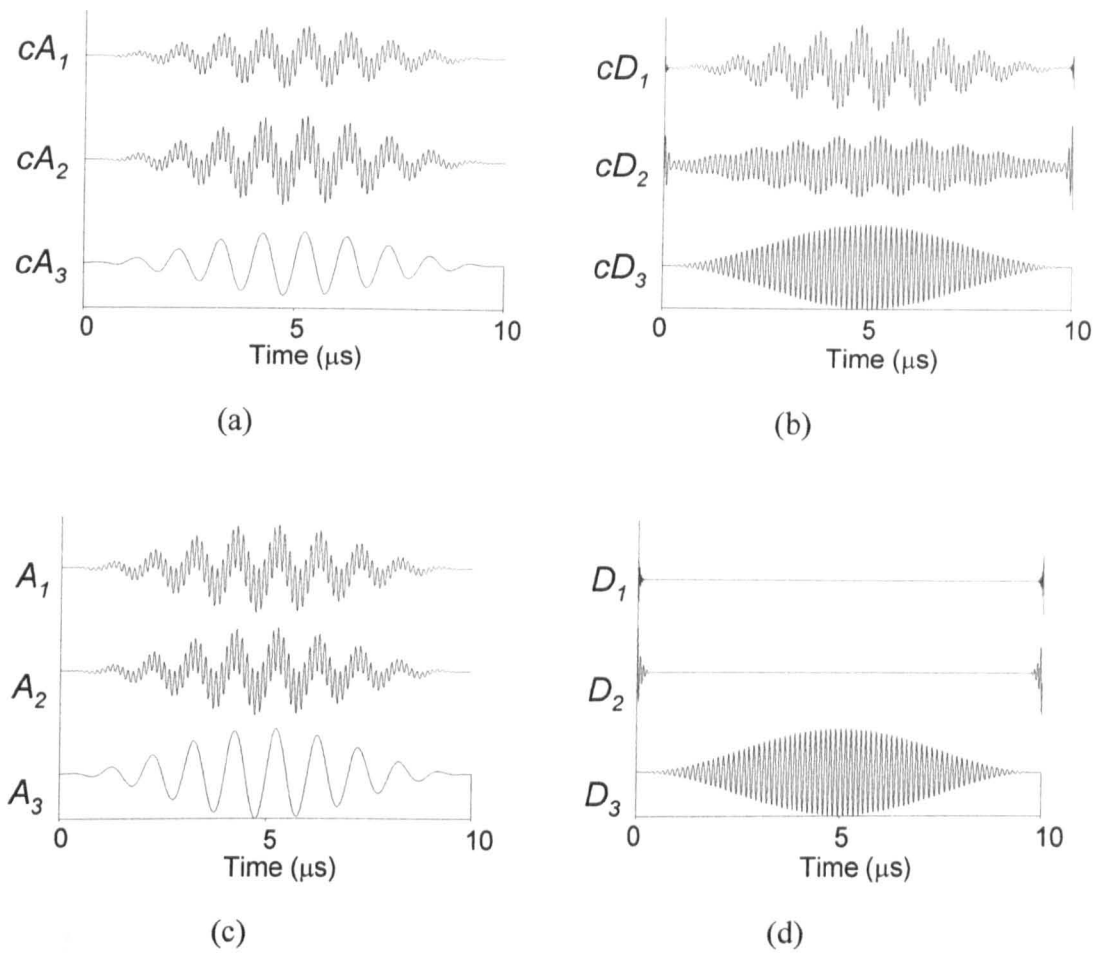


Figure 6.8: Signal decomposition and reconstruction using SWT. (a) Three levels decomposition of approximation coefficients, (b) three levels decomposition of detail coefficients, (c) three levels reconstruction of approximation coefficients, and (d) three levels reconstruction of detail coefficients.

6.5 Preliminary Experiments

Preliminary experiments were conducted to determine the response of the EMAT system used, and to illustrate the modes that would be expected within the received waveform.

6.5.1 Apparatus and Experimental Setup

The EMAT configuration was that shown earlier in Figure 6.2, and used a planar meander-line coil configuration as 6 cycles with the wavelength chosen of approximately 1.8 mm. The EMAT was 8.8 mm long and was 20 mm wide. The EMAT was constructed using fine enamelled copper wire (Maplin) with a

diameter of ~ 0.08 mm. This was measured using digital callipers (Kennedy: 331-206). An Alcomax-3 permanent magnet was used as the bias magnet field for the EMATs. The EMAT coil was placed against the centre of the flat face of a rectangular-shaped magnet to provide a magnetic field primarily in the direction parallel to the meandering coil. The permanent magnet used had a size of 20 mm by 10 mm with a thickness of 5 mm. Each magnet typically had a weight of 0.03 kg and had a maximum flux density (B_r) of ~ 0.3 T. This was measured using a Hall sensor (Honeywell: SS94A2D). The experimental configuration is shown in Figure 6.9.

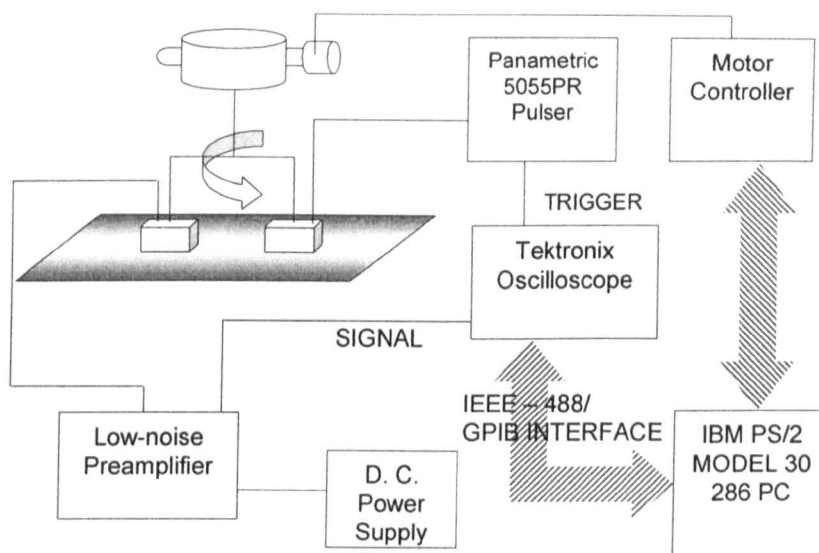


Figure 6.9: Schematic diagram of the experimental arrangement.

Experiments were performed in a pitch-catch arrangement using two similar EMATs. A low carbon-steel plate was used as the sample under test. The steel sheet was 305 mm \times 102 mm, and had a thickness of 0.39 mm. The source EMAT was driven with a -400 V pulse from a Panametric-NDT pulse generator (Model: 5055PR). Lamb waves generated by the EMAT travelled along the plate to the receiver. The transmitted signal was fed to a preamp of approximately 62 dB gain. A second-order Butterworth high pass filter was used to remove some low frequency noise, and the cut-off frequency was chosen at ~ 1 MHz. The time waveform was then recorded on a Tektronix TDS430A digital oscilloscope. The two EMATs were separated by ~ 50 mm from centre-to-centre in the work reported here.

6.5.2 Results and Discussions

An example of the experimental performance of the EMAT system is shown in Figure 6.10, which shows the time signal (Figure 6.10(a)) and the corresponding frequency spectrum (Figure 6.10(b)) for a 0.39 mm thick steel plate. The generation source characteristics are determined by the combination of coil width and proximity of the EMAT coil to the sample, the temporal profile, size of the permanent magnet, and current pulse. The frequency spectrum (Figure 6.10(b)) shows that certain frequency bands are present, which was expected from the Rayleigh-Lamb wave dispersion curve shown in Figure 6.3.

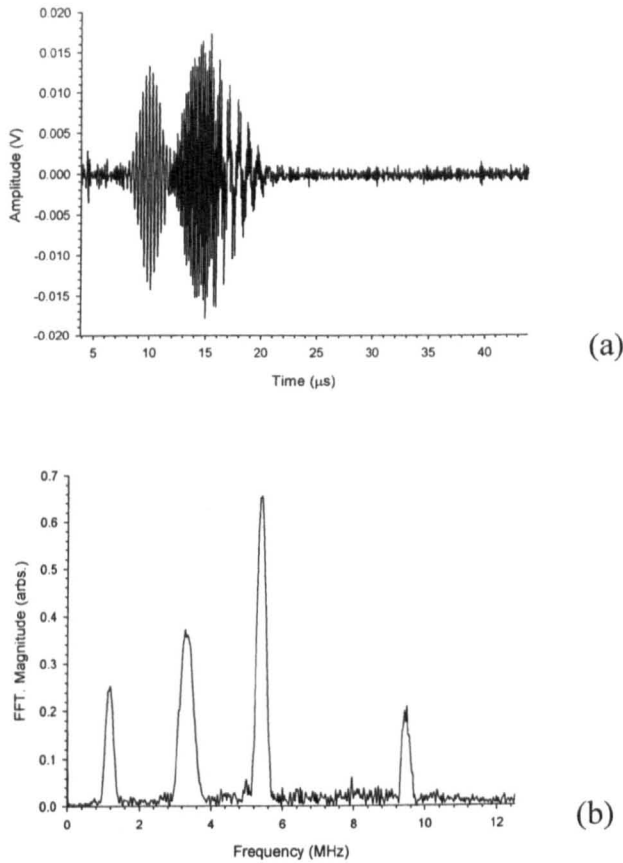


Figure 6.10: Experimental result of the EMAT system, (a) time signal, and (b) frequency spectrum corresponds to (a).

The wave modes generated by the EMAT are relatively narrowband due to the inherently sharp wavelength. The lowest frequency peak corresponded to 1.2 MHz, and the next frequency component is centred at 3.3 MHz. These presumably correspond to the lowest order of Lamb modes, (s_0 and a_0). The

highest amplitude frequency component has a centre frequency peak of 5.4 MHz, and the lowest amplitude component is located at 9.5 MHz. As was predicted in Figure 6.3, these high frequency components correspond to the higher order Lamb wave modes (*i.e.*, a_1 , and s_2). However, the s_1 Lamb component is not present from the captured time signal shown in Figure 6.10(a) and 6.10(b). This is because the calculated phase velocity point (Figure 6.3(a)) corresponds to the 1.8 mm wavelength meander-line EMAT is not exactly interacting to the calculated s_1 group velocity point shown in (Figure 6.3(b)). Hence, the s_1 mode can not be seen in Figure 6.10(a) and 6.10(b).

6.6 Mode identification

6.6.1 Short-Time-Fourier Transform approach

Although these modes can be easily predicted from Figure 6.3, the exact arrival time corresponding to each wave mode is difficult to estimate experimentally. This is due to the modes overlapping in time, as velocities are relatively closed to each other, especially a_0 , a_1 and s_2 in this case. To confirm the prediction seen in Figure 6.10, Short-time Fourier Transform (STFT) signal processing was used to identify this. Mathematically, the STFT is written as:

$$STFT\{x, y\} = X(\tau, \omega) = \int_{-\infty}^{\infty} x(t) w(t - \tau) e^{-j\omega t} dt \quad (6.15)$$

where $w(t)$ is the windowing function, and $x(t)$ is the signal to be transform. $X(\tau, \omega)$ is essentially the Fourier Transform of $x(t)w(t - \tau)$, a complex function representing the phase and magnitude of the signal over time and frequency. In the discrete time case, the data to be transformed could be broken up into chunks which usually overlap each other. Each chunk is Fourier Transformed, and the complex result is added to a matrix (m, ω) , which records magnitude and phase for each point in time and frequency. This can be written as:

$$STFT\{x, y\} = X(m, \omega) = \sum_{n=-\infty}^{\infty} x[n] w[n - m] e^{-j\omega n} \quad (6.16)$$

likewise, with signal $x[n]$ and window $w[n]$. The magnitude squared of the STFT yields the spectrogram of the function:

$$\text{spectrogram}\{x, y\} = |X(\tau, w)|^2 \quad (6.17)$$

6.6.2 STFT Spectrogram

The STFT was used to perform mode identification. The signal to be analysed was the signal shown in Figure 6.10(a). Equations (6.16) and (6.17) were used to calculate the spectrogram. 512 FFT points were used to calculate the discrete Fourier Transforms, and a Hanning window of length 32 units was employed for the windowing function. A maximum sampling frequency of 12.5 MHz was used for scaling. Figure 6.11 shows the time-frequency representation where Figure (6.11(a)) is the captured time waveform shown at the top, with the corresponding frequency spectrum shown to the right (Figure 6.11(b)), and the absolute magnitude of STFT is shown in Figure 6.11(c). The theoretical group velocity dispersion curves for the 0.39 mm thick steel sheet are superimposed on the experimental data in Figure 6.11(c). This shows the group velocity dispersion for the s_0 , a_0 , a_1 , and s_2 multiple Lamb wave modes. The experimental data is consistent with the theoretical predictions in that the data lies on the predicted curves. Note that the s_2 has a very low amplitude compared to a_1 , and it is due to this that the s_2 can not be seen clearly in the contour representation shown in Figure 6.11(c). A 3D mesh plot corresponded to Figure 6.11(c) is shown in Figure 6.11(d) for better visualisation for the identification all multiple modes.

6.7 Demonstration of Multiple Mode Extraction

6.7.1 Stationary Wavelet Processing Approach

Multiple mode extraction was carried out using SWT signal processing technique. The signal $f(x)$ shown in Figure 6.10(a) was used as an input to the SWT decomposition using hierarchical steps (levels) of different resolutions.

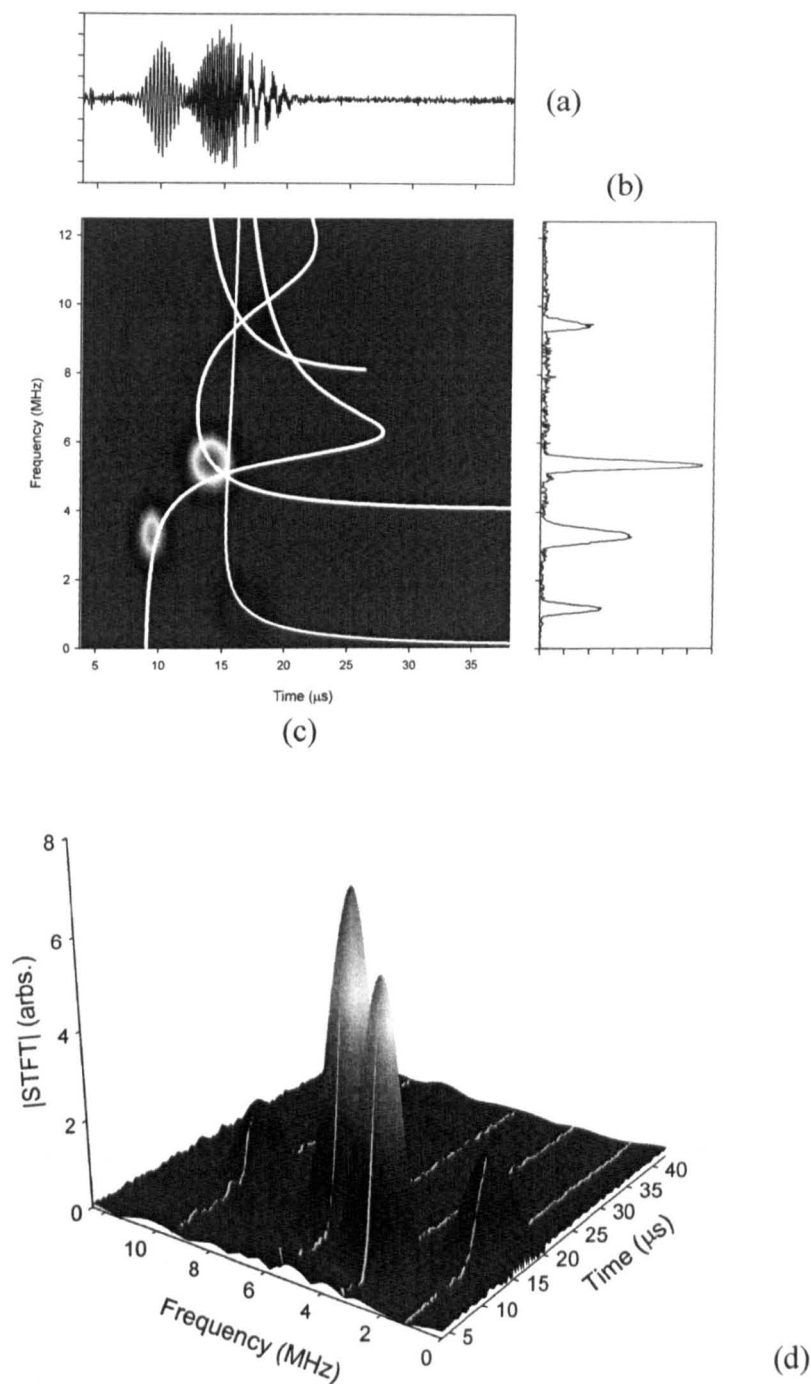


Figure 6.11: Mode identification using STFT, (a) Time signal used for the input of STFT, (b) the frequency spectrum corresponds to (b), (c) the resulted spectrogram using STFT corresponding to (a), and (d) 3D mesh plot of (c).

This was performed using Equation (6.7) with each daughter wavelet corresponding to the time behaviour of the signal in a frequency band. In order to avoid burdensome computational effort, the signal, $f(x)$ is zero padded to a

number of sample points equal to 1024. This is due to the specific implementation adopted for the SWT.

The wavelet and scaling function used were the *FIR* based approximation of the Meyer wavelet as shown in Figure 6.7(a) and Figure 6.7(b). At the first step the function $f(x)$ was decomposed into wavelet coefficients, and the low-frequency components (low-pass filtering) and high-frequency components (high-pass filtering) of $f(x)$ are retained up to level 3. This was performed using Equations (6.9) and (6.10). The signal $f(x)$ is therefore decomposed into separate frequency bands (scales). The filtering outputs were then up-sampled, using Equation (6.11) and (6.12). The number of wavelet coefficients for each branch is thus retained to the total number of points given from that of the original signal.

Next, the process of reconstructing the time signal from these calculated wavelet coefficients was performed. The *approximation* obtained at level 3 is the lowest order component, and it is likely to correspond to the a_0 mode. Figure 6.12(a) shows the synthetic time signal performed after SWT signal processing (solid line), and before SWT signal processing (dotted line). This extraction was confirmed by performing Fast Fourier Transform (*FFT*) spectrum analysis of the synthetic time signal obtained in Figure 6.12(a). Figure 6.12(b) shows the frequency spectrum after SWT signal processing (solid line), and the frequency spectrum of the original signal (dotted line). As can be seen, the signal which was extracted corresponds to the a_0 mode, and the interference of higher-frequency components is completely separated.

6.7.2 Wavelet Binary Tree Approach

This process was repeated in a pyramidal manner, and the exact procedure is shown schematically in Figure 6.13. This wavelet decomposition tree approach can be used for numerous expansions of a given signal, *i.e.* the original signal $f(x)$ is split up into *approximation* coefficients and *detail* coefficients, and the information lost between the two successive approximations is captured in the detail coefficients. The next step consists of splitting the new *approximation* coefficients and *detail* coefficients until the

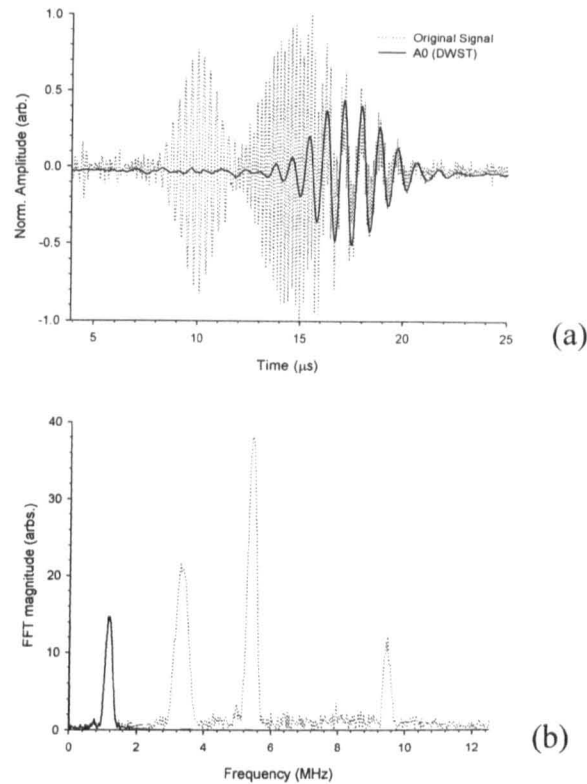


Figure 6.12: Mode extraction using SWT, (a) the synthetic time signal of the approximation coefficients at level 3, (b) the corresponding frequency spectrum of (a).

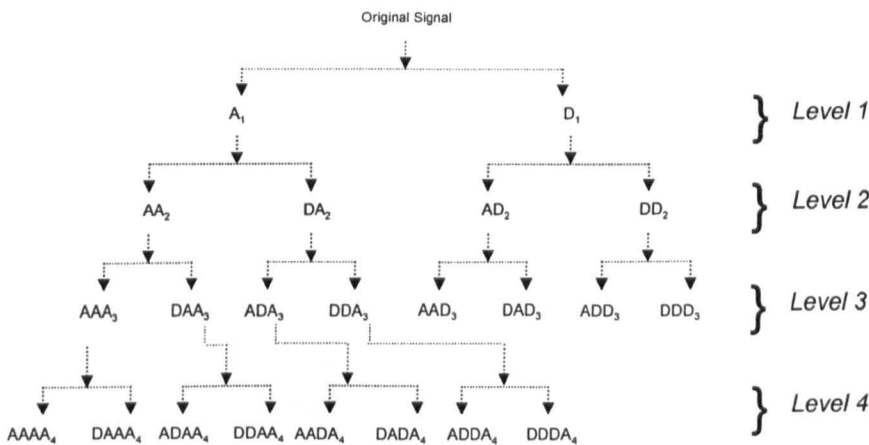


Figure 6.13: Schematic diagram of the binary tree SWT structure.

desired information is achieved. This complete binary tree can produce the richest analysis for the extraction of a desired wave mode. By using this wavelet binary tree procedure, the extraction of a_0 is obtained at AAA_3 , s_2 is obtained at DD_2 , a_1 is obtained at $DDDA_4$ and s_0 is obtained at $AADA_4$.

Figure 6.14 shows the extracted modes using the wavelet binary tree approach. Figure 6.14(a) shows the synthetic time signal corresponding to the s_0 mode, Figure 6.14(b) is the corresponding frequency spectrum of Figure 6.14(a), Figure 6.14(c) is the synthetic time signal corresponded to the a_1 mode, Figure 6.14(d) is the corresponding frequency spectrum of Figure 6.14(c), and

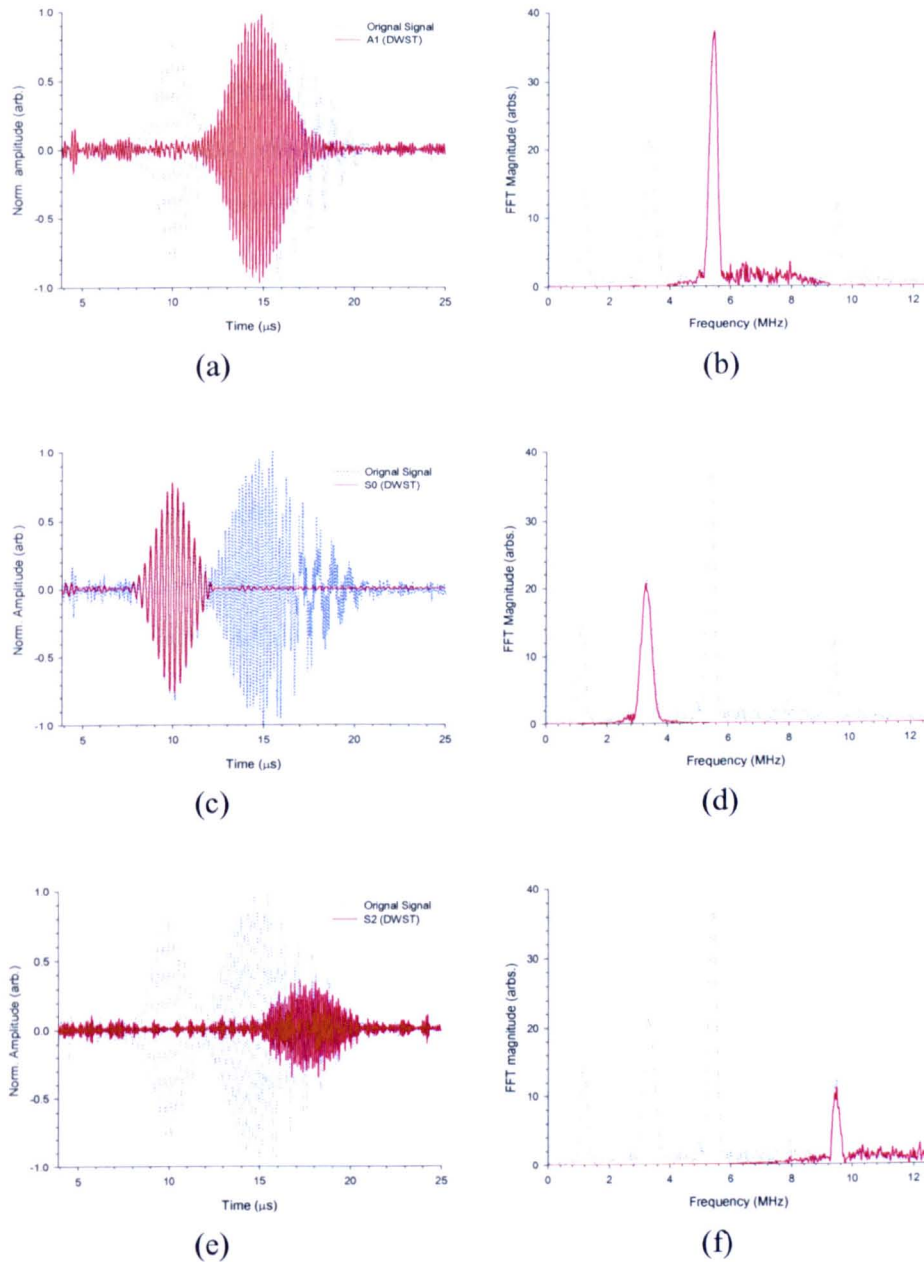


Figure 6.14: Mode extraction using the binary tree SWT, (a) the synthetic time signal obtained at AADA4, (b) the corresponding frequency spectrum of (a), (c) the synthetic time signal obtained at DDDA4, (d) the corresponding frequency spectrum of (c), (e) the synthetic time signal obtained at DD2, (f) the corresponding frequency spectrum of (e).

Figure 6.14(e) shows the synthetic time signal corresponding to the s_2 mode, Figure 6.14(f) is the corresponding frequency spectrum of Figure 6.14(e).

As was shown in Figure 6.12 and Figure 6.14, the identified modes from the experimental signal shown in Figure 6.11 using the STFT approach are extracted. This means the precise cut-off frequencies and bandwidths associated with each wave mode are ascertained. This was obtained by dividing them out via QMF pairs filtering, and therefore the wave mode can be captured and implemented separately for application where wave mode optimisation is considered to be important. It should be pointed out that this technique can be used for mode extraction under highly-noisy environment, where any unwanted noise can be removed, and it is thus allowing a dramatic improvement in the acquisition speed without the need of signal averaging.

6.8 Degree of Dispersion Considerations

6.8.1 Mode Analysis using FFT

Since no plate is infinitesimally thick, wave propagation in a plate is always dispersive. Thus, the selection of wave mode must be carefully chosen if quantitative values of the texture parameters are to be obtained. Therefore the degree of dispersion of wave propagation should be estimated or resolved before proceeding to the details of the texture experimental analysis. An experiment was first performed to verify the dispersion effect using a range of different thickness specimens. A set of experiments was carried out using the apparatus as shown in Figure 6.9. The same sample of different thickness sheets 0.05 - 0.39 mm were used. Figure 6.15 shows the transmission and reception of Lamb waves using 1.8 mm wavelength EMATs on different thickness of steel sheets.

Figure 6.15(a) shows a waterfall plot which was created using the received time signals and (b) shows the corresponding frequency spectrum of (a). The 0.39 mm received time signal is the same as shown in Figure 6.10(a), and consists of the four order modes expected and identified in Figure 6.11. As the thickness decreases, the modes attenuate and velocities changes dramatically

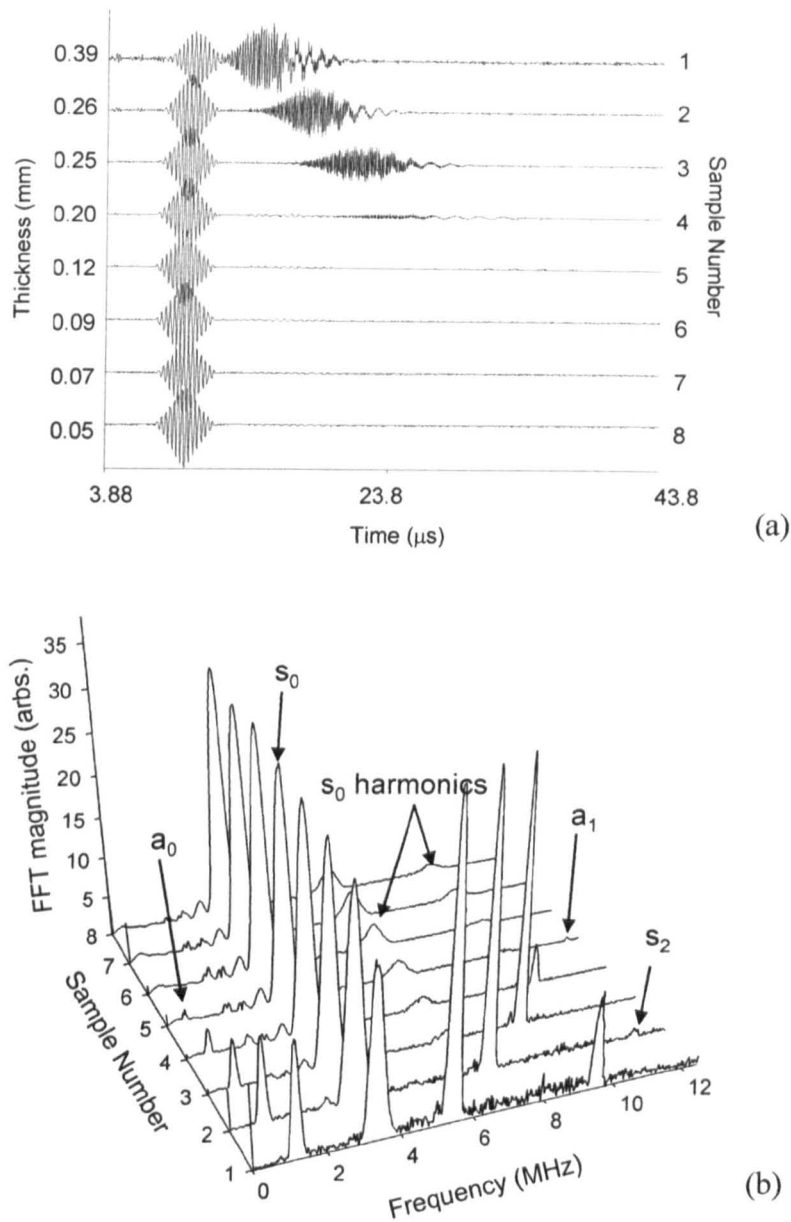


Figure 6.15: Experimental results obtained using various of different steel sheet thickness, (a) waterfall-plot of the time received signals, (b) the corresponding frequency spectrum of (a).

except for the s_0 fundamental mode. The attenuation of the s_0 mode has the opposite behaviour pattern compared to a_0 , a_1 and s_2 modes. The s_2 mode attenuated to its maximum at 0.26 mm thick plate, and the maximum a_0 and a_1 mode attenuation both occur in the 0.12 mm thick plate. The change of peak frequency for a_1 and s_2 against the change in thickness are large compare to a_0 , and the s_0 mode has its minimum peak frequency changed. As the thickness increases, the peak frequency increases for the fundamental s_0 and a_0 modes,

and the peak frequency decreases for the higher-frequency Lamb modes, *i.e.* the a_1 and s_2 modes. Also note that the 0.05 to 0.25 mm plates show a harmonic series of s_0 modes. It has a fundamental frequency (first harmonic), f of 3.4 MHz, second harmonic, $2f$ of 6.8 MHz and a third harmonic, $3f$ of 10.1 MHz.

6.8.2 Mode Velocity Analysis

The mode velocities shown in Figure 6.15 for all plates were extracted using SWT, and the values (shown in dots) were plotted and shown in Figure 6.16. The extracted values are plotted on the y-axis and the corresponding frequency \times thickness ($f \times d$) is plotted on the x-axis. The theoretical group velocity calculation of the dispersion wave modes is fitted to the experimental extracted data.

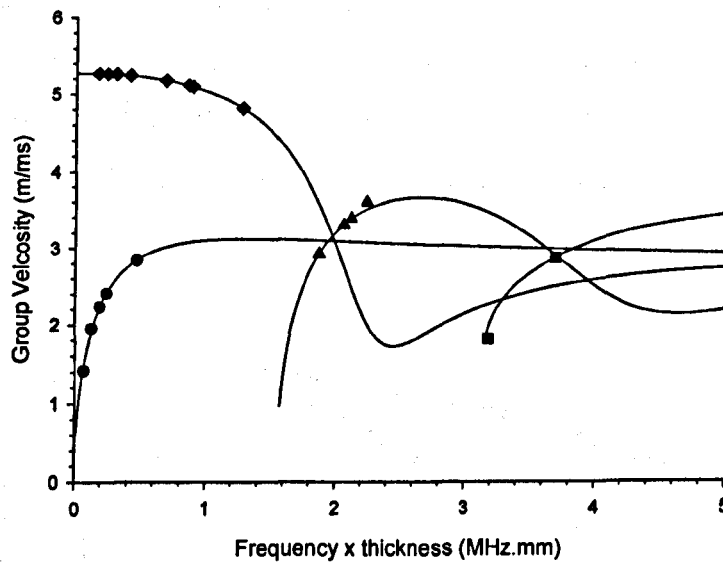


Figure 6.16: Modes extraction using SWT at a range of different thickness. The solid-lines show the Rayleigh-Lamb dispersion curves of 1 mm thick steel, the dotted points show the time extracted results obtained from Figure 6.15(a).

As can be seen, the experimental data lies on the predicted curves. The tests are in good agreement with those predicted theoretically. For the dispersion curves shown in Figure 6.16, the larger slope of the curve means higher dispersion, and the smaller slope (or flat region) of the dispersion curve represents little dispersion (or the non-dispersive region). As can be seen in

Figure 6.16, the s_0 lie in the non-dispersive region for small thickness sheets, and the reason for this is that the s_0 velocities and the peak frequency shown in Figure 6.15 have the least effect on the different thicknesses. The a_0 changes from high dispersion to lower dispersion as the thickness increases, and has the lowest excitation frequency required compare to s_0 , a_1 and s_2 . The a_1 and s_2 are both dispersive and required higher frequencies of excitation compared to the fundamental a_0 and s_0 modes.

6.9 Texture Measurements

6.9.1 Dispersion Effect Estimation in Thin Plates

The influence of dispersion on the velocity measurements is important. This is due to the fact that both the phase and the group velocity are frequency dependent. The propagation of an s_0 mode using the 0.05 mm thick steel sheet is first measured for ideal measurements of phase velocity, and this serves as an exact reference solution to the measurements made on 0.39 mm thick sample. The phase velocity (V_p) and group velocity (V_g) have been calculated for 1 mm steel sheet up to a frequency-thickness of 1 MHz.mm as shown in Figure 6.17.

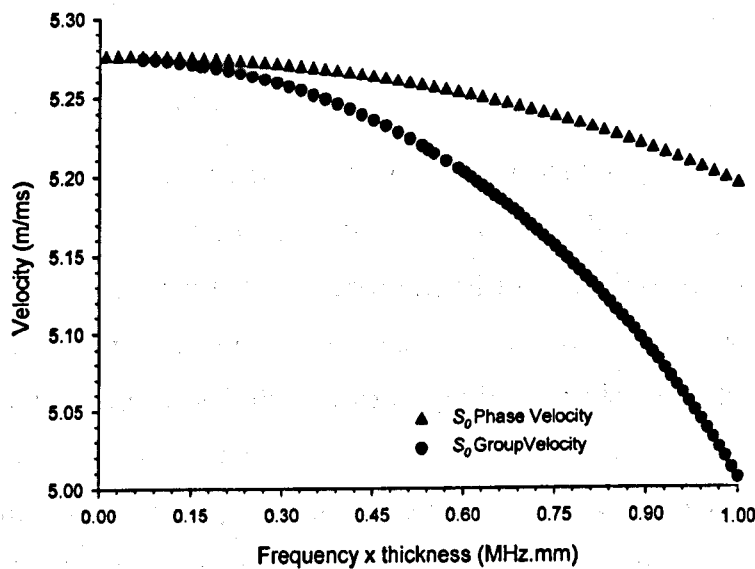


Figure 6.17: Phase and Group velocity dispersion curves simulated up to 1 MHz of 1 mm thick steel.

Note that the frequency-thickness product present for 0.05 mm experiment is less than 0.17 MHz.mm, and there would be a variation of less than 0.1% in the group velocity, and thus dispersion effects are negligible in this case.

6.9.2 Texture Experiments and Apparatus

Measurements were performed using the same specimens as described previously in Figure 6.15. The 0.05 and 0.39 mm nominal thickness samples were chosen to demonstrate the ability to extract the information required to evaluate the texture characteristics using different modes. A schematic diagram of the experimental set-up is shown in Figure 6.9. The measurements were carried out under standard laboratory conditions. The EMAT transducers were set close together to minimise the pulse distortion phenomenon effect, *i.e.* a pulse of dispersive wave changes its shape and spreads out as it propagated. A distance of 50 mm was chosen, and the transducers were fixed on either end of a rotating arm driven by a stepper motor. The stand-off distance between the EMATs and the sheet sample was approximately 0.3 mm. A PC was used to control the stepper motor that drove the EMATs rotationally and the same PC was used to capture and process the ultrasonic data. The EMATs were scanned around one complete revolution with 1° step size, and SWT was used to extract the velocities as a function of angle to the rolling direction.

6.9.3 Velocity Measurements On Thin Plate

The transit time measurement for the s_0 mode propagates as a function of angle to the rolling direction for the 0.05 mm is shown in Figure 6.18. The polar plot is used to illustrate the measured arrival time against the corresponding angular axis. The results for the 0.05 mm thick sheet, as can be seen in Figure 6.18, show the expected form of anisotropy in acoustic velocity. The fastest directions for the s_0 mode on the 0.05 mm thick sheet (Figure 6.18) occurs perpendicular to the rolling direction and are nominally identical. The slowest directions for the s_0 mode occur at $\sim 30^\circ$ to the rolling direction. The velocity along the rolling direction was taken to be equal to 5208 ms^{-1} , and this corresponds to an uncertainty of $\pm 62 \text{ ms}^{-1}$ compared to the theoretical value

obtained using the Rayleigh-Lamb frequency relations. The magnitude of the anisotropy *i.e.* the fractional arrival time differences are observed approximately on the order of 0.6 μs . This corresponds to a $\sim 6.5\%$ variation in V_g for the 0.05 mm thick sheet. With this degree of variation, it is likely to observe some beam steering effects in the experimental measurement.

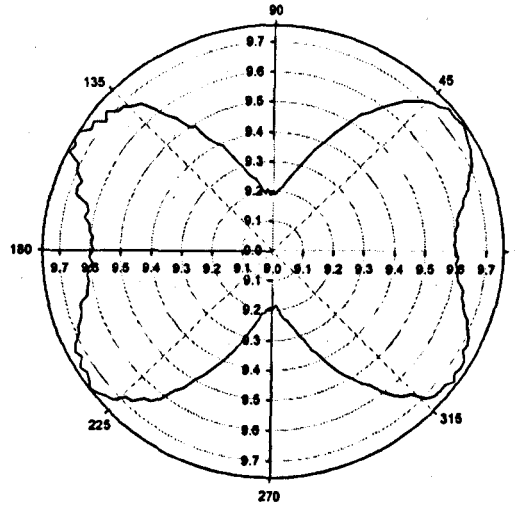


Figure 6.18: The s_0 mode transit time (μs) texture result on the 0.05 mm thick steel sheet as a function of angle to rolling direction.

6.9.4 Orientation Distribution Coefficients Extraction

The theory shown in Equations (6.3) to (6.5) is used to relate the aforementioned ODCs of textured sheets to the wave propagations in three different directions (0° , 45° , and 90°) with respect to the rolling direction. This theory assumes the ratio of sheet thickness to wavelength to be small, and this is satisfied for the s_0 experimental data obtained using the 0.05 mm thick steel sheet. In the case where the wavelength of the s_0 is large compared to the sheet thickness, the s_0 mode can be considered to be effectively non-dispersive as shown in Figure 6.18. The calculated values of the ODCs obtained by using three velocity values at 0° , 45° and 90° for the 0.05mm sheet using the s_0 is shown in Table 6.1. Fits were made to the results shown in Table 6.1 using Equation (6.2) for the full range of angles, 0-360°, and this is shown in Figure 6.18. The solid-line shows the experimental results, and the fitted curve is shown using the dashed-line. Figure 6.19 shows reasonable agreement between the experimental and theoretical curve.

		sheet thickness (mm)	W_{400}	W_{420}	W_{440}
Mode					
From 3 points	s_0	0.05	0.01342	0.00452	0.00452
From curve fit	s_0	0.05	0.01380	0.00473	0.00447
From 3 points	s_0	0.39	0.00971	0.00334	0.00420
From curve fit	s_0	0.39	0.00984	0.00340	0.00396
From 3 points	s_0	0.39	-0.09459	0.00021	0.00081
From curve fit	s_0	0.39	-0.09476	0.00021	0.00079
From 3 points	a_1	0.39	-0.07696	-0.00056	0.00052
From curve fit	a_1	0.39	-0.07716	-0.00055	0.00051

Table 6.1: Calculated values of the ODCs obtained by using three velocity values at 0°, 45°, and 90°, and the theoretical fitting to Equation (6.2).

The accuracy in the coefficient values obtained from the curve fit is estimated to be $\pm 5\%$, and the largest error obtained from using just three velocity values occurred at W_{420} . The difference is probably due to the experimental error. Fitting the entire range of data to the function gives a more reliable measurement of the ODCs, but obtaining the data obviously requires more time. Hence the three velocities approach is suitable where speed is crucial, but the curve fit can be used to reduce measurement error.

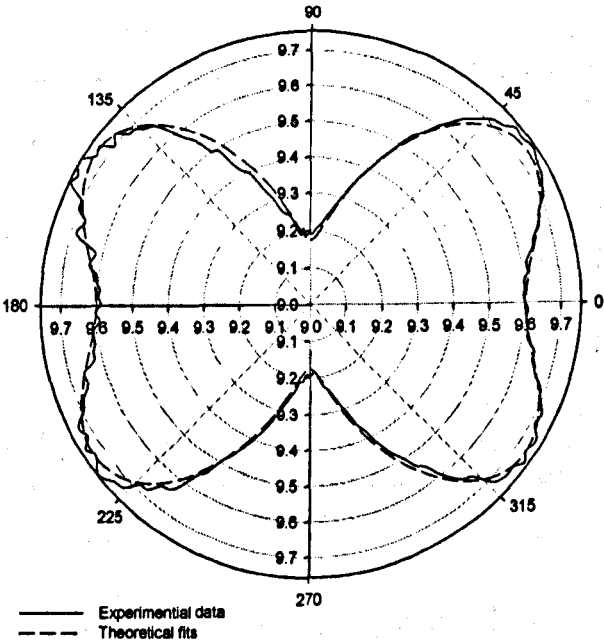


Figure 6.19: The s_0 transit time (μs) together with a “theoretical fit” on the 0.05 mm thick steel sheet.

6.9.5 Amplitude Measurements on Thin Plate

Figure 6.20 shows the directionality using the amplitudes for the s_0 mode measured as a function of angle to the rolling direction for the 0.05 mm thick sample.

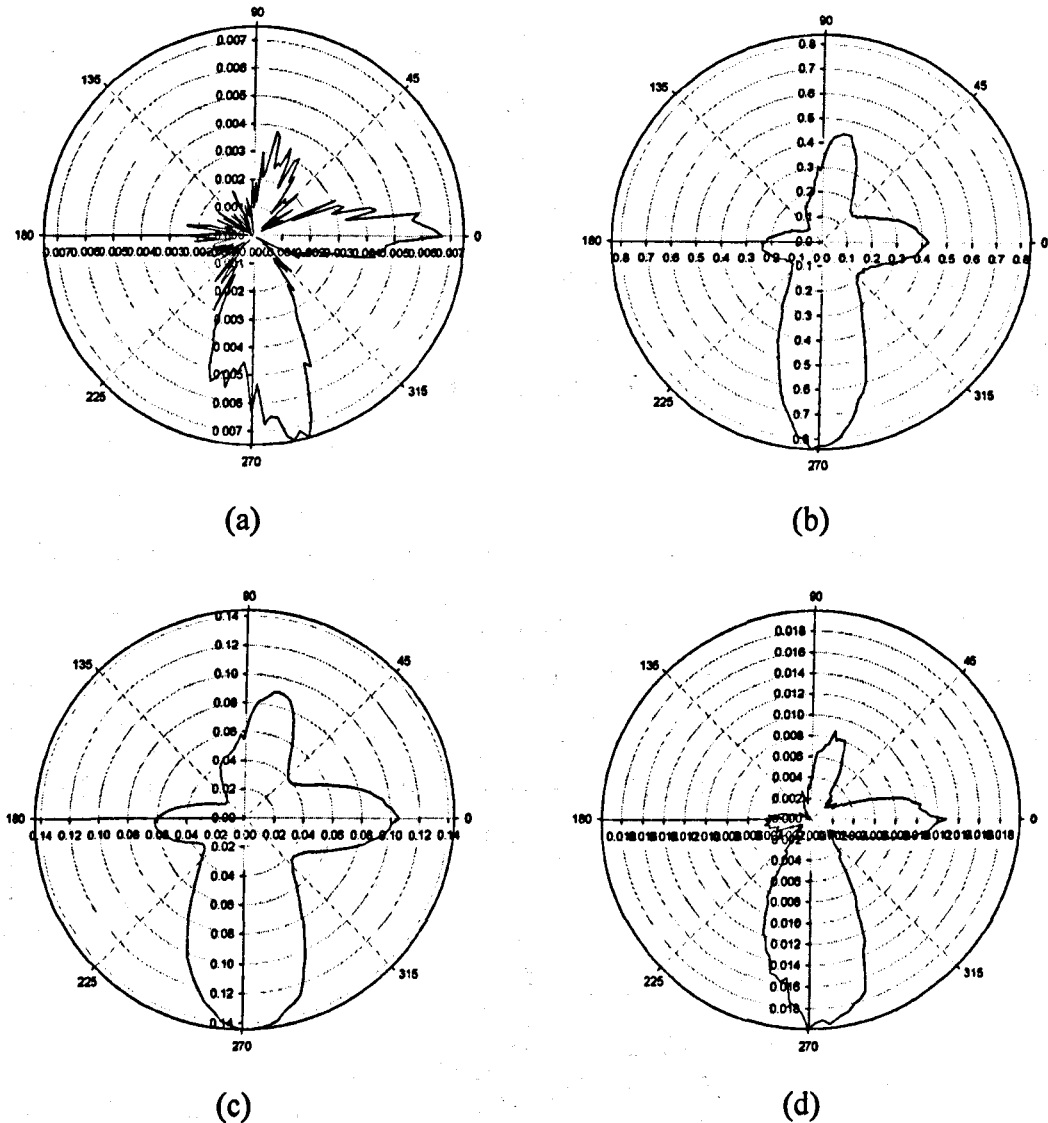


Figure 6.20: s_0 directivity on 0.05mm thick steel, the scales are shown in arbitrary scales, (a) amplitude peak-to-peak, (b) FFT magnitude of the fundamental frequency, (c) FFT magnitude of the second harmonic, and (d) FFT magnitude of the third harmonic.

The obtained results are shown using polar plots, and the amplitude is shown as an arbitrary scale. Figure 6.20(a) shows the peak-to-peak amplitude with respect to the angular position, Figure 6.20(b) shows the frequency magnitude obtained via FFT corresponding to the fundamental frequency f with respect to the angular position, Figure 6.20(c) shows the frequency magnitude

corresponding to the second multiple harmonic $2f$, and Figure 6.20(d) shows the frequency magnitude corresponding to the third multiple harmonic $3f$. The directivity between the amplitude and the frequency spectrums obtained using the s_0 mode shown in Figure 6.20 have very similar characteristics. As can be seen, the directivity pattern has the maximum attenuation occurring at approximately 45° , 135° , 225° , and 315° . This has resulted in four distinct peaks at an approximate angle of 0° , 80° , 180° , and 270° with respect to the rolling direction. The angle range approximately from 225° to 315° has the largest beam-lobe. It has the widest beam width and has the highest amplitude. The smallest beam-lobe is found approximately at 135° to 225° with respect to the rolling direction. The s_0 amplitude shown in Figure 6.20(a), and the harmonic series shown in Figure 6.20(b) to Figure 6.20(d) corresponding to Figure 6.20(a) shown to have a similar trend.

6.9.6 Texture Measurements on a Thick Plate using the s_0 mode

The measurements of the s_0 velocities on the 0.39 mm sheets were compared with to the values obtained on the 0.05 mm thick sheet. The s_0 mode used in this texture experiment has higher-dispersive characteristics than the one used for 0.05 mm, and this is seen experimentally in Figure 6.18. The measured arrival time for the s_0 mode obtained using the 0.39 mm thick sample is shown in Figure 6.21.

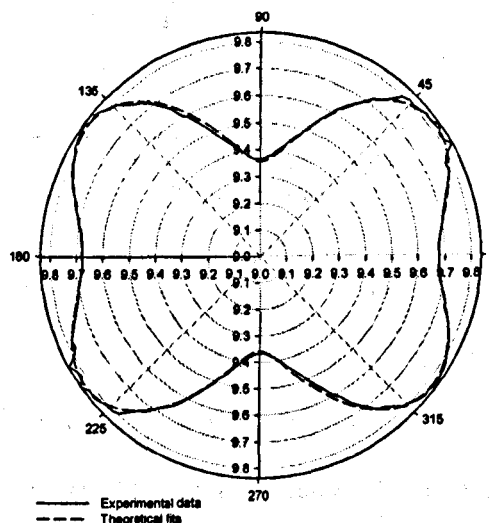


Figure 6.21: s_0 mode texture result on the 0.39 mm thick steel sheet as a function of angle to rolling direction. The experimental transit time (μs) together with a theoretical fit.

The fastest direction for the s_0 mode in the 0.05 mm thick sheet (Figure 6.21) occurs perpendicular to the rolling direction and is nominally identical. The slowest directions for the s_0 mode occur at $\sim 40^\circ$ to the rolling direction. This has shown a similar pattern compared to Figure 6.19(a). The magnitude of the anisotropy (*i.e.* the fractional arrival time differences) is approximately of 0.5 μs . This corresponds to a $\sim 5.3\%$ variation in V_g for the 0.39 mm thick sheet.

The calculated values of the ODCs obtained by using three velocity values at 0° , 45° and 90° for the 0.05 mm sheet using the s_0 is shown in Table 6.1. Fits were made to the results shown in Table 6.1 using Equation (6.3) to (6.5) for the full range of angles, 0 - 360° , and this is shown in Figure 6.21. The solid-line shows the experimental results, and the fitted curve is shown using a dashed-line. Figure 6.21 shows good agreement between the experimental and theoretical curve. However, it has a large error for the W_{420} coefficient. The two measured angular dependent s_0 velocity curves are shown, the error introduced by the dispersion is illustrated in Figure 6.22.

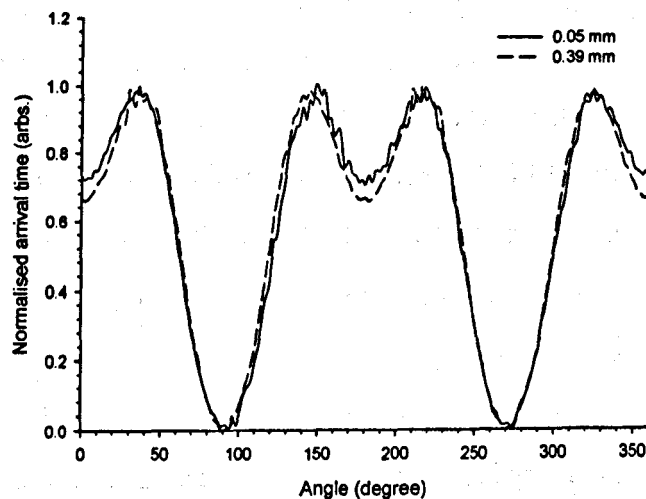


Figure 6.22: Normalised s_0 transit time on 0.05 mm (solid line) and s_0 transit time on 0.39 mm (dashed line).

Note the arrival time for the 0.05 and 0.39 mm thick specimens correspond to the frequency-thickness products of $\sim 0.15 \text{ MHz}\times\text{mm}$ and $\sim 1.17 \text{ MHz}\times\text{mm}$ respectively obtained using the s_0 mode have been normalised for easy comparison. The solid-line shows the 0.39 mm thick experimental data,

and the 0.05 mm is shown using the dashed-line. Note that there is no observable difference between the curves perpendicular to the rolling direction, but velocity differences appear along or at angles close to the rolling direction. The dispersion effect in this case has caused the measured velocity to be apparently lower. The normalised curves have shown there is no difference between the normalised velocities perpendicular to the rolling direction for the two cases, and based on this experimental evidence, the effect of dispersion has negligible effects on the propagation velocity of the s_0 mode.

6.9.7 Texture Measurements on a Thick Plate using the a_0 Mode

The measurement of the a_0 velocities are compared relative to the s_0 values obtained for the 0.39 mm thick sheet. The a_0 used has a frequency-thickness product (MHz×mm) of ~ 0.47 . The measured arrival time (solid-line) for the a_0 mode obtained using the 0.39 mm thick sample is shown in Figure 6.23. An experimental fit was made to the measured results using Equation (6.2), and this is plotted and shown as a dashed-line. The two fastest directions for the a_0 mode in the 0.39 mm thick sheet (Figure 6.23) occur along and perpendicular to the rolling direction and are nominally identical. The slowest directions for the s_0 mode occur at $\sim 40^\circ$ to the rolling direction. The fractional arrival time differences are observed approximately of the order of 0.4 μs . This corresponds to a $\sim 2.3\%$ variation in V_g for the 0.39 mm thick sheet.

The calculated values of the ODCs obtained by using three velocity values at 0° , 45° and 90° and the theoretical fit for the 0.39 mm sheet using the a_0 are shown in Table 6.1. Figure 6.24 shows the angular dependent arrival time for the s_0 and a_0 modes measurement performed using the 0.39 mm thick sheet. Note the arrival time for both modes are normalised for easy comparison. The effects on the arrival time are generally similar, *i.e.* the fastest velocities occur at the direction perpendicular to the rolling direction and are nominally identical, but the velocity along or at angles close to the rolling direction is noticeably different. The s_0 and a_0 velocities correspond to the rolling direction has a difference of $\sim 40\%$. Therefore, the a_0 has produced sharper changes of velocity corresponding to the angles range between the rolling and the perpendicular directions when it is compared to the s_0 mode.

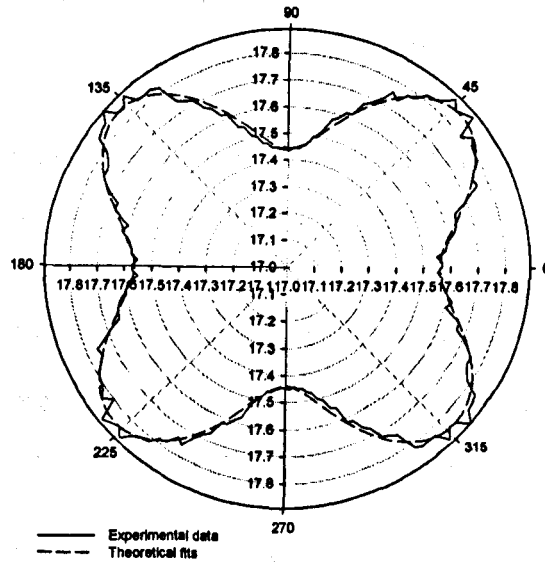


Figure 6.23: a_0 transit time (μs) mode texture result on the 0.39 mm thick steel sheet as a function of angle to rolling direction, with a “theoretical fit”.

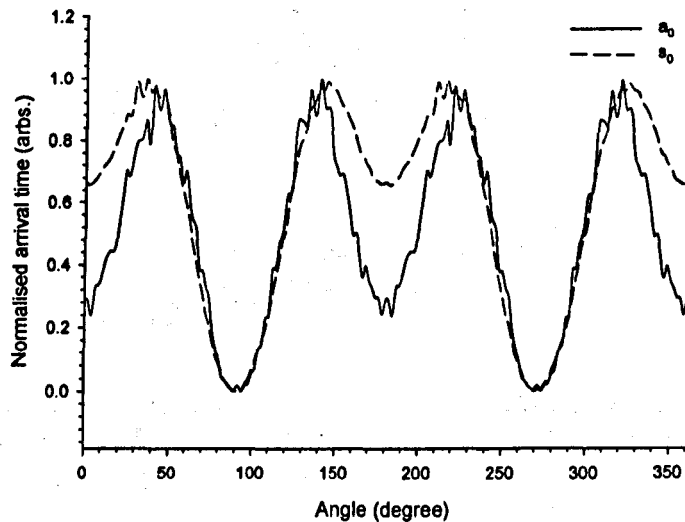


Figure 6.24: Normalised a_0 transit time on 0.39 mm (solid line) and s_0 transit time on 0.39 mm (dashed line).

6.9.8 Texture Measurements on a Thick Plate using the a_1 Mode

The measurement of the a_1 velocities are compared relative to the s_0 values obtained for the 0.39 mm thick sheet. The a_1 used has a frequency-thickness product (MHz \times mm) of ~ 2.1 . The measured arrival time (solid-line) for the a_1 mode obtained using the 0.39 mm thick sample is shown in Figure

6.25. An experimental fit was made to the measured results using Equation (6.2), and this is plotted and shown as a dashed-line. The fastest directions for the a_1 mode in the 0.39 mm thick sheet (Figure 6.25) occur along to the rolling direction and are nominally identical. The slowest directions for the a_1 mode occur at $\sim 50^\circ$ to the rolling direction. The fractional arrival time differences are observed approximately in the order of $0.25 \mu\text{s}$. This corresponds to a 1.7% variation in V_g for the 0.39 mm thick sheet. The calculated values of the ODCs obtained by using three velocity values at 0° , 45° and 90° and the theoretical fit for the 0.39 mm sheet using the a_1 are shown in Table 6.1.

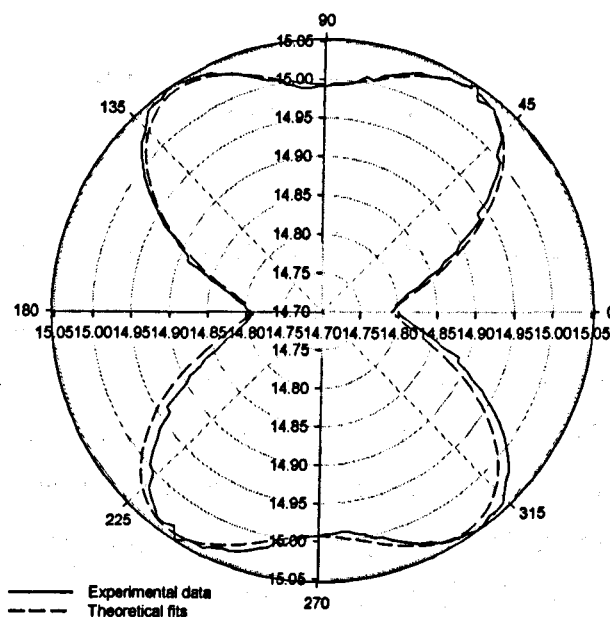


Figure 6.25: a_1 mode transit time (μs) texture result on the 0.39 mm thick steel sheet as a function of angle to rolling direction, with a "theoretical fit".

Figure 6.26 shows the angular dependent arrival time for the s_0 and a_1 modes measurement performed using the 0.39 mm thick sheet. Note the arrival time for both modes are normalised for ease of comparison. As it can be seen in Figure 6.26, the a_1 has an angular dependent arrival time pattern similar to the results obtained by using the s_0 , with the angular axis shifted by $\pm 90^\circ$. In other words, the fastest direction for the a_1 mode is located along the rolling direction, where the s_0 mode has the fastest direction perpendicular to the rolling direction. The rolling direction corresponds to the s_0 mode and the perpendicular direction corresponds to the a_1 mode has a velocity difference of $\sim 70\%$.

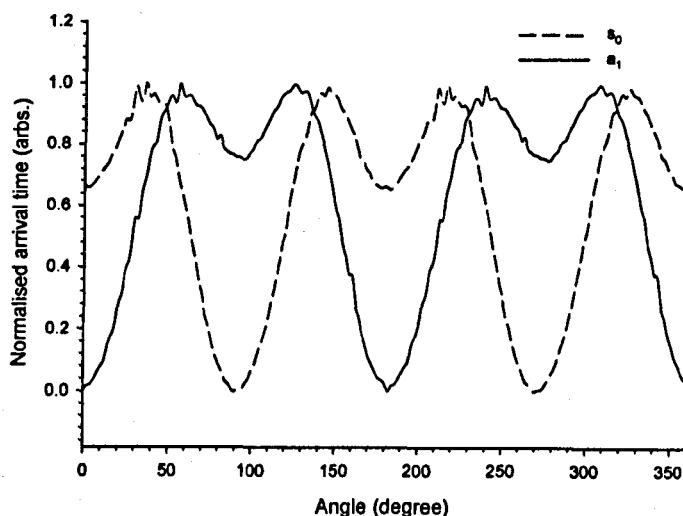


Figure 6.26: Normalised a_1 transit time on 0.39 mm (solid line) and s_0 transit time on 0.39 mm (dashed line).

6.9.9 Amplitude Comparison of Multiple Modes on Thick Plate

Figure 6.26 shows the directionality using the peak-to-peak amplitude, measured as a function of angle to the rolling direction for the 0.39 mm thick sample. The results are represented using a polar plot, and the amplitude is shown in an arbitrary scale. Figure 6.26 shows the peak-to-peak amplitude with respect to the angular position of (a) the, s_0 mode, (b) the a_0 mode, (c) the a_1 mode, and (d) the s_2 mode. As can be seen, the directivity plots corresponding to a_0 , s_0 , a_1 and s_2 modes for the 0.39 mm thick specimen shown in Figure 6.26 have similar amplitude patterns. It is interesting to note that the s_0 beam-lobes observed in Figure 6.19(a) have become significantly narrower as shown in Figure 6.26(a). This is especially true for the directivity beam-lobe corresponding to the angle range between 225° and 315° with respect to the rolling direction. Also note that for the s_0 directivity beam-lobe corresponds to the angle range between 45° and 125° shown in Figure 6.26(a) has the maximum amplitude exactly at 90° , but the one shown in Figure 6.19(a) has the maximum amplitude approximately at 80° .

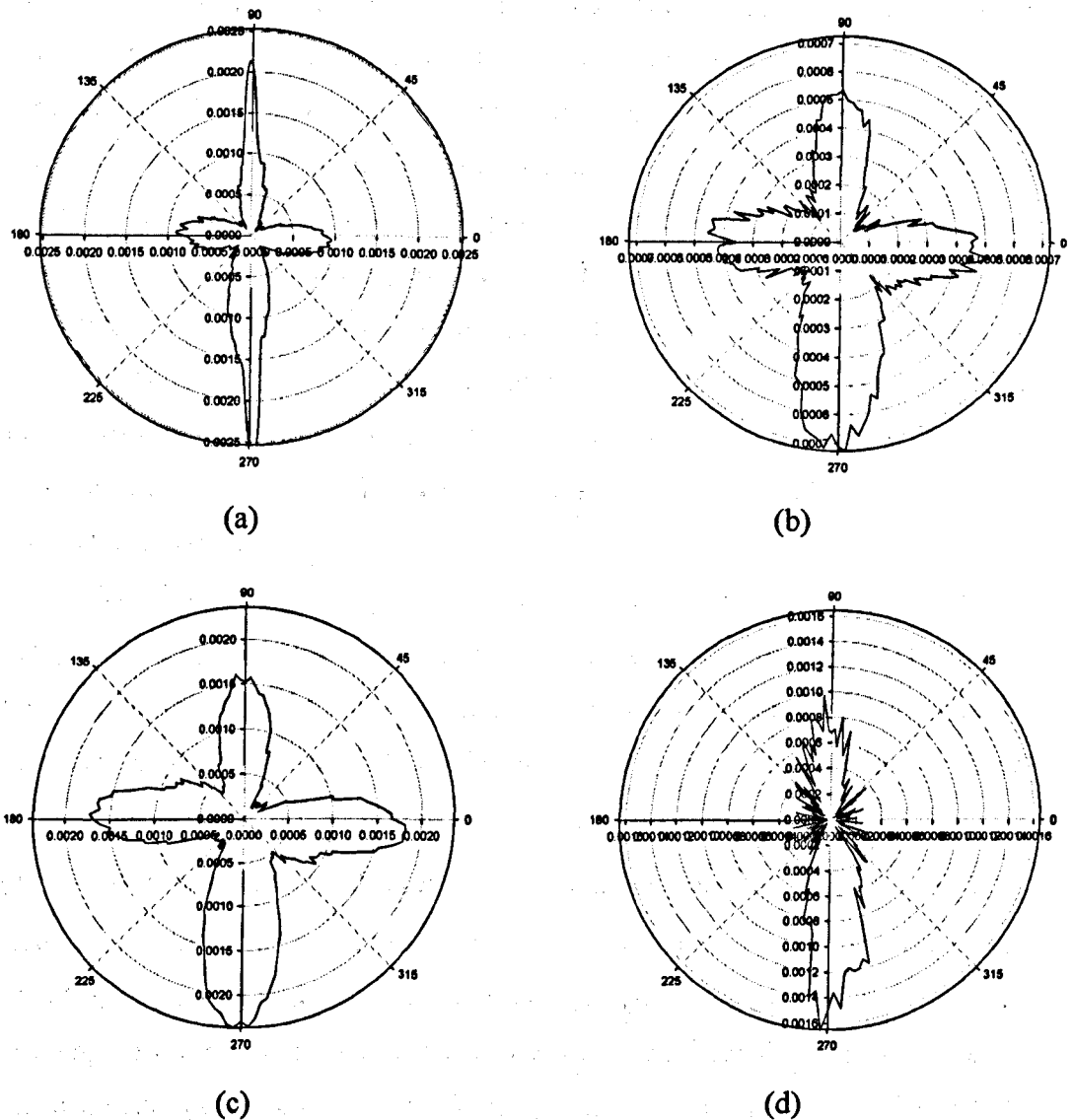


Figure 6.27: Directivity on 0.39 mm thick steel, the scales are shown in arbitrary scales, (a) s_0 peak-to-peak, (b) a_0 peak-to-peak, (c) a_1 peak-to-peak, and (d) s_2 peak-to-peak.

6.10 Conclusions

A pair of EMATs has been used for the generation and detection of Lamb waves on steel sheets. The group velocity of the zero-order asymmetric and symmetric Lamb wave mode (a_0 and s_0), as well as the a_1 and s_2 of higher-order Lamb wave mode have been measured on metal sheets as a function of angle to the rolling direction. The generation and detection of multiple modes was predicted using the Rayleigh-Lamb frequency relationship, and it has

shown a good agreement with experimental results. The overlapping modes within the signal were further identified using the Short-Time Fourier Transform (STFT). Although the first-order symmetric Lamb wave mode (s_1) has not been detected, the use of smaller coil spacing can improve the detection of s_1 as was indicated by the dispersion curves. The Stationary Wavelet Transform (SWT) was employed to extract the information required to evaluate the texture characteristics of metal sheets. The exact orientation distribution coefficients (ODCs) values obtained in the experiments have been used for comparison with the theoretical fit. It is thus possible to extract the ODCs with 95% degree of confidence. This can be used as an indication of the suitability of the metal for cold forming technique.

The influence of dispersion on the texture measurements is quantified using the s_0 fundamental mode. An experiment was performed for ideal measurements of phase velocity, and this is used to serve as an accurate reference to the measurements made on a thicker sheet. The optimum phase velocity experiment has as low a thickness-wavelength ratio (t/λ) as possible (e.g. ~ 0.03), whereas the thicker sheet experiment has (t/λ) of ~ 0.22 . This resulted in small but statistically significant deviations from the predicted anisotropy. The asymmetric zero and first order (a_0 and a_1) modes were chosen to compare the entire experimental dataset obtained from the s_0 mode. The a_0 mode appeared to have a similar velocity angular dependent pattern. The fastest direction for both s_0 and a_0 occur at the perpendicular to the rolling direction. There is a large velocity difference along the rolling direction. The a_1 mode has a $\pm 90^\circ$ shift velocity angular dependent pattern compared to the s_0 mode. Interestingly, the s_0 mode has the largest variation of the group velocity (V_g) against the angular axis, and the a_1 mode has the least. The directivity pattern observed using the amplitude is mostly due to the effect of birefringence.

6.11 References

- [1] S. G. Mallat, "Theory for multiresolution signal decomposition: the wavelet representation," *IEEE Trans. Pattern Anal. Mach. Intell.*, vol. 11, pp. 674-693, 1989.

- [2] M. Lang, H. Guo, J. E. Odegard, C. S. Burus and R. O. Wells Jr, "Noise reduction using an undecimated discrete wavelet transform," *IEEE Signal Process. Lett.*, vol. 3, pp. 10-12, 1996.
- [3] A. Cohen and R. D. Ryan, *Wavelets and Multiscale Signal Processing*. London : Chapman & Hall, 1995.
- [4] Gao Qing-wei, Li Hai-ying, Zhuang Zhen-quan and W. Tao, "Denoising of ECG signal based on stationary wavelet transform," *Acta Electron. Sin.*, vol. 31, pp. 238-40, 02. 2003.
- [5] Huang Shi-liang, Wu Guang-yao and Qiu Jian-qing, "A method using stationary wavelet transform for reduction of truncation artifacts in MR imaging," *Chin. J. Med. Imag. Technol.*, vol. 21, pp. 472-4, 03/20. 2005.
- [6] W. A. Mahmoud and I. K. Ibraheem, "Image denoising using stationary wavelet transform," *Adv. Model. Anal. B, Signals, Inf., Patterns, Data Acquis., Transm., Process., Classif.*, vol. 46, pp. 1-17, 2003.
- [7] X. H. Wang, R. S. H. Istepanian and Y. H. Song, "Microarray image denoising using stationary wavelet transform," in *International Conference on Information Technology - Applications in Biomedicine*, 2003, pp. 15-18.
- [8] R. Roe, "Description of Crystallite Orientation in Polycrystalline Materials. III. General Solution to Pole Figure Inversion," *J. Appl. Phys.*, vol. 36, pp. 2024-2031, 1965.
- [9] R. Roe, "Inversion of Pole Figures for Materials Having Cubic Crystal Symmetry," *J. Appl. Phys.*, vol. 37, pp. 2069-2072, 1966.
- [10] P. R. Morris and J. W. Flowers, "Texture and magnetic properties," *Texture Cryst. Solids (UK)*, vol. 4, pp. 129-41, 1981.
- [11] R. B. Thompson, J. F. Smith, S. S. Lee and G. C. Johnson, "Comparison of ultrasonic and X-ray determinations of texture in thin Cu and Al plates," *Metall. Trans. A, Phys. Metall. Mater. Sci. (USA)*, vol. 20A, pp. 2431-2447, 1989.
- [12] A. V. Clark Jr., R. C. Reno, R. B. Thompson, J. F. Smith, G. V. Blessing, R. J. Fields, P. P. Delsanto and R. B. Mignogna, "Texture monitoring in aluminium alloys: a comparison of ultrasonic and neutron diffraction measurement," *Ultrasonics*, vol. 26, pp. 189-97, 07. 1988.
- [13] A. V. Clark Jr., R. B. Thompson, Y. Li, R. C. Reno, G. V. Blessing, D. V. Mitrakovic, R. E. Schramm and D. Matlock, "Ultrasonic measurement of sheet steel texture and formability: comparison with neutron diffraction and mechanical measurements," *Res. Nondestr. Eval.*, vol. 2, pp. 239-57, 1990.

- [14] M. D. G. Potter, S. Dixon and C. Davis, "Development of an automated non-contact ultrasonic texture measurement system for sheet metal," *Meas Sci Technol*, vol. 15, pp. 1303-8, 07. 2004.
- [15] S. Dixon, C. Edwards and S. B. Palmer, "Texture measurements of metal sheets using wideband electromagnetic acoustic transducers," *J. Phys. D, Appl. Phys.*, vol. 35, pp. 816-24, 04/21. 2002.
- [16] M. Hirao, K. Aoki and H. Fukuoka, "Texture of polycrystalline metals characterized by ultrasonic velocity measurements," *J. Acoust. Soc. Am.*, vol. 81, pp. 1434-40, 05. 1987.
- [17] M. Hirao, H. Fukuoka, K. Fujisawa and R. Murayama, "Characterization of formability in cold-rolled steel sheets using electromagnetic acoustic transducers," *Metall. Trans. A, Phys. Metall. Mater. Sci.*, vol. 20A, pp. 2385-92, 11. 1989.
- [18] M. D. G. Potter and S. Dixon, "Apparent texture symmetry deviations in aluminum sheet," *IEEE Trans. Ultrason. Ferroelectr. Freq. Control*, vol. 52, pp. 1791-6, 10. 2005.
- [19] M. Hirao, N. Hara, H. Fukuoka and K. Fujisawa, "Ultrasonic monitoring of texture in cold-rolled steel sheets," *J. Acoust. Soc. Am.*, vol. 84, pp. 667-72, 08. 1988.
- [20] H. Kopineck, R. Loffel and H. Otten, "Industrial on-line texture determination in rolled steel strips," *J. Nondestr. Eval.*, vol. 12, pp. 13-19, 1993.
- [21] R. Murayama, K. Fujisawa, H. Fukuoka and M. Hirao, "Development of an on-line evaluation system of formability in cold-rolled steel sheets using electromagnetic acoustic transducers (EMATs)," *NDT E Int.*, vol. 29, pp. 141-146, 1996.
- [22] E. P. Papadakis, R. B. Thompson, S. J. Wormley, D. D. Bluhm, H. D. Skank, G. A. Alers, K. Forouraghi, J. R. Griffiths, R. M. Parker, W. D. Thomas and D. H. Birlingmair, "Development of an automatic ultrasonic texture instrument and its transition from laboratory to market: a model for technology transfer," *Mater. Eval.*, vol. 51, pp. 77-85, 01. 1993.
- [23] R. B. Thompson, E. P. Papadakis, D. D. Bluhm, G. A. Alers, K. Forouraghi, H. D. Skank and S. J. Wormley, "Measurement of texture and formability parameters with a fully automated, ultrasonic instrument," *J. Nondestr. Eval.*, vol. 12, pp. 45-62, 03. 1993.
- [24] R. B. Thompson, S. S. Lee and J. F. Smith, "Relative anisotropies of plane waves and guided modes in thin orthorhombic plates: implication for texture characterization," *Ultrasonics*, vol. 25, pp. 133-7, 05. 1987.
- [25] R. B. Thompson, S. S. Lee and J. F. Smith, "Angular dependence of ultrasonic wave propagation in a stressed, orthorhombic continuum:

- theory and application to the measurement of stress and texture,” *J. Acoust. Soc. Am.*, vol. 80, pp. 921-31, 1986.
- [26] M. Hirao and H. Fukuoka, “Dispersion relations of plate modes in anisotropic polycrystalline sheets,” *J. Acoust. Soc. Am.*, vol. 85, pp. 2311-15, 06. 1989.
- [27] Y. Li and R. B. Thompson, “Influence of anisotropy on the dispersion characteristics of guided ultrasonic plate modes,” *J. Acoust. Soc. Am.*, vol. 87, pp. 1911-31, 05. 1990.
- [28] P. P. Delsanto, R. B. Mignogna and A. V. Clark Jr., “Ultrasonic texture and stress measurements in anisotropic polycrystalline aggregates,” *J. Acoust. Soc. Am.*, vol. 87, pp. 215-24, 01. 1990.
- [29] D. R. Allen and C. M. Sayers, “The measurement of residual stress in textured steel using an ultrasonic velocity combinations technique,” *Ultrasonics*, vol. 22, pp. 179-88, 07. 1984.
- [30] Y. Arai and H. Kobayashi, “Influence of structure anisotropy on acoustoelastic effect,” in *Proceedings of the International Conference*, 1987, pp. 709-20.
- [31] M. D. G. Potter, S. Dixon, C. L. Davis and G. Kong, “Analysis of asymmetry of acoustic velocity in cubic sheet metals,” in *AIP Conf. Proc.*, 2005, pp. 1323-30.
- [32] R. Murayama, “Non-destructive evaluation of formability in cold rolled steel sheets using the SH_0 -mode plate wave by electromagnetic acoustic transducer,” *Ultrasonics*, vol. 39, pp. 335-43, 08. 2001.
- [33] C. M. Sayers, D. R. Allen, G. E. Haines and G. G. Proudfoot, “Texture and stress determination in metals by using ultrasonic Rayleigh waves and neutron diffraction,” *Philos. Trans. R. Soc. Lond. A, Math. Phys. Sci.*, vol. 320, pp. 187-98, 1986.
- [34] Y. Li and R. B. Thompson, “Effects of dispersion on the inference of metal texture from S_0 plate mode measurements. Part I. Evaluation of dispersion correction methods,” *J. Acoust. Soc. Am.*, vol. 91, pp. 1298-309, 03. 1992.
- [35] C. M. Sayers, “Ultrasonic velocities in anisotropic polycrystalline aggregates,” *J. Phys. D, Appl. Phys.*, vol. 15, pp. 2157-67, 11/14. 1982.
- [36] R. B. Thompson, “Generation of horizontally polarized shear waves in ferromagnetic materials using magnetostrictively coupled meander-coil electromagnetic transducers,” *Appl. Phys. Lett.*, vol. 34, pp. 175-7, 01/15. 1979.
- [37] R. B. Thompson, “A model for the electromagnetic generation of ultrasonic guided waves in ferromagnetic metal polycrystals,” *IEEE Trans. Sonics Ultrason.*, vol. SU-25, pp. 7-15, 01. 1978.

- [38] B. Igarashi, G. A. Alers and P. T. Purtscher, "Magnetostrictive EMAT efficiency as a materials characterization tool," in *Review of Progress in Quantitative Nondestructive Evaluation*, 1998, pp. 1485-92.
- [39] R. Murayama, "Driving mechanism on magnetostrictive type electromagnetic acoustic transducer for symmetrical vertical-mode Lamb wave and for shear horizontal-mode plate wave," *Ultrasonics*, vol. 34, pp. 729-36, 10. 1996.
- [40] S. G. Mallat, *A Wavelet Tour of Signal Processing*. London : Academic Press, 1998.
- [41] I. Daubechies, "The wavelet transform, time-frequency localization and signal analysis," *IEEE Trans. Inf. Theory*, vol. 36, pp. 961-1005, 1990.

Chapter 7

EMATs Fabricated using Micro-Stereolithography

7.1 Introduction

In fabrication terms, the most complicated part of an EMAT is the coil. This is usually wire-wound, although a printed circuit board (PCB) can be used for planar coils [1–2]. While these methods are effective, they are limited in scope. A possible alternative is the stereolithography process, which allows a wide range of shapes and components to be manufactured as part of a rapid prototyping system [3]. Here the component is built up from a series of layers, using photo-polymerisation of liquid polymers in patterns defined by optical masks. While this is a common technique in manufacturing, it is only recently being introduced into more high precision components due to the development of micro-stereolithography (MSL) [4]. This allows objects with greater precision to be fabricated in this way. MSL can be used, for instance, in the fabrication of micro-gears, micro-tubes and micro-convex cone structures [5]. Other experiments have shown that the piezoelectric properties of PZT ceramics fabricated by such techniques are promising, which implies such structures could be integrated within devices to produce microactuators or sensors [6]. Applications in facial reconstructive surgery have been in place for some time [7]. Despite the above, the manufacture of ultrasonic devices such as EMATs using MSL for use in non-destructive testing does not seem to have been described in the literature.

A wide range of applications could be envisaged for EMATs produced by MSL techniques. The main advantage is the ability to produce relatively complex EMAT coils. For example, the front face of the coil can be designed with a specific geometry to fit a given sample topography. This could subsequently reduce the coupling energy losses and improve the efficiency of transduction for complicated shapes. Another advantage is that this technology

can produce complex coil designs, so that one-off prototypes can be produced and tested at minimal cost.

The data obtained from these EMATs has been processed using the SAFT approach. SAFT was designed to overcome some of the limitations imposed by large physical apertures, and has been successfully applied in a broad range of imaging applications, such as radar [8], ultrasonic testing [9], geophysical exploration [10], concrete testing [11] etc. The synthetic aperture method is based on the concept of collecting data from many transmitter-receiver separations, so as to simulate a large transducer with much better resolution and SNR ratio.

In the following, the MSL process used to fabricate EMATs is described, and this is followed by a description of the SAFT algorithm used to reconstruct images of data obtained from these EMATs. Finally, results are given, demonstrating that the EMATs can be used to perform NDE inspections. The work has been submitted as a journal paper in [12].

7.2 Micro-Stereolithography for EMAT Fabrication

The EMATs were produced using a PERFACTORY® Mini SXGA Multi Lens MSL machine, shown schematically in Figure 7.1. This can be used to fabricate prototype EMATs by solidifying a methacrylate photopolymer resin in a series of pre-defined layers. This is achieved by shining light patterns onto the liquid, causing polymerisation to occur where required. Each new layer is added to the structure in turn. The advantage of this approach is that it uses a micro-mirror to form the light pattern, with software controlling the intensity distribution (and hence the solid shape) at each layer. The effective pixel size is approximately 24 μm in the horizontal (XY) plane. The vertical tolerance is 10 μm , representing the minimum thickness of each layer in the vertical (Z) direction. This enables the construction of extremely small and accurate three-dimensional models from computer-aided design (CAD) data.

Solidworks™ 3D-CAD software was used to design and generate an MSL file for both spiral and meander-line EMATs. The spiral coil had 10 turns

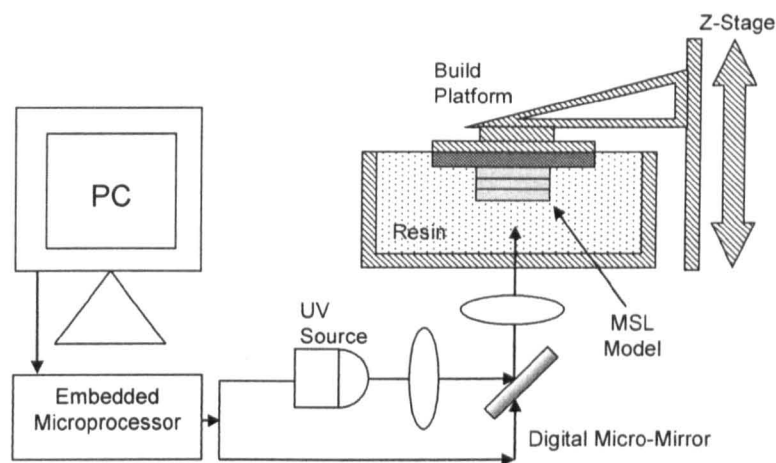


Figure 7.1: Schematic diagram of micro-stereolithography process used to fabricate EMAT coils.

with an outer diameter of 20 mm. The track width and clearance were both set at approximately 0.5 mm. The thickness of the photopolymer block upon which the coil was mounted was set at 5 mm. The meander-line was designed with 12 turns, and was 30 mm long and 10 mm width. The meander-line pitch was 0.9 mm. Figure 7.2 shows an example of the 3D-CAD model for these spiral and meander-line EMAT coils.

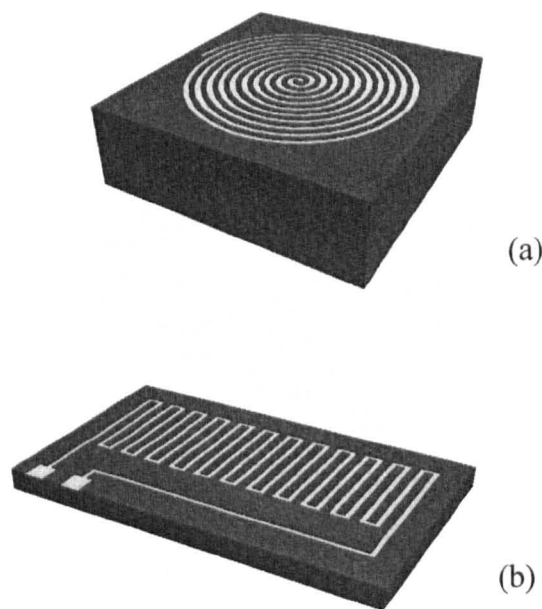


Figure 7.2: 3D-CAD models of the types of EMAT coil constructed using MSL, these being (a) spiral and (b) meander-line geometries.

Figure 7.3 shows the process flow for the production of a spiral EMAT. Note the spiral pattern of a circular EMAT is described by depressions on the surface. The part itself is essentially a block of solidified photopolymer (Figure 7.3(a)) with surface detail corresponding to the required geometry of the EMAT. The surface of the photopolymer block is patterned such that depressed areas correspond to where metal will be required on the completed transducer. The complete EMAT architecture was realised using a combination of electro-deposition and polishing post-processing techniques applied to the basic structure produced by MSL. This was obtained by sputtering a conformal layer of gold over the surface of the block (Figure 7.3(b)). The final stage is polishing the surface of the block down to its original surface (Figure 7.3(c)), thereby removing the deposited gold from all raised areas, and leaving the required geometry of gold on the surface of the block.

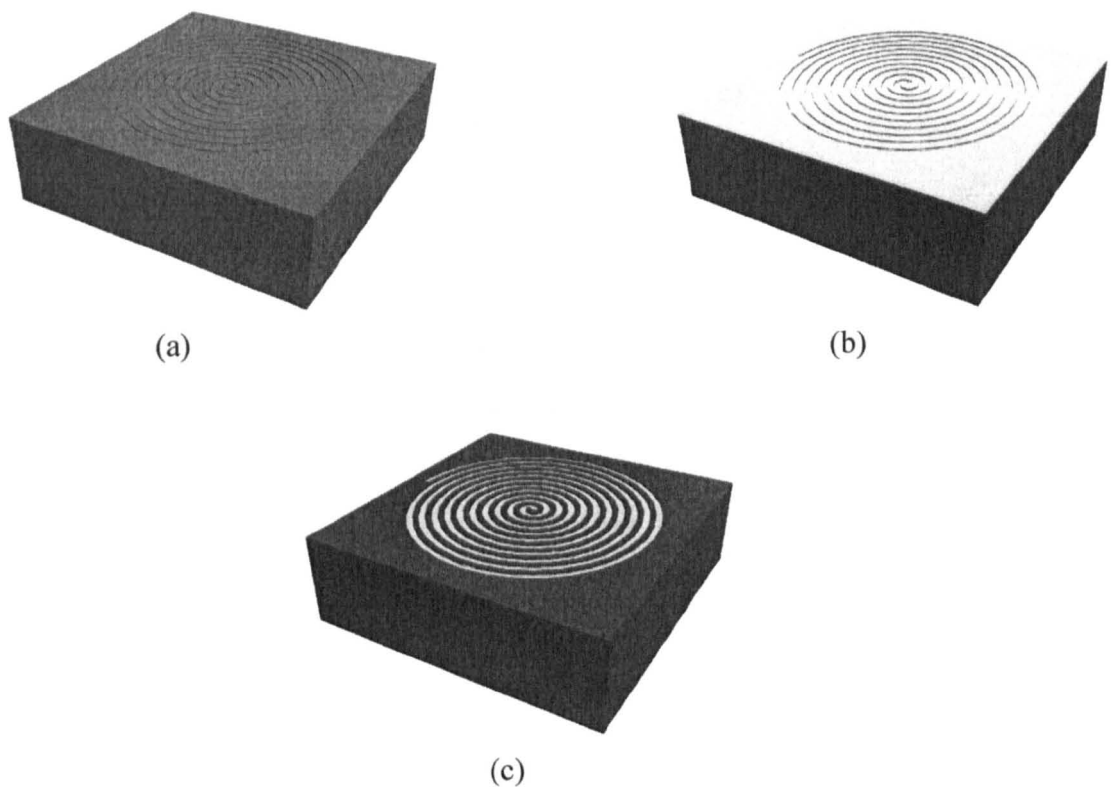


Figure 7.3: Process flow for production of a spiral EMAT. (a) MSL model is created, defining spiral EMAT architecture; (b) 200 nm planar layer of gold is sputtered over entire model; (c) model is polished to leave only depressions describing the spiral.

An example of an EMAT coil produced in this way is illustrated in Figure 7.4 (in this case a spiral coil EMAT shown in Figure 7.4(a) and meanderline EMAT shown in Figure 7.4(b)).

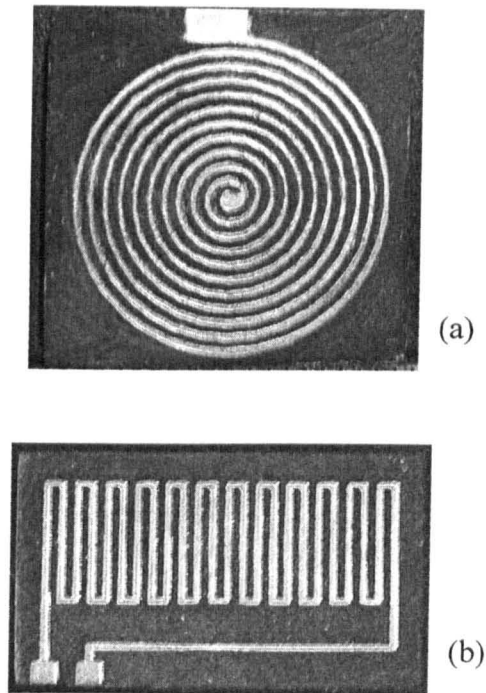


Figure 7.4: Example of EMAT coil manufactured using MSL, (a) a spiral EMAT and (b) meanderline EMAT.

The construction of the full device is shown in Figure 7.5. The coil was placed against the flat face of a cylindrical neodymium-iron-boron (Nd-Fe-B) sintered magnet, which had a maximum flux density B_r of ~ 1.5 T. This provided a magnetic field primarily in the direction normal to the sample surface and the plane of the coil. The magnet was backed by a cylindrical steel block of 40 mm thickness and 25 mm diameter to decrease the demagnetising factor [13], thus providing an increase in the normal component of the static magnetic field.

7.3 Experimental Measurements of EMAT Performance

The apparatus used to characterise the EMATs produced by micro-stereolithography (MSL) is shown in Figure 7.6. The EMAT receiver was

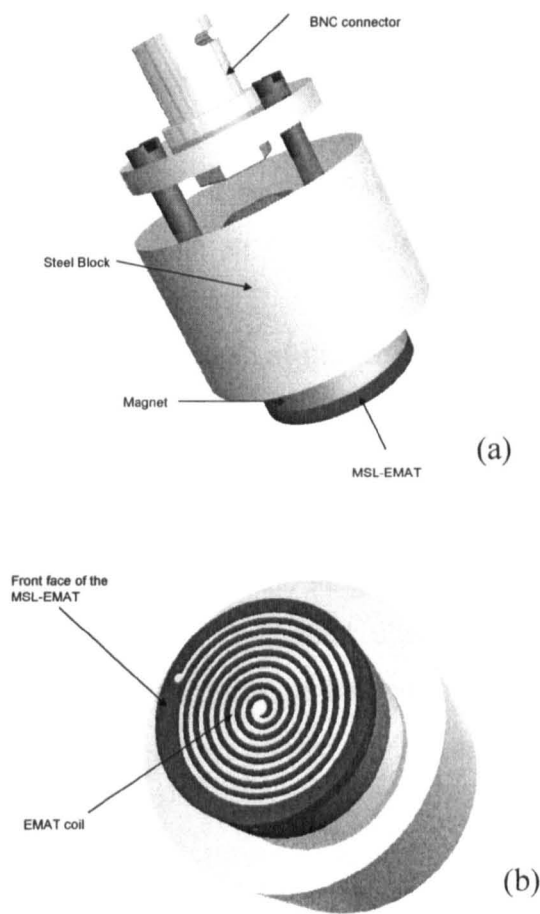


Figure 7.5: Manufacture of an EMAT probe prototype.

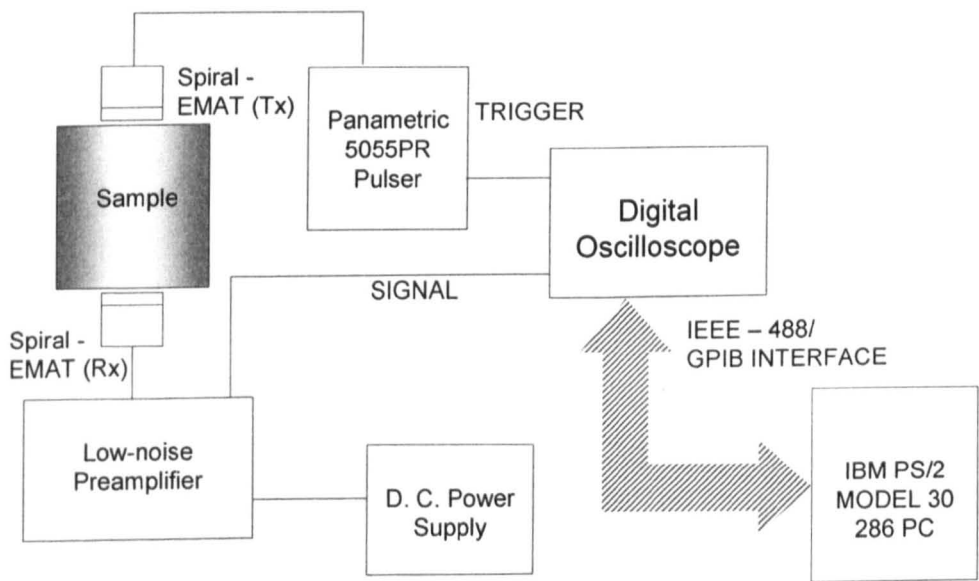


Figure 7.6: The experimental setup used for the characterisation of EMATs fabricated using MSL.

placed directly opposite a similar EMAT source in through-transmission across a 10 mm thick aluminium sample. The source EMAT was driven with a -400 V unipolar pulse from a Panametrics 5055PR pulser-receiver. A low-noise, high impedance preamp was attached to the EMAT receiver. The time domain waveform was then recorded on an Agilent 54622D digital oscilloscope, with 1024 signal averages.

Figure 7.7 shows an example of the received time signal (Figure 7.7(a)) and the corresponding frequency spectra (Figure 7.7(b)) for the three multiple shear wave arrivals (S1, S3 and S5). The first received component at $\sim 3.2 \mu\text{s}$ corresponds to the radially polarised shear wave generated by the EMAT source that has propagated directly through the sample from source to receiver, giving a velocity of $3165 \pm 35 \text{ ms}^{-1}$. The radial ultrasonic wave has a dominant frequency content centred at $\sim 2 \text{ MHz}$, extending to around 10 MHz. The third (S3) and fifth (S5) reflection echoes arrived at $\sim 9 \mu\text{s}$ and $15 \mu\text{s}$.

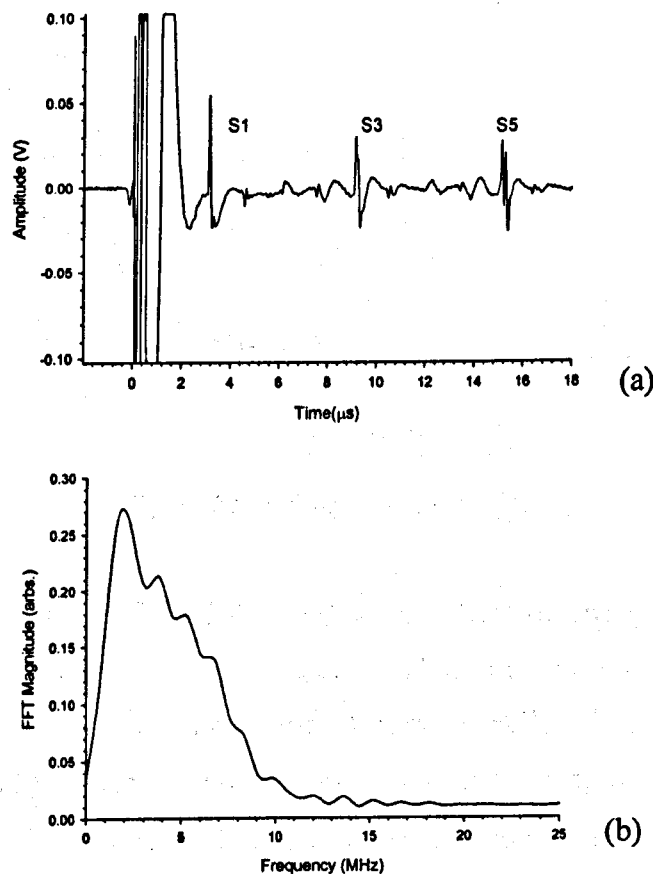


Figure 7.7: Spiral-coil MSL EMATs in through-transmission. (a) Received time signal, and (b) corresponding frequency spectrum for the first arrival S1.

All EMATs have lift-off effects associated with their operation, which causes a change in the effective impedance of the EMAT. Consequently, a phase shift in the output voltage of a receiving EMAT could be produced. This can cause errors when the EMAT is used for velocity measurements [1]. In addition, the sensitivity of the EMAT will generally decrease with the distance of the coil from the surface. To evaluate this effect, the receiver lift-off was varied from $z = 0$ to 5 mm, with a spatial resolution of 0.1 mm. It was measured using a micrometer. The EMAT transmitter had a fixed air gap of 0.2 mm to the sample surface. Figure 7.8 shows the results, where the solid-line represents the actual experimental results and the dashed line corresponds to a curve fitted to the data. As expected [14], the drop in amplitude with increased lift-off was exponential, with the EMATs usable with gaps of up to 0.6 mm.

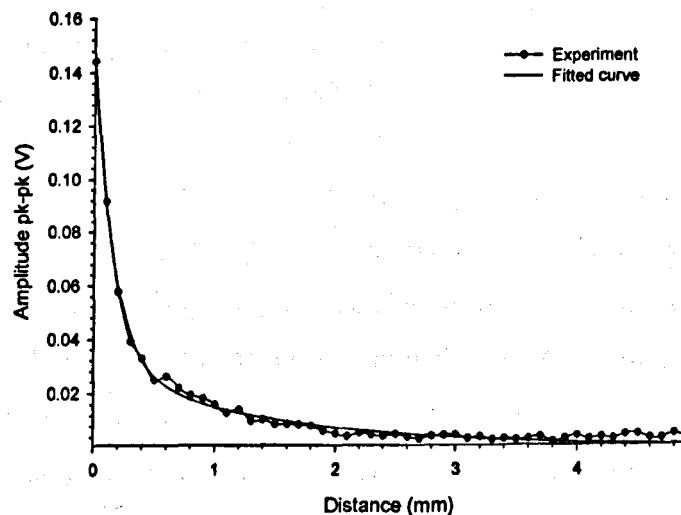


Figure 7.8: Lift-off experimental result.

To test the MSL EMATs further, the effect of changing the magnetic field strength was investigated. Here the solid-state magnets were replaced by a water-cooled electromagnet, constructed from enamelled 0.22 mm thick copper wire (134AWP) wound around a 20 mm diameter, 20 mm long mild steel core. A water-cooled unit was used to control the temperature at around 15 °C. The electromagnet was used to evaluate the sensitivity of a spiral-coil EMAT source, by changing the magnitude of the bias magnetic field and detecting the change

in received amplitude, using the apparatus of Figure 7.6 with a fixed receiver. The peak-to-peak amplitude of the first arrival (S1 in Figure 7.7) was plotted as a function of magnetic field strength, measured using a Hall probe, the results being shown in Figure 7.9. This shows that the efficiency of a spiral MSL EMAT was proportional to the square of the magnetic field strength.

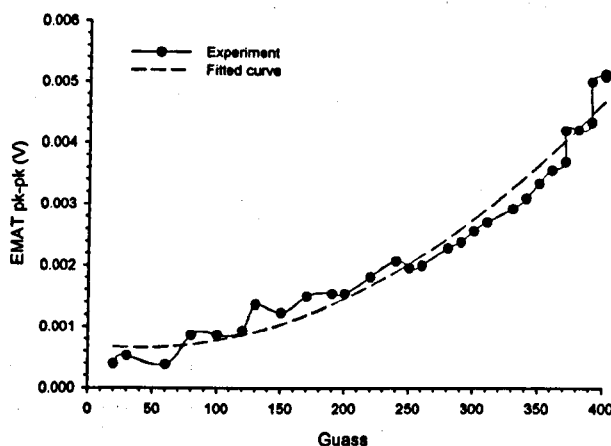


Figure 7.9: The influence of magnetic field strength on the spiral-coil EMAT performance.

EMATs can generate high intensity signals when driven by tone-burst signals. EMATs generally behave as inductive loads, and the EMAT impedance for a particular driving frequency can be altered using capacitors in parallel with the coil to better match to the output impedance of a power amplifier. The proper design of impedance matching networks requires knowledge of the impedance of both the driver and receiver and the EMAT. It is thus important to be able to estimate the inductance of a spiral EMAT coil made using the MSL approach. This was measured using the circuit of Figure 7.10(a) for different numbers of turns of a spiral coil EMAT, and the results plotted as shown in Figure 7.10(b). The results show that the coil inductance increases as a function of the square of the number of turns, while the coil resistance increases linearly. The EMAT coils produced using MSL technology are thus behaving as expected.

The above measurements all used the spiral coil EMAT geometry, whereas interesting directivity effects can be produced using meander-line

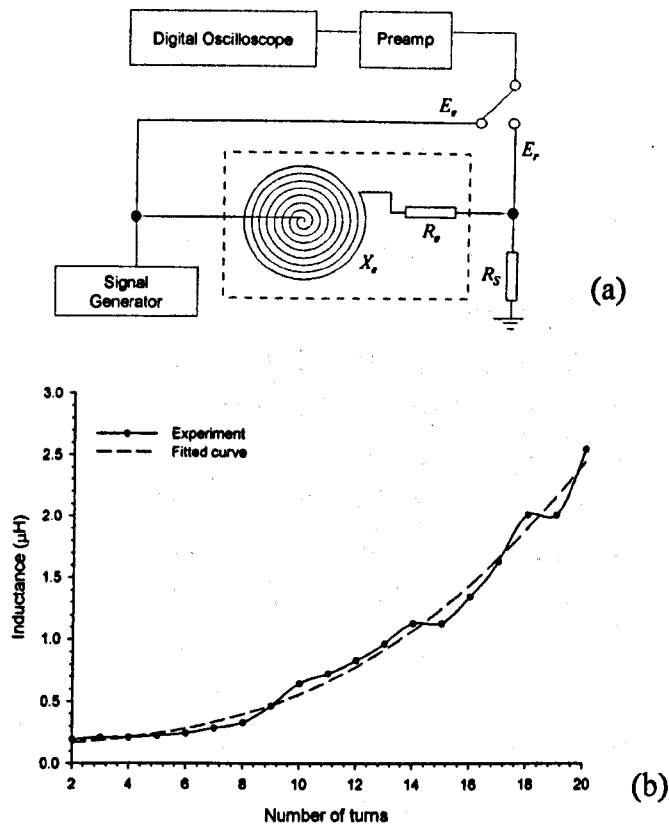


Figure 7.10: (a) Schematic diagram of the experimental circuit to measure EMAT coil inductance. (b) Spiral-coil EMAT inductance as a function of the number of turns in the coil.

geometries (Figure 7.1(b) and Figure 7.4(b)). Directivity patterns were measured using a semi-cylindrical sample of aluminium, whose diameter was 200 mm with an axial length of 100 mm. The meander-line EMAT was located on the middle of the flat surface. The Shear-vertical (SV) wave [15] thus generated was detected by a spiral-coil EMAT receiver, scanned at $\theta = 5^\circ$ intervals around the cylindrical surface. The results for a meander-line spacing (l) of 0.9 mm is shown in Figure 7.11, where the received frequency spectra at various angles are displayed together, with the lighter regions representing higher received amplitudes. It will be seen that the frequency at which the signal amplitude is a maximum is a function of angle. Theory states that for a metal with a given longitudinal velocity (c) there should be maximum signal radiated at some angle given by [15]:

$$\sin \theta = \frac{c}{2l \times f} \quad (7.1)$$

The predictions of this equation are also shown as the dotted line in Figure 7.11, in good agreement with the experimental data.

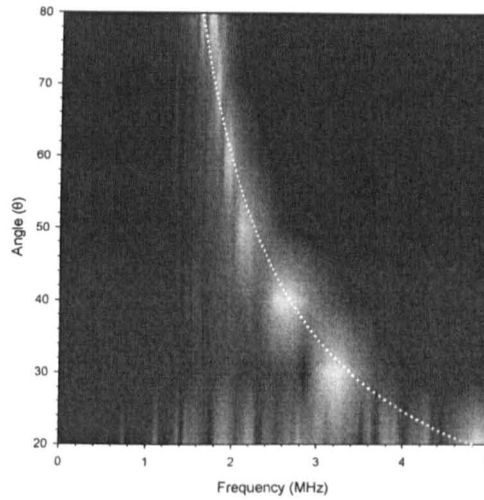


Figure 7.11: Frequency and SV propagation angle of different meanderline conductor spacing, of 0.9 mm.

The directivity at a particular frequency was also measured using a tone-burst signal at selected frequencies. Figures 7.12(a) - (e) shows the results for SV shear mode, over a range of θ from 30° - 70° respectively, for a meanderline transmitter with $l = 0.9$ mm. The broadest main-lobes are the 30° and 70° propagated angles, and they correspond to a -6 dB level of approximately 23° and 29° respectively. The main lobes for the other angles are sharper. However, it can be seen that shear wave beam steering was accomplished successfully using this EMAT design. This was obtained by using different frequencies with a fixed meander-line spacing.

7.4 Imaging Using Synthetic Aperture Focussing Technique

Experiments have been performed using an MSL meander-line source and a spiral-coil EMAT as a receiver, to demonstrate that the new fabrication technology could lead to practical imaging systems. The algorithm and software used to implement Synthetic Aperture Focussing Technique (SAFT) imaging in this study can be found in [16]. Figure 7.13 shows the experimental setup used.

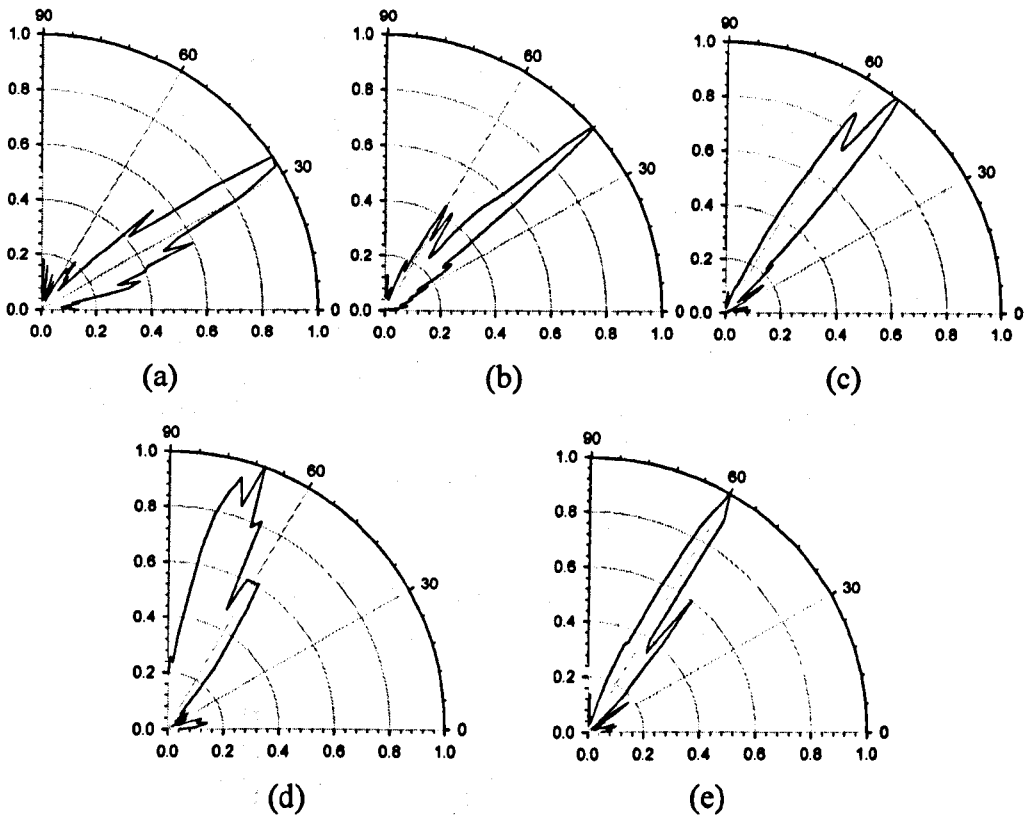


Figure 7.12: Directivity patterns for a meander-line EMAT source with $l = 0.9$ mm. (a) $\theta = 30^\circ$ (b) $\theta = 40^\circ$ (c) $\theta = 50^\circ$ (d) $\theta = 60^\circ$ and (e) $\theta = 70^\circ$.

The meander-line transmitter was driven with a tone-burst signal from a WaveTek-191 signal generator, providing a peak-to-peak amplitude of 500 mV, which was subsequently amplified using an ENI A-300 power amplifier with a typical gain of 55 dB. The position of the spiral-coil EMAT receiver was controlled by a single linear scanning stage. The received signal was amplified using a low-noise preamp with a typical gain of 62 dB. A second-order Butterworth high-pass filter was used to remove some of the low-frequency noise. The digital waveform data was recorded using a Tektronix TDS430 digital oscilloscope, and the data transferred to a PC via the IEEE-488 (GPIB) interface controlled by LabviewTM.

A typical ultrasonic waveform is presented in Figure 7.14, which shows the reflected signal (both waveform and spectrum) from a cylindrical hole of 15 mm diameter. The transmitter and receiver EMATs were separated by ~100 mm, and driven with a 2.15 MHz tone-burst signal. This gave an angled beam

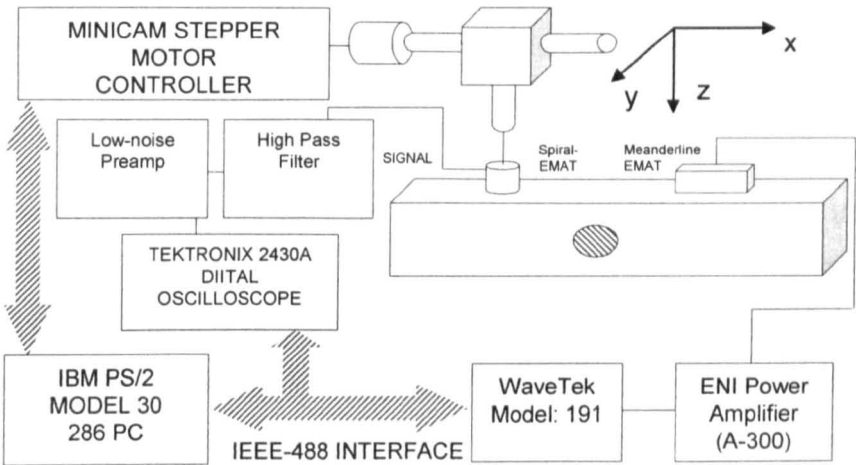


Figure 7.13: Experimental setup used for SAFT imaging.

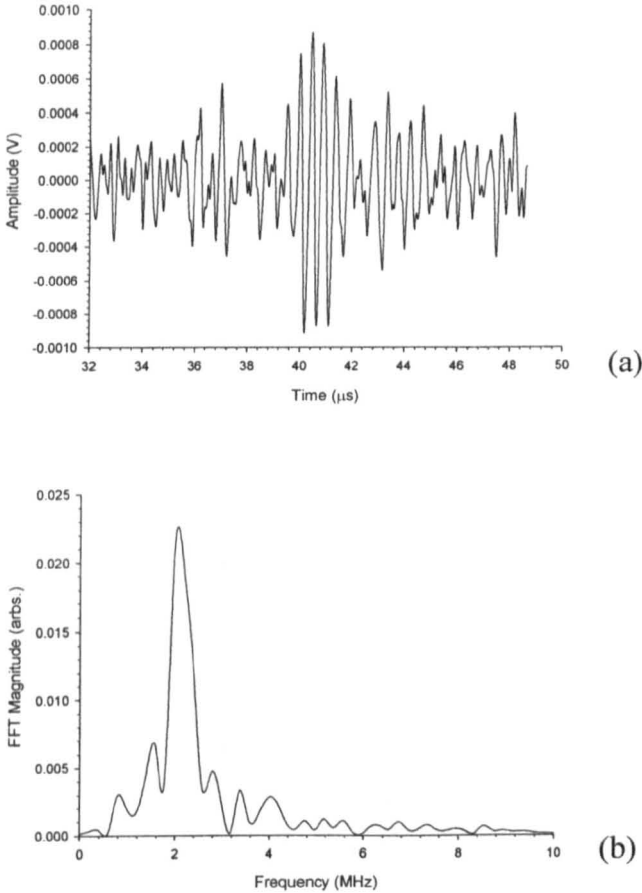


Figure 7.14: A shear-vertical wave reflected from an artificial circular defect using MSL EMATs. The source was driven by a high power tone-burst with a centre frequency of 2.15 MHz. (a) The time received waveform, and (b) the corresponded frequency spectrum.

from the source at $\theta \sim 60^\circ$ to the normal, with the total travel path length being ~ 120 mm. As can be seen the artificial defect was easily detected.

SAFT imaging was now performed. With the transmitter fixed at one location, the receiver was moved in steps of 1 mm away from the transmitter and waveforms recorded at each point. The process was then repeated until data was collected over a range of angular source position (45° - 65°). SAFT images obtained from a cylindrical hole of 10 mm diameter, centred at a depth of 37.5 mm, are shown in Figures 7.15(a) and (b) for two EMAT receiver diameters of 10 mm and 5 mm respectively. The position of the defect is indicated by the white circle on the image. The peak amplitude in the image is located at $x = 125$ mm and $z = 32.5$ mm in each case, which is its true position. Despite the complexity and low SNR of the transmitted signals, the position of the flaw can be directly read from the image. For the larger receiver, the SNR was better but the resultant spatial resolution not as good, as might be expected. An experiment was also performed for a 5 mm diameter defect, the result being shown in Figure 7.16. Note that the size of the focussing ellipse has decreased compared to the one obtained in Figure 7.15, as expected for a smaller diameter EMAT receiver.

7.5 Conclusions

This work has demonstrated that rapid prototyping techniques can be used for the fabrication of EMATs. The EMAT coil pattern was created using an MSL process, and the complete EMAT architecture was produced using a combination of electro-deposition and polishing post-processing techniques. Two types of practical devices for different kinds of elastic wave generation were constructed and used to make ultrasonic measurements. These devices were characterised in terms of bandwidth and directivity, using both meander-line and spiral-coil geometries for shear wave generation. The detection of reflections from artificial defects was demonstrated, and their use in a SAFT imaging system led to the successful reconstruction of images. These MSL EMATs are likely to have many applications in NDE, as they can be made in a

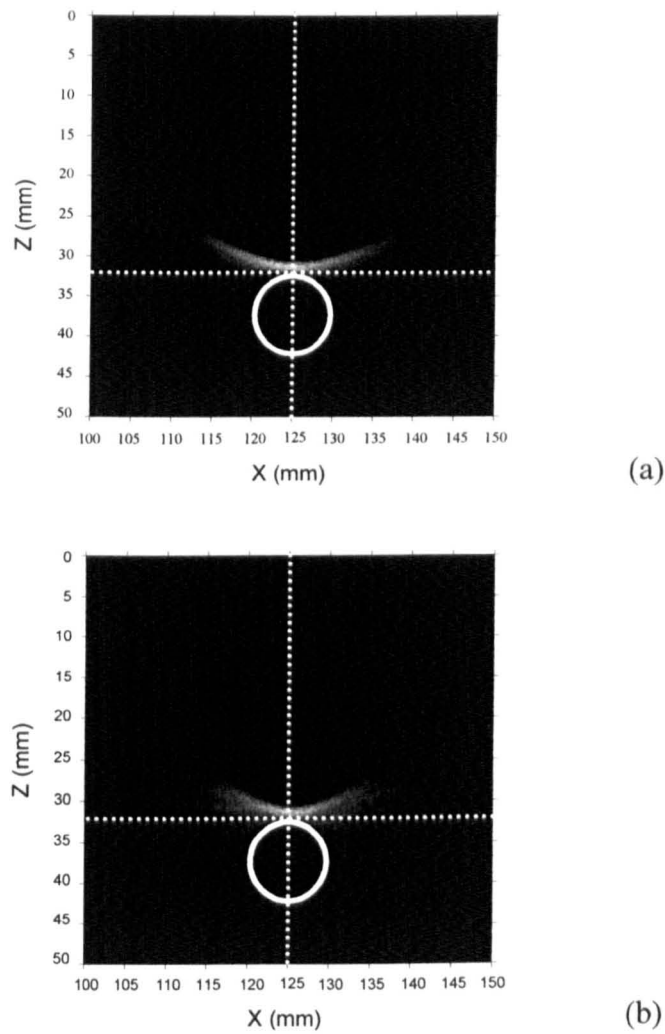


Figure 7.15: SAFT image of a 10 mm through-hole defect (shown as the white circle) located at (125 mm, 32.5 mm), using EMAT receivers of (a) 105 mm and (b) 5 mm diameter.

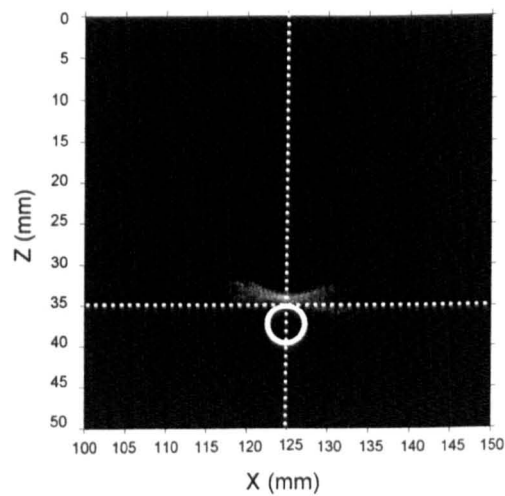


Figure 7.16: SAFT reconstructed image of a 5 mm through-hole defect, located at (125 mm, 35 mm).

wide variety of shapes and sizes in a reproducible fashion. The use and complexity of possible EMAT configurations can become easier with the MSL technology increases, and it can also incorporate the electronics and magnets into the design.

7.6 References

- [1] B. W. Maxfield and C. M. Fortunko, "The design and use of electromagnetic acoustic wave transducers (EMATs)," *Mater. Eval.*, vol. 41, pp. 1399-408, 11. 1983.
- [2] G. A. Alers and L. R. Burns, "EMAT designs for special applications," *Mater. Eval.*, vol. 45, pp. 1184-9, 10. 1987.
- [3] P. F. Jacobs, *Stereolithography and Other RP\&M Technologies : From Rapid Prototyping to Rapid Tooling*. New York : Society of Manufacturing Engineers in cooperation with the Rapid Prototyping Association of SME , 1996.
- [4] B. Liu, X. Gong and W. J. Chappell, "Layer-by-layer polymer stereolithography fabrication for three-dimensional RF components," in *IEEE MTT. S. Int. Microwave Symp. Dig.*, 2004, pp. 481-4.
- [5] X. Zhang, X. N. Jiang and C. Sun, "Micro-stereolithography for MEMS," in *Proceedings of Microelectromechanical Systems (MEMS) 1998*, 1998, pp. 3-9.
- [6] X. N. Jiang, C. Sun, X. Zhang, B. Xu and Y. H. Ye, "Microstereolithography of lead zirconate titanate thick film on silicon substrate," *Sens. Actuators A Phys.*, vol. A87, pp. 72-7, 12/01. 2000.
- [7] L. K. Cheung, M. C. M. Wong and L. L. S. Wong, "The applications of stereolithography in facial reconstructive surgery," in *Proceedings International Workshop on Medical Imaging and Augmented Reality*, 2001, pp. 10-15.
- [8] P. Valin, Y. Tessier and A. Jouan, "Hierarchical ship classifier for airborne synthetic aperture radar (SAR) images," in *Proceedings of 1999 Asilomar Conference*, 1999, pp. 1230-4.
- [9] D. A. Hutchins, S. M. Kramer and C. Saleh, "SAFT processing of non-contact ultrasonic NDE data," in *IEEE 1989 Ultrasonics Symposium*, 1989, pp. 661-664.
- [10] M. Rheault, R. Simard, C. Garneau and V. R. Slaney, "SAR Landsat TM-geographical data integration utility of value-added products in

- geological exploration,” *Can. J. Remote Sens. (Canada)*, vol. 17, pp. 185-90, 04. 1991.
- [11] K. J. Langenberg, K. Mayer, A. Zimmer and C. Kohl, “Nondestructive evaluation of embedded structures in concrete: Modeling and tomographic imaging,” in *URSI 2004 International Symposium on Electromagnetic Theory*, 2004, pp. 1203-5.
- [12] K. S. Ho, R. J. Bradley, D. R. Billson and D. A. Hutchins, “Electromagnetic acoustic transducers (EMATs) fabricated using micro-stereolithography,” *Ultrasonics*, submitted for publication, Feb. 2007.
- [13] K. Muramatsu, T. Nakata, N. Takahashi, K. Fujiwara and H. Ukita, “Numerical calculation of demagnetizing factor for permanent magnet,” *COMPEL Int J Comput Math Electr Electron Eng*, vol. 14, pp. 157-161, 1995.
- [14] X. Jian, S. Dixon and R. S. Edwards, “Modelling ultrasonic generation for Lorentz force EMATs,” *Insight, Non-Destr. Test. Cond. Monit. (UK)*, vol. 46, pp. 671-3, 11. 2004.
- [15] T. J. Moran and R. M. Panos, “Electromagnetic generation of electronically steered ultrasonic bulk waves,” *J. Appl. Phys.*, vol. 47, pp. 2225-7, 05. 1976.
- [16] A. Neild, D. A. Hutchins and D. R. Billson, “Imaging using air-coupled polymer-membrane capacitive ultrasonic arrays,” in *Ultrasonics International 2003*, 2004, pp. 859-64.

Chapter 8

Conclusions

8.1 General Conclusions

In general, it can be concluded that signal processing techniques can improve the operation of EMATs. As was shown in the main chapters of this thesis, the use of pulse compression can alleviate the noise problem while improving the resolution. The result can enhance the reliability and validity of EMATs measurements. Using devices such as EMATs with wavelet processing allows retaining more of the redundant information due to modes superimposing, and reflections interference, empowering the ability to separate desired from undesired signals.

This chapter includes the conclusions from each section of the thesis, so that the reader may review the major achievements and outline of each. It finishes with a discussion of the most useful directions for subsequent work to take.

8.2 Conclusions for each Chapter

Chapter 1 in this thesis introduced some of the existing problems in EMATs. Despite the obvious attraction of their non-contact nature, EMATs have not yet found wide application, due to the poor signal-to-ratios, poor measurement spatial resolution caused by the large aperture size, mode mixing, etc. The proposed signal processing techniques to resolve the problems were described.

Chapter 2 gave a literature review of EMAT technology. The chapter gave a historical review and background to EMATs. The chapter also finished with some of the available EMAT configurations designed to date.

Chapter 3 has shown that pulse-compression signal processing techniques can be applied to EMATs, to improve some of the major weakness of EMATs, leading to a wide range of possible applications. This chapter has demonstrated that measurements of various thicknesses of metal plates can be conducted, with a high accuracy. This chapter also showed that the use of the pulse-compression processing technique reduces the amount of averaging required for data acquisition and thus improves the time taken for imaging and real time measurements. The resolution of the image obtained using the pulse-compression approach was also improved compared to a transient pulse signal from Panametrics pulser/receiver. It is thus suggested that the combination of EMATs and pulse-compression can lead to a wide range of online applications where fast time acquisition is required.

Chapter 4 described a pair of non-contact EMATs to generate and detect ultrasonic waves across beverage containers. A planar spiral EMAT prototype was designed and fabricated using PCB techniques. EMATs generate and receive elastic waves within the metallic can wall, and do not require any coupling, which allows a high degree of accuracy for time of arrival measurements. It was shown that ultrasonic wave propagation in a typical beverage container is complex due to geometrical considerations. Multiple acoustic modes (*e.g.* symmetrical Lamb modes (s_0), shear horizontal SH modes, and longitudinal (L) modes) were shown to be present when conventional transient pulse excitation was used, and the presence of s_0 and SH modes was seen to prevent the required through-transmitted longitudinal (L) wave from being identified at all locations. Pulse-compression signal processing was thus employed for mode extraction while maintaining a high resolution and good signal-to-noise ratio.

The application of the pulse-compression signal processing technique to EMATs was also used to determine the location of water-oil interface in the container. The destructive interference at the boundary location was due to the mismatch of acoustic impedance between different media. The resolution obtained via arrival time was better than that obtained using attenuation, thought to be due mainly to the finite aperture of the EMATs.

Fan-beam tomography was also employed for tomographic imaging of the size and location of solid objects in a cylindrical container. Here the use of

mode extraction was seen to lead to clear images from the L mode, even though guided wave signals in the container wall were still present. This indicates that the combination of pulse-compression and mode extraction, when applied to EMAT transducers for the testing of fluid-filled containers, gives a distinct advantage over other forms of testing such objects.

In chapter 5, a Continuous Wavelet Transform (CWT) has been used to characterise Lamb wave group velocity dispersion from broadband signals in plates. Two approaches were described in this chapter. The main one was the use of a continuous wavelet transform using a Gaussian wavelet, followed by Hilbert Transform. This method leads to good results. The other approach was to use Morlet wavelet. This was also investigated for mode isolations. Direct comparisons were made with two approaches.

The use of a pair of non-contact EMATs to generate Lamb waves containing both zero and higher order modes was investigated. These multiple modes were superimposed on each other in the time-domain waveform. The CWT was able to separate these modes in time-frequency space, a process known as mode extraction, to allow dispersion measurements to be made.

The arrival times were then used with the known propagation distance to calculate the group velocity dispersion. The agreement between the time-frequency measured dispersion and the known theoretical dispersion curves for aluminium was excellent. The EMAT system was also used for tomographic imaging using Lamb waves. It was demonstrated that the performance was better for the higher order a_1 and s_1 modes than for the s_0 mode. Although amplitude-based data was found to give the best images in terms of dynamic range and signal-to-noise ratio, other methods using the frequency-shift of a given mode, or a change in mode arrival time, were also demonstrated.

Chapter 5 concluded that the wavelet transform approach is very useful when wide bandwidth measurements are made, such as when EMATs are used, and where more than one acoustic mode is present. It allows the modes to be identified so that one particular mode can be chosen easily from the complicated time waveform. This approach is likely to be useful for many other applications where reflections and multiple modes are likely to be encountered. The most noticeable difference between the two wavelet approaches is the fine frequency structure using the Morlet wavelet. The Mexican hat is real-valued and captures

both the positive and negative oscillations of the time series as separate peaks. The results follow by the Hilbert Transform combines both positive and negative peaks into a single broad peak. The Morlet is a complex wavelet in nature and contains both the magnitude and phase information. Hence, the resultant wavelet power combines both positive and negative peaks into a single sharp peak. The use of the Morlet wavelet would produce a plot similar to that from the Mexican hat approach. Overall, the same features appear in both plots, approximately at the same locations.

Chapter 6 described a pair of EMATs that has been used for the generation and detection of Lamb waves on steel sheets. The group velocity of the zero-order asymmetric and symmetric Lamb wave mode a_0 and s_0 , as well as the a_1 and s_2 of higher-order Lamb wave mode have been measured on metal sheets as a function of angle to the rolling direction. Multiple Lamb mode generation and detection was predicted using the Rayleigh-Lamb frequency relationship, and it has shown a good agreement with experimental results. The overlapping modes within the signal were further identified using the Short-Time Fourier Transform (STFT). Although the first-order symmetric Lamb wave mode (s_1) has not been detected, the use of smaller coil spacing can improve the detection of s_1 as was indicated by the dispersion curves. The Stationary Wavelet Transform (SWT) was employed to extract the information required to evaluate the texture characteristics of metal sheets. The exact orientation distribution coefficients (ODCs) values obtained in the experiments have been used for comparison with the theoretical fit. It is thus possible to extract the ODCs with 95% degree of confidence. This can be used as an indication of the suitability of the metal for cold forming technique.

The influence of dispersion on the texture measurements was quantified using the s_0 fundamental mode. An experiment was performed for ideal measurements of phase velocity, and this is used to serve as an accurate reference to the measurements made on a thicker sheet. The perfect phase velocity experiment has a thickness-wavelength ratio of ~ 0.03 , and the thicker sheet experiment has a thickness-wavelength ratio of ~ 0.22 . This resulted in small but statistically significant deviations from the predicted anisotropy. The asymmetric zero (s_0 and a_0) and higher order (a_1 and s_2) modes were chosen to compare the entire experimental dataset obtained from the s_0 mode. The a_0

mode appeared to have a similar velocity angular dependent pattern. The highest velocities for both s_0 and a_0 modes occurred in directions perpendicular to the rolling direction. The a_1 mode has a $\pm 90^\circ$ shift velocity angular dependent pattern compared to the s_0 mode. Interestingly, the s_0 mode has the largest variation of the group velocity against the angular axis, and the a_1 mode has the least. The directivity pattern observed using the amplitude is mostly due to the effect of birefringence.

Chapter 7 has demonstrated that rapid prototyping techniques can be used for the fabrication of EMATs. The EMAT coil pattern was created using an MSL process, and the complete EMAT architecture was produced using a combination of electro-deposition and polishing post-processing techniques. Two types of practical devices for different kinds of elastic wave generation were constructed and used to make ultrasonic measurements. These devices were characterised in terms of bandwidth and directivity, using both meander-line and spiral-coil geometries for shear wave generation. The detection of reflections from artificial defects was demonstrated, and their use in a SAFT imaging system led to the successful reconstruction of images. These MSL EMATs are likely to have many applications in NDE, as they can be made in a wide variety of shapes and sizes in a reproducible fashion. The use and complexity of possible EMAT configurations can become easier with the MSL technology increases, and it can also incorporate the electronics and magnets into the design.

8.3 Future Work

It is felt that the work presented in this thesis has contributed to the development of EMAT technology. It is hoped that it will prove useful in the development of future NDE applications. For future work, this could be extended in several ways.

Pulse compression techniques described in this thesis can be expanded with different coded waveforms to optimise applications. It is hoped that the techniques can be implemented in hardware for real online inspection. Thus,

future applications should focus on moving samples, which are usually difficult to inspect using piezoelectric transducers.

Wavelet transform signal processing techniques can be applied to EMATs in many different samples. Future work could thus include the use of the technique for samples exhibiting high attenuation and scattering. It is hoped that the discrimination between the noise and signals are still noticeable under these difficult situations, and that EMAT systems and techniques can open up more opportunities for Lamb wave NDE applications and imaging.

The fabrication of EMATs using micro-stereolithography (MSL) can be extended to produce smaller EMATs, and potentially EMAT arrays, for use in more NDE applications. It is hoped that the technique can produce micro-EMATs to improve resolution. It is also thought that more complicated coils could be fabricated using this technology. It is also evident that this MSL technique could have uses in other NDE technologies, including eddy currents and ultrasonics arrays, etc.

Bibliography

“Guide to Examinations for Higher Degrees by Research”, The University of Warwick Graduate School, May 2007.

Publications arising from this thesis

- [1] K. S. Ho, T. H. Gan, D. R. Billson and D. A. Hutchins, “Application of pulse compression signal processing techniques to electromagnetic acoustic transducers for noncontact thickness measurements and imaging,” *Rev. Sci. Instrum.*, vol. 76, pp. 54902-1, 05. 2005.
- [2] T. H. Gan, K. S. Ho, D. R. Billson and D. A. Hutchins, “Application of pulse compression signal processing techniques to electromagnetic acoustic transducers for noncontact thickness measurements and imaging,” in *16th WCNDT 2004 - World Conference on NDT*, 2004, pp. 51.
- [3] K. S. Ho, D. R. Billson and D. A. Hutchins, “Inspection of drinks cans using non-contact electromagnetic acoustic transducers,” *J. Food Eng.*, vol. 80, pp. 431-44, 05. 2007.
- [4] K. S. Ho, D. R. Billson and D. A. Hutchins, “Ultrasonic Lamb wave tomography using scanned EMATs and wavelet processing,” *Nondestr. Test. Eval.*, vol. 22, pp. 19-34, 2007.
- [5] K. S. Ho, R. J. Bradley, D. R. Billson and D. A. Hutchins, “Electromagnetic acoustic transducers (EMATs) fabricated using micro-stereolithography,” *Ultrasonics*, submitted for publication, Feb. 2007.